Lawrence Berkeley National Laboratory

Title

THE CURRENT EXPERIMENTAL SITUATION IN HEAVY-ION REACTIONS

Author

Scott, David K.

Publication Date

2011-03-18

THE CURRENT EXPERIMENTAL SITUATION IN HEAVY-ION REACTIONS

David K. Scott

Lawrence Berkeley Laboratory
University of California
Berkeley, California 94720

INTRODUCTION

Let us begin on a grandiose note by comparing heavy-ion collisions, which occur on the shortest scales of time and space in the Universe (10^{-23} sec and 10^{-13} cm), with the collisions of galaxies (then both exponents are positive!). Figure 1.1 shows the spectacular NGC 5194 spiral nebula in Canes Venatici,[1] with the satellite nebula NGC 5195. The analysis of this type of cosmological event uses a simple potential model with gravitational forces folded over the mass density distributions.[2,3] The collision of two equal mass

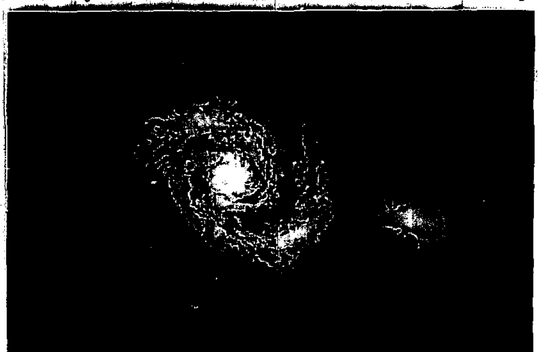

Figure 1.1

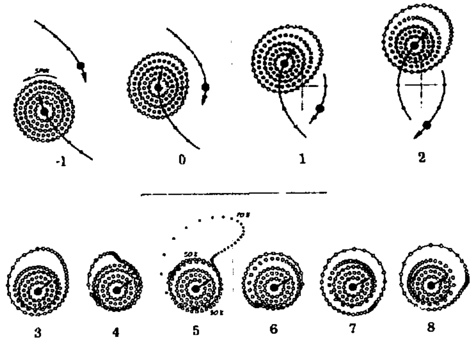

Figure 1.2

galaxies, where one has some initial symmetric distribution counter to the parabolic orbit of the incident galaxy, is shown in Fig. 1.2. As time passes, we see the build-up of a tidal wave which eventually spews out mass in the "target fragmentation region," leaving behind some hot, residual system which seeks a stable mode. Now compare the collision of ^{20}Ne on ^{238}U at incident relativistic energies of

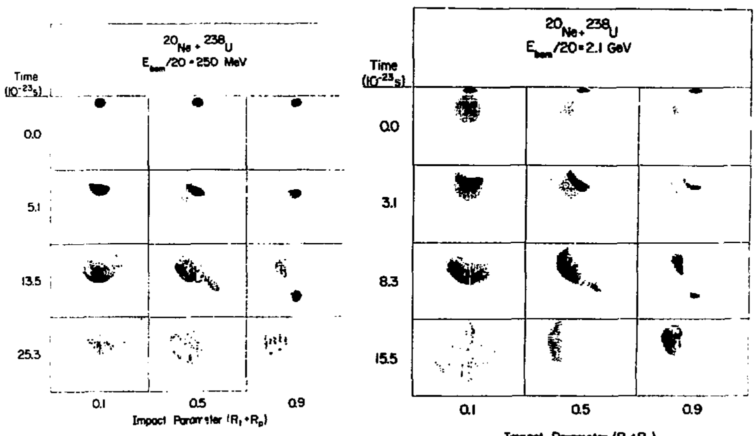

Figure 1.3

XBL 777-9763

250 MeV/nucleon and 2.1 GeV/nucleon in Fig. 1.3; these pictures were generated by solving the hydrodynamic equations,[4] and show nuclear rather than galactic matter streaming out, as the wounded nuclei try to recover. (The hydrodynamic equations have also been solved for star-star collisions.[5,6])

The relevance of heavy-ion collisions to cosmological events may be even more profound. In Fig. 1.4 is shown the temperature reached in the nuclear fireball (the region of matter dispersed between the target and the projectile in Fig. 1.3) as a function of the incident energy of two colliding ions,[7] for two assumptions about the hadronic mass spectrum. The curve labeled "experimental" corresponds to a mass spectrum containing essentially the known particles, while that labeled "Hagedorn" corresponds to the bootstrap hypothesis of an exponential growth of hadrons. In this model the temperature limits at ≈140 MeV (and such a limit may have been observed[8]), a temperature approaching the limit reached at the earliest recognizable moments of our Universe, in the Cosmic Big Bang.[9] After this beginning to our lectures, let us hope that we do not end with a whimper!

These examples demonstrate that there is considerable interest throughout the whole of physics in the collisions of structured objects, especially insofar as the phenomena may be explained in the context of a microscopic theory. In the most general sense, this motivation justifies the enormous effort and expense poured into providing heavy-ion beams as massive as uranium up to energies of 2 GeV/nucleon for the study of nuclear interactions. (Useful sources on developments in the field are contained in Refs. 10-30.) A more specific motivation becomes evident when we take a panoramic view of the stability diagram[31] for nuclear species in Fig. 1.5.

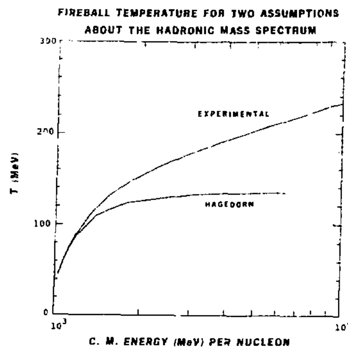

Figure 1.4

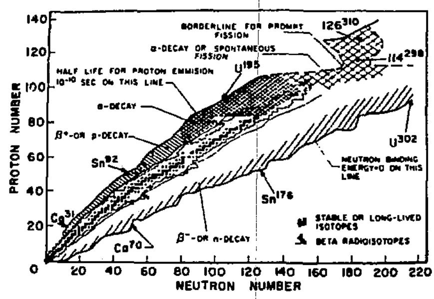

Figure 1.5

There are 300 stable nuclear species. During the last half century only some 1300 additional radioisotopes have been identified and studied. It is estimated that in the interaction of U + U, 6000 new species could be formed. The historic role of heavy-ion physics, through the study of these nuclei, will be to relax the limitations that have been imposed on the study of nuclear physics over its 60 year history — limitations of nuclear charge and mass number, limitation of spherical shape, limitations of "normal" temperatures and pressures and reaction mechanisms. The influence of very heavy-ion accelerators is already beginning to be felt in theoretical chemistry, in atomic physics, and quantum electrodynamics as well as in nuclear physics itself. Over the last few years, a wave of enthusiasm has caused nuclear physicists to focus on research with heavy ions, and the view both near and far is one of increasing excitement which has pervaded the conference halls and the research laboratories, dominated the research proposals and preoccupied the funding agencies. It shows no signs of abatement.

In these lectures I shall attempt to give a survey of the present experimental situation in Heavy-Ion Physics. I shall draw heavily from a similar course of lectures delivered last year,[30] updated by the many new trends which have emerged since that time — or which were unknown to me then! In order to chart a navigable course through the vast territory of heavy-ion literature, I shall make a division into three continents, named (a) Microscopia, (b) Macroscopia, and (c) Asymptotia, which will deal in turn (a) with the simple excitation of discrete states in elastic scattering, transfer and compound nuclear reactions; (b) with more drastic perturbations of the nucleus high in the continuum through fusion, fission and deeply-inelastic scattering; and (c) with the (possibly) limiting asymptotic phenomena of relativistic heavy-ion collisions. However, it will be one of the goals of these lectures — and my selection of material is so guided — to show that there are definite signs of a *Continental drift*, with a merging of the microscopic, macroscopic and asymptotic approaches. When they finally become a Trinity, no doubt we shall find Utopia, but I am afraid we shall not reach it in these lectures. However, the very fact that we are gathered here to discuss both heavy-ion *and* pion physics is also an indication of the reunification of the many branches into which nuclear physics has become divided. Perhaps we could do well to reflect on Benjamin Franklin's injunction to his colleagues, "Gentlemen, let us all hang together, or we may all hang separately." In other words, make out of necessity a golden opportunity to strike down artificial barriers in physics, providing a better perspective on many aspects of nuclear dynamics.[32]

1. MICROSCOPIA

We shall begin by defining some of the parameters of heavy-ion reactions, and then use this knowledge to describe the characteristic features of elastic scattering. The status of optical potentials is then treated, followed by their incorporation into the DWBA formalism for simple transfer reactions. A survey of more complicated multinucleon transfer leads us to heavy-ion compound nuclear reactions, from which most of our knowledge of new types of states excited in heavy-ion collisions is presently being gleaned. Throughout this, and the subsequent lectures, the emphasis will be on heavy-ion collisions at energies well above the barrier, since this region is the wave of the future.

1.1 Characteristics of Heavy-Ion Collisions

In the collision of nuclei with charge and mass numbers Z_1, A_1 and Z_2, A_2, some useful quantities are defined in Fig. 1.6

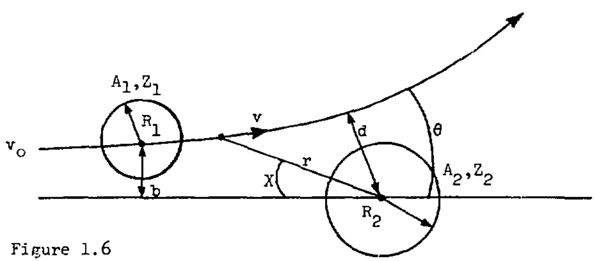

Figure 1.6

$$\text{Reduced mass}\quad \mu = \frac{mA_1A_2}{A_1+A_2}\,, \qquad m = \text{nucleon mass.} \tag{1.1}$$

Relative velocity = v,

$$\frac{v}{c} = \sqrt{\frac{E_{lab}}{469\,A_1}}\,, \qquad E \text{ in MeV}. \tag{1.2}$$

$$\text{Wave number}\quad k = \frac{1}{\lambda\!\!\!^{-}} = \frac{\mu v}{\hbar} = \frac{4\cdot 8\ A_1A_2}{A_1 + A_2}\left(\frac{v}{c}\right). \tag{1.3}$$

Kinetic energy of relative motion $E = \tfrac{1}{2}\,\mu v^2$. (1.4)

Half distance of closest approach in head-on collision

$$a = \frac{Z_1Z_2e^2}{\mu v^2} = \frac{Z_1Z_2}{2E_{cm}}\left(\frac{e^2}{\hbar c}\right)\hbar c\ . \tag{1.5}$$

$$\text{Sommerfeld parameter}\quad \eta = ka = \frac{Z_1Z_2e^2}{\hbar v} \tag{1.6}$$

Classical impact parameter = b.

Associated angular momentum = kb = ℓ (partial wave).

Scattering angle = θ.

Strong interaction radius $R = R_1 + R_2 = r_o(A_1^{1/3} + A_2^{1/3})$.

For a Rutherford orbit,

$$\begin{aligned} d &= a(1 + \operatorname{cosec}\theta/2) \\ &= a + \sqrt{a^2 + b^2} \\ &= \eta/k\ (1 + \sqrt{1 + (\ell/\eta)^2} \end{aligned} \tag{1.7}$$

Critical scattering angle θ_g or θ_c when $d = R$,

$$\sin\frac{\theta_c}{2} = \frac{a}{R - a} \tag{1.8}$$

$$b_c = R\sqrt{1 - 2a/R} \tag{1.9}$$

$$\ell_c = kb_c = kR(1 - 2\eta/kR) \tag{1.10}$$

Heavy-ion reactions are characterized by large values of $kR = R/\lambda\!\!\!^{-} \gg 1$. Such considerations lead us to the concept of a semi-classical trajectory, associated with different impact parameters. Indeed the very features that complicate *numerical* calculations for heavy-ion interactions, high orbital angular momenta $\ell = kR$ and large Sommerfeld parameter η, are just those that may be turned to advantage in semi-classical *analytical* computations. Referring to Fig. 1.6, we can write for a given point on the orbit, by conservation of angular momentum and energy:

$$\mu r^2 \dot{\chi} = \ell = \mu v_o b \tag{1.11}$$

$$\tfrac{1}{2}\mu \dot{r}^2 + \tfrac{1}{2}\mu r^2 \dot{\chi}^2 + V(r) = E = \tfrac{1}{2}\mu v_o^2 \tag{1.12}$$

Then

$$\frac{d\chi}{dr} = \frac{d\chi/dt}{dr/dt} = \frac{\dot{\chi}}{\dot{r}} = \frac{\ell}{r^2} \frac{1}{\sqrt{E - V(r) - \ell^2/2\mu r^2}} \tag{1.13}$$

and we can calculate the scattering angle

$$\theta(\ell) = \pi - 2\int_d^\infty \frac{\ell}{r^2} \frac{dr}{\sqrt{2\mu E - 2\mu V(r) - \ell^2/r^2}} \tag{1.14}$$

since $\theta = \pi - 2\chi$. Here $V(r)$ is the total potential, comprising Coulomb + nuclear. Equation (1.14) enables us to construct a scattering diagram and a deflection function diagram, which typically looks like Fig. 1.7.

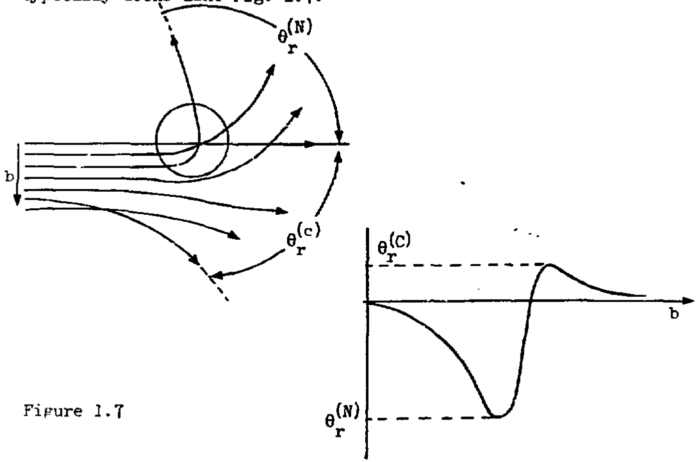

Figure 1.7

For large impact parameter b the trajectory follows a Coulomb orbit, and as b decreases θ initially decreases. At smaller impact parameters the attractive nuclear potential pulls the trajectory forward so there is a maximum scattering angle $\theta_r^{(C)}$, called the Coulomb rainbow angle, *beyond which scattering is forbidden* classically. The attraction pulls the trajectories round to a *maximum negative* angle, after which still smaller impact parameters again scatter to smaller angles. This negative maximum is called the nuclear rainbow angle, $\theta_r^{(N)}$. The trend is concisely represented in the deflection function diagram at the bottom. One of the contrasts between light- and heavy-ion scattering is the prominence of *nuclear rainbows in the former* and Coulomb rainbows in the latter.[33] These considerations lead us to predict an elastic scattering distribution (Fig. 1.8).

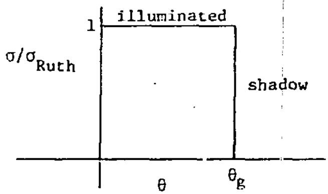

Figure 1.8

The scattering follows the Rutherford pattern up to the grazing trajectory. Beyond that is the shadow region, where classically no particles penetrate. Note, however, that a similar picture can be generated by *strong absorption* inside the grazing trajectory. Then the shadow is generated by an imaginary rather than the real potential.[34]

We compare these zeroth order predictions with the two standard forms occurring experimentally in Fig. 1.9, which shows the scattering of ^{16}O of 10 MeV/nucleon on ^{208}Pb and ^{12}C.

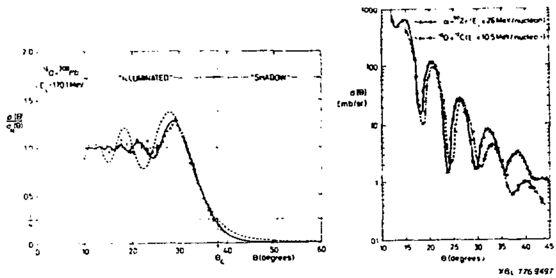

Figure 1.9

These are examples of Fresnel and Fraunhoffer diffraction. In the case of $^{16}O + ^{208}Pb$, the scattering is Coulomb dominated and the *average trend* is indeed as in Fig. 1.8. An interpretation of the *diffraction patterns* is possible in the semiclassical picture by introducing *complex trajectories*,[35,36] and is discussed by R. Schaeffer in this lecture series.

1.2 More Formal Treatment of Elastic Scattering

The scattering amplitude can be written

$$f(\theta) = \frac{1}{ik} \sum_{\ell} (2\ell+1) P_{\ell}(\cos\theta) \left(e^{2i\delta_{\ell}} - 1\right) \tag{1.15}$$

Using semi-classical ideas:[37,38]

a) Replace ℓ by continuous variable L, $\ell + \frac{1}{2} \to L$.
b) Assume continuous variation of phase shift $\delta(L)$ with L.
c) Replace $P_{\ell}(\cos\theta)$ by an asymptotic form for large L.
d) Replace Σ by $\int$.

Then

$$f(\theta) \approx \frac{1}{ik} \int L\, dL\, J_0(L \sin\theta) \left(e^{2i\delta(L)} - 1\right) \tag{1.16}$$

is valid if $\theta \lesssim \pi/6$.

If we set

$$\begin{aligned} e^{2i\delta(L)} &= 1, \qquad L > L_c \\ &= 0, \qquad L < L_c \ , \end{aligned} \tag{1.17}$$

(i.e., no scattering if $L > L_c$, complete absorption if $L < L_c$), the integral can be evaluated to give the diffractive cross section

$$\sigma_D(\theta) \approx (kR^2)^2 \left[\frac{J_1(kR\theta)}{kR\theta}\right]^2 \tag{1.18}$$

where $L = kR$. This diffraction cross section has a characteristic oscillatory behavior with spacing

$$\Delta\theta_D \approx \pi/kR \ . \tag{1.19}$$

In order to discover the predicted trend of differential cross sections we tabulate some values of parameters in Table 1.1. We see that the $^{16}O + ^{12}C$ reaction at 168 MeV has a small Sommerfeld parameter η and has similar values of η, kR, $\lambda\!\!\!^{-}$, a, R, θ_c to the reaction $\alpha + ^{94}Zr$ at 104 MeV. There is therefore nothing mysterious about the almost exactly similar differential cross sections shown in Fig. 1.9(b), of the predicted Fraunhoffer diffraction spacing, 4.6°.

TABLE 1.1. Interaction radius computed as $r_0(A_1^{1/3} + A_2^{1/3})$ with r_0 = 1.6 fm.

Ions	a	R (fm)	λ	E (MeV)	v/c	η	θ_c	kF	$\Delta\theta_c$
$\alpha + {}^{94}Zr$	0.577	9.81	[illegible]	104	0.235	2.49	7.17	42	4.24
${}^{16}O + {}^{12}C$	0.479	7.69	0.203	168	0.159	2.34	[illegible]	38	[illegible]
${}^{16}O + {}^{208}Pb$	1.628	13.51	[illegible]	[illegible]	[illegible]	[illegible]	[illegible]	137	[illegible]
${}^{238}U + {}^{238}U$	5.114	19.83	0.033	2380	0.093	1166	45.67	600	0.30

A reaction such as ${}^{16}O + {}^{208}Pb$ is characterized by a large η parameter and is Coulomb-dominated, leading to Fresnel scattering (the Fraunhoffer scattering would be difficult to observe experimentally since $\Delta\theta_D \approx 0.3°$).

In this case we make the large angle approximation to $f(\theta)$:

$$f(\theta) \approx \frac{1}{ik}\int_0^{\infty} L\, dL \left(\frac{2}{\pi L \sin\theta}\right)^{\frac{1}{2}} \cos\left(L\theta - \frac{\pi}{4}\right)\left(e^{2i\delta(L)} - 1\right) \quad (1.20)$$

At a scattering angle θ, the main contribution to the integral comes from values of L near L_θ given by

$$2\left(\frac{d\delta(L)}{dL}\right)_\theta = \pm\theta \quad (1.21)$$

[Note: This is an equation for L_θ: for Coulomb phase shifts gives $L_\theta = \eta\cot(\theta/2)$.]

Expand $\delta(L)$ about L_θ:

$$\delta(L) = \delta(L_\theta) + \left(\frac{d\delta}{dL}\right)(L - L_\theta) + \frac{1}{2}\left(\frac{d^2\delta}{dL^2}\right)(L - L_\theta)^2 + \ldots \quad (1.22)$$

$$\therefore 2\delta(L) = 2\delta(L_\theta) + \theta(L - L_\theta) + \frac{1}{2}\left(\frac{d\theta}{dL}\right)(L - L_\theta)^2 + \ldots \quad (1.23)$$

Taking out slowly varying functions, and replacing the lower limit of integration by L_c (i.e. sharp cut-off model):

$$f(\theta) \approx \frac{1}{k}\sqrt{\frac{L_\theta}{2\pi\sin\theta}}\; e^{i\alpha(\theta)}\int_{L_c}^{\infty} dL\, \exp\left[\frac{i}{2}\left(\frac{d\theta}{dL}\right)_\theta (L-L_\theta)^2\right] \quad (1.24)$$

This is just the Fresnel integral (compare Fig. 1.9(a)).

Introducing a new variable x by

$$\pi x^2 = \left(\frac{d\theta}{dL}\right)_\theta (L-L_\theta)^2 \quad (1.25)$$

$$f(\theta) = \frac{1}{k}\sqrt{\frac{L_\theta (dL/d\theta)_\theta}{2\sin\theta}}\; e^{i\alpha(\theta)}\int_{x_c}^{\infty} dx\, \exp \frac{i\pi}{2} x^2 \quad (1.26)$$

The integral can be evaluated, replacing $x_c \to -\infty$, i.e. $L_c < L_\theta$, as $\sqrt{2}\, e^{i\pi/4}$. Then

$$f(\theta) = \frac{1}{k}\sqrt{\frac{L_\theta (dL/d\theta)}{\sin\theta}}\; e^{i\bar{\alpha}(\theta)} \quad \text{where} \quad \bar{\alpha} = \alpha + \frac{\pi}{4}\left(\frac{d\theta}{dL}\right)_\theta \quad (1.27)$$

and

$$\sigma(\theta) = |f(\theta)|^2 = \frac{1}{\sin\theta}\left(\frac{bdb}{d\theta}\right) \quad (1.28)$$

where $L_\theta = kb_\theta$, which is just the classical scattering formula.

Now we note that if x_c is set equal to zero, i.e., $L = L_c$, we have the simple result that at the *critical angle* θ_c,

$$\frac{\sigma(\theta)}{\sigma_R(\theta)} = \frac{1}{4} \quad (1.29)$$

which is the origin of the famous "quarter-point" recipe.[39] We shall see that this point (and others closely related) dominate most heavy-ion elastic scattering experiments. To make further progress we either have to introduce more elaborate parameterizations of the phase shifts[38] (which *can* be done, e.g. smooth cut-off instead of sharp cut-off) or resort to the common practice of dressing everything up by an *optical potential*.

1.4 Optical Model Analysis of Elastic Scattering

Most analyses have used a Saxon-Woods nuclear optical potential. (The Coulomb and centrifugal potentials must also be included.)

$$U(r) = -V(e^{x}+1)^{-1} - iW(e^{x'}+1)^{-1} \qquad (1.30)$$

where

$$x = (r-R)/a \qquad R = r_0(A_1^{1/3} + A_2^{1/3})$$

$$x' = (r-R')/a' \qquad R' = r_0'(A_1^{1/3} + A_2^{1/3})$$

Most often the four-parameter form, $R = R'$ and $a = a'$, is used.

The most coherent picture would be that of quoting a global set of parameters, but we are not quite there yet. There are tremendous ambiguities associated with the potentials for the scattering of strongly absorbed particles, which are sensitive only to the extreme tail of the potential.

As an example, consider data for the reaction $^{16}O + {}^{208}Pb$ at 192 MeV shown in Fig. 1.10(a) (similar to that shown in Fig. 1.9(a)). The analysis with Saxon-Woods potentials in Fig. 1.10(b) illustrates three potentials which fit the 192 MeV data equally well.[40] *Only the value of the potential at 12.5 fm is well determined.* Note that the actual value of the nuclear potential at this point (≈ 1 MeV) is very small compared to the Coulomb (≈ 75 MeV). The cross-over point is called the *sensitive radius* (R_S) and has the same significance as the Fresnel ¼-point discussed previously. In fact, from Fig. 1.10(a), $\theta_{1/4} = 31.4°$. Then,

$$L_{1/4} = \eta \cot(\theta_{1/4}/2) = 105 \,, \qquad \eta = 29.9 \qquad (1.31)$$

and

$$R_{1/4} = \eta/k \left(1 + \sqrt{1+(1/\eta)^2}\right) = \text{[illegible] fm} \qquad (1.32)$$

which is close to the 12.5 fm of the cross-over. The point also coincides with the radius associated with the ℓ-value at which the optical model transmission coefficient drops to ½, ($R_{1/2}$), and $L_{1/2} = 106$ in the above example. This distance is typically 2 or 3 fm *larger* than the sum of the radii of the two ions, at which their densities fall to one-half of the central value.[41] Even when absorption is almost complete, only the 10% regions overlap. From classical perturbation theory it can be shown[42] that elastic scattering mainly determines the real part of the optical potential at a point slightly inside the distance of closest approach for a

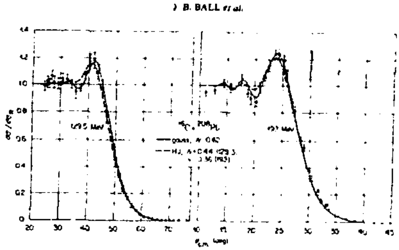

Figure 1.10(a)

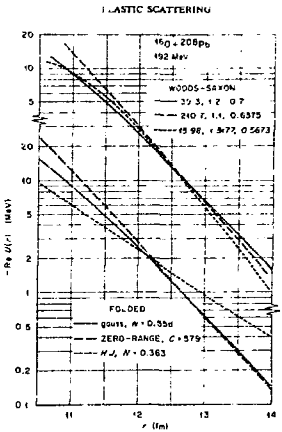

XBL 777-9498

Figure 1.10(b)

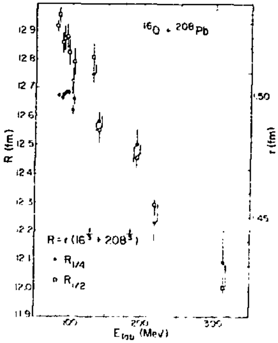

Figure 1.11

trajectory leading to a rainbow angle, and this distance should become constant at high energies. A detailed analysis of the data for the $^{16}O + ^{208}Pb$ system[34] shows that from 90 MeV to 190 MeV, the scattering is indeed refractive, with $R_{1/2}$ roughly constant. Recently the elastic scattering has been extended to 315 MeV (see Fig. 1.11) suggesting rather that the distance continues to decrease, and that higher energies may be able to prove the potential deeper inside the nucleus.[43]

Higher bombarding energies have been used in an attempt to resolve the ambiguities in the $^{16}O + ^{28}Si$ system.[44,45] The data at 215 MeV are shown in Fig. 1.12. The idea is to take data beyond the rainbow angle, where an exponentially decreasing cross section will be observed if the real potential is sufficiently weak. Too

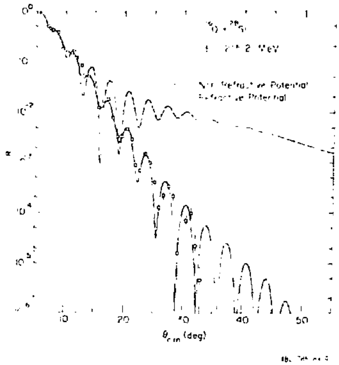

Figure 1.12

much absorption will always give rise to a *diffractive* pattern. The data are clearly diffractive, and call for potentials with $V/W < 0.5$ (in contrast to those for light ions for which $V/W \approx 5.0$), assuming an energy independence; this is expected to be small for heavy-ions.[46] The solid curve is for $V = 10$, $W = 23$, $r_o = 1.35$, $r_o' = 1.23$, $a = 0.618$ and $a' = 0.552$, whereas the dashed curve is for a deep potential of 100 MeV. The potentials extracted for $^{12}C + ^{28}Si$ are quantitatively very similar.[47]

Given the abrupt change in character of potentials for light ions (e.g., alpha particles) and heavy ions as light as ^{12}C, obviously one must look in between, say at ^{6}Li. In fact the results[47] in Fig. 1.13 have a pronounced nuclear rainbow similar to α-scattering, completely at variance with shallow 10 MeV diffractive potentials, but unable nonetheless to pin down the real potential to better than between 150 and 200 MeV (with $W \approx 40$ MeV in both cases). Now the search is on with ^{9}Be, and no doubt Mother Nature will be clever enough to hide the sudden transition between light and heavy ions in the nucleus ^{8}Be! The suddenness of the transition is a challenge to fundamental theoretical derivations of heavy-ion potentials and we end our discussion of elastic scattering with a catalogue of some of these approaches.

1.4 More General Approach to Heavy-Ion Potentials

As we have seen, the study of heavy-ion potentials is hampered in general by the insensitivity of elastic scattering to all but the value of the potential at the strong interaction radius. [illegible]s natural therefore that both experiment and theory should turn to methods which determine the potential at closer distances. A[illegible]r distance where the nucleus-nucleus interaction is established can be estimated from the liquid drop model. This is the distance

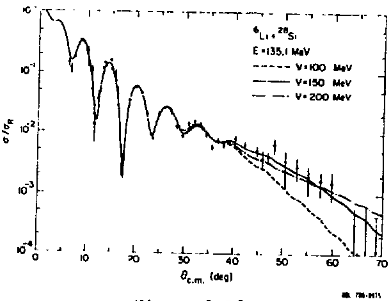

Figure 1.13

corresponding to the sum of the half-density radii R_1 and R_2 where the attractive force is:[48]

$$F = 4\pi\gamma \frac{R_1 R_2}{R_1 + R_2}, \quad R_1 + R_2 = R_0 \tag{1.33}$$

where $\gamma \approx 0.95$ MeV·fm^{-2} is the surface tension coefficient. The previously determined sensitive radius and the value of the potential at this point, together with the value of the force:

$$\left(\frac{dV}{dr}\right)_{r=R_0} = \frac{V}{4a} = 4\pi\gamma \frac{R_1 R_2}{R_0} \tag{1.34}$$

determine the two parameters V and a. The sum of the half density radii R_1+R_2 can be evaluated using expressions of the form:[49]

$$R_1 = 1.12\ A^{1/3} - 0.86\ A^{-1/3} \tag{1.35}$$

(The deviation from strict proportionality to $A^{1/3}$ comes from purely geometrical considerations of a spherical distribution with a diffuse surface.) Using these equations, the nuclear potential can be calculated for any target projectile combination, and lead typically to potentials 60 MeV deep, of diffuseness 0.85 fm.

These simple considerations have been generalized by the *Proximity Force Theorem* which states:[50]

> *"The force between rigid gently curved surfaces is proportional to the potential per unit area between flat surfaces."*

For frozen, spherical density distributions, the force between two nuclei as a function of distance s between their surfaces is

$$F(s) = 2\pi \frac{R_1 R_2}{R_1 + R_2} e(s) \tag{1.36}$$

where e(s) is the potential energy per unit area, as a function of the distance between flat surfaces. The touching of two flat surfaces results in a potential energy gain per unit area equal to twice the surface energy coefficient,

$$\therefore\ e(0) = -2\gamma$$

leading to the same maximum force as above. (The force becomes repulsive as the two density distributions overlap.)

For the potential we obtain,

$$U(s) = 2\pi \frac{R_1 R_2}{R_1 + R_2} \int_s^\infty e(s')ds' \tag{1.37}$$

where

$$s = r - (R_1 + R_2) \ .$$

The interaction is given in terms of a universal function e(s); once known or calculated for one pair of nuclei, we immediately have information about other pairs. Although based on a liquid drop model, the formula is actually very general. Suppose that the interaction energy is represented by a folding formula with a δ-function interaction:

$$U = A\ \rho_1(r_1)\rho_2\ (r - r_1)d\underline{r_1} \tag{1.38}$$

If the densities ρ_1, ρ_2 have Saxon-Woods shapes

$$\rho = \frac{\rho_0}{\left[1 + \exp\left(\frac{r - R}{a}\right)\right]} \tag{1.39}$$

then the integral can be evaluated:[51]

$$U(s) = 2\pi A\ \rho_0^2 \frac{R_1 R_2}{R_1 + R_2} \int_s^\infty \frac{s'ds'}{\exp \frac{s'}{a-1}} \tag{1.40}$$

where $s = r - (R_1 + R_2)$, and has the proximity form with a particular expression for e(s). This result begins to link for us the *microscopic* and *macroscopic* approaches to potentials.

To compare with experiment, we write U(s) in the form

$$U = 4\pi\gamma \frac{R_1 R_2}{R_1 + R_2} b\phi(\zeta) \tag{1.41}$$

where $\zeta = s/b$, b = 1 fm, and $\gamma \approx 0.95\ \mathrm{MeV \cdot fm^{-2}}$. The universal function ϕ has been evaluated using the nuclear Thomas-Fermi method. We find:

$$\begin{aligned} \phi(\zeta < 1.25) &= -\tfrac{1}{2}(\zeta - 2.54)^2 - 0.85(\zeta - 2.54)^3 \\ \phi(\zeta > 1.25) &= -3.437\ \exp(-\zeta/0.75) \end{aligned} \tag{1.42}$$

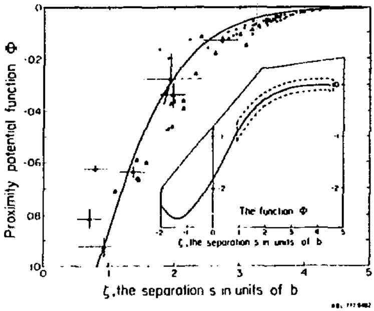

Figure 1.14

and is plotted in Fig. 1.14.[52]

The theoretical proximity function $\phi(\xi)$ in the extreme tail region has been compared with nuclear potentials deduced from an analysis of elastic scattering data, leading to values of ϕ from 0 to -0.16, and are reproduced in the figure by circles. We see (as expected) that elastic scattering tests the potential over ϕ at large values of ζ, i.e., radial distances near the strong absorption radius.

As we shall see in later sections, *inelastic* processes probe the potential to much smaller radii.[34] Values derived in this way are shown as triangles. The theoretical proximity potential is in good agreement with the data over the entire range of distances. A similar global comparison is discussed in Ref. 53, where the potential is tested at distances where friction effects are important, but this subject leads us into Macroscopia.

Many other approaches are taken to the theoretical derivation of heavy-ion potentials; for example, the folding model,[54-56] and the energy density formalism.[57,58] Perhaps it is appropriate to conclude with a comparison[42] in Fig. 1.15 of some of these potentials, evaluated at the sensitive radius with the Saxon-Woods potential for a wide range of interacting systems. Equally good agreement is produced by the *empirical potential* of proximity type:

$$V(r) = 50 \frac{R_1 R_2}{R_1 + R_2} \exp\left(\frac{r-R_1-R_2}{\alpha}\right)$$

with $R_1 = 1.233\, A_i^{1/3} - 0.978 A_i^{-1/3}$ and a = 0.63 fm.

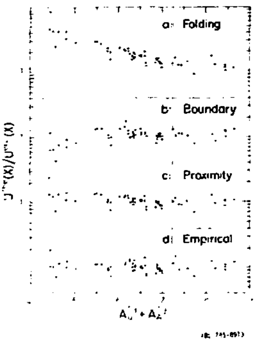

Figure 1.15

1.5 Transfer Reactions

The resurgence of interest in microscopic heavy-ion reactions around 1970 was largely (and rightly) triggered by the great hope that multinucleon transfers (which are possible only via heavy ion reactions) would reveal a rich spectrum of new types of states in nuclei, e.g., nuclear quartets.[12,59] The ideal scenario is to take the optical potentials from the elastic scattering studies of the previous sections, compute distorted waves in the initial and final channels, plug them into the DWBA transfer amplitude to get the cross sections for transfer. Since 1970, however, many studies of one, two, three and four nuclear transfers[60-62] (some of which are also possible with light ions!) indicate that the mechanisms are complicated by high order coupled channels and multistep effects. The whole subject has become bogged down in a welter of computational details. Let me try to show that the situation is not quite as black as it is often painted, and that heavy-ion reactions can still make an attack on nuclear structure problems.[64]

Look at a nucleus such as ^{20}Ne in which the spherical-basis shell model generates rotational like spectra described as (2s,1d).[4] A clear "rotational band" is predicted in agreement with experiment (Fig. 1.16), not only for level positions but also for E2 transition strengths (those in brackets are collective model, the others are shell model). It seems that the shell model is winning, because of the fall off of E2 strength for the higher spin states. The shell model also predicts that the band should terminate at J=8, whereas the collective model, as classically conceived, goes on forever, to states of 10, 12 .... If the band *did* run on, it would be a triumph for the collective model, but it would not be the end of the shell model. We would argue that as the excitation increases, so does the tendency to loosen the ^{16}O core so that the configurations such as $1p^{-2}(2s,1d)^6$ creep in, bringing higher angular

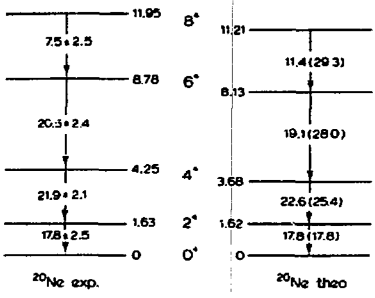

Figure 1.16

momentum. (Such merging of single particle and collective aspects will be taken up in our discussion of much higher angular momenta in nuclei, in the lecture on Macroscopia). If the band stops at J=8, the argument for the truth of the shell model as against the classical rotational model becomes very strong.

The states of the band should be strongly populated by attaching an α-particle to the ^{16}O core, and the same is true for the configurationally equivalent case in ^{16}O, by α-transfer on ^{12}C into the band beginning at 6.05 MeV. Now take a look at the spectrum[65] for the $^{12}C(^{11}B,{}^{7}Li)^{16}O$ reaction at 114 MeV in Fig. 1.17. We imagine the α-particle popped onto the ^{12}C surface, bringing in an angular momentum of several units due to its linear motion in the ^{11}B. The striking feature of the spectrum is the *extreme selectivity*. Only a few states appear up to 21 MeV excitation which can be identified with members of the rotational band

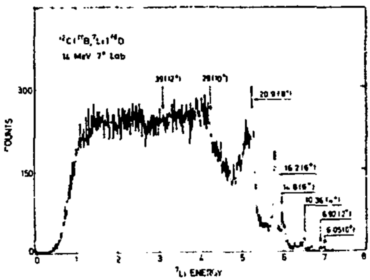

Figure 1.17

up to 8^+ (and also a negative parity band up to 7^-). Remember that the level density in ^{16}O around 20 MeV is many tens of levels/MeV. There is little sign of 10^+ and 12^+ levels which the $E_J = \hbar^2/2\mathcal{J}\ I(I+1)$ rotational scheme would place around 29 and 39 MeV. So this simple spectrum, *almost by inspection*, already strengthens our feeling that the shell model is probably an excellent first order description of nuclear structure and that the collective models are probably to be regarded as much more convenient representations of some aspects of the shell model, but secondary to it, rather than models that contain truths *beyond* those to be distilled from shell model wavefunctions.[64] However, we do need a quantitative theory of the reaction dynamics to predict the strengths of the states in Fig. 1.17. Let us begin with a simple, semiclassical one.

This model[66,67] assumes that the particles move on classical trajectories, as illustrated in Fig. 1.18. (The transfer is dealt with quantum-mechanically.) There are three kinematical conditions to be satisfied if the transfer probability of the cluster m (a nuclear or group of nuclears) is to be large. (We shall return to this theory in Lecture 3 on Deeply-Inelastic Scattering.) The cluster starts in an initial state $(\ell_1\lambda_1)$ and ends in $(\ell_2\lambda_2)$.

$$\Delta k = k_0 - \frac{\lambda_1}{R_1} - \frac{\lambda_2}{R_2} \approx 0 \qquad (1.1[illegible])$$

$$k_0 = \frac{mv}{\hbar}$$

where v is the speed of the particle at the transfer point.

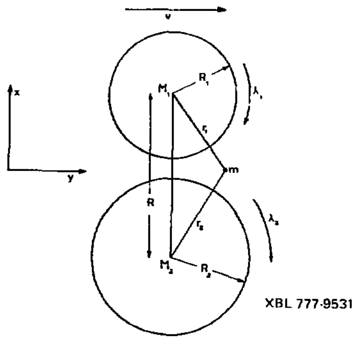

Figure 1.18

$$\Delta L = \lambda_2 - \lambda_1 + \tfrac{1}{2}k_0(R_1-R_2) + Q_{eff}\,\frac{R}{\hbar v} \approx 0 \qquad (1.44)$$

$$Q_{eff} = Q - (z_1^f z_2^f - z_1^i z_2^i)\, e^2/R \qquad (1.45)$$

$\ell_1 + \lambda_1,\ \ell_2 + \lambda_2$ even.

These conditions imply, respectively: conservation of the y-component of angular momentum of the transferred nucleon; conservation of angular momentum; and confinement of the transfer to the reaction plane, i.e., the angles θ in the spherical harmonics of the single particle wave functions are ≈ π/2. An approximate expression for the transition probability is:

$$P(\lambda_2\lambda_1) \sim S_1S_2P_0(R)\,\left|Y_{\ell_1}^{\lambda_1}\left(\tfrac{\pi}{2},0\right)\,Y_{\ell_2}^{\lambda_2}\left(\tfrac{\pi}{2},0\right)\right|^2 \times \exp\left[-\left(\frac{R\Delta k}{\sigma_1}\right)^2 - \left(\frac{\Delta L}{\sigma_2}\right)^2\right] \qquad (1.46)$$

where $P_0(R)$ is determined by the radial wave functions at the nuclear surface, and σ_1, σ_2 measure the spreads in Δk, ΔL from zero as allowed by the uncertainty principle. The total transition probability is then calculated by summing over the final magnetic substates and averaging over the initial substates, weighted by angular momentum coupling coefficients and the spectroscopic factors (S_1, S_2) for finding the cluster in the initial and final states. However, the localization and semi-classical aspects of the transfer usually mean that the reaction is "well matched" for a restricted range of λ_1, λ_2 and ℓ_1, ℓ_2. The spectroscopic amplitudes in the rotational band are very simple to calculate in the SU(3) model. They are just proportional to the intensities of the SU(3) [ ] representation in each state, which are equal for all members of the band (at about 0.36). A comparison of the experimental and theoretical cross sections[65] for the positive parity band are given in Table 1.2. (Theory and experiment are normalized for the 6^+ state.) There is still some uncertainty about the location of the 8^+ state[68] but it is more likely to be associated with the broad structure at 22 MeV excitation rather than at 20.9 MeV, which appears rather to be the 7^- member of the negative parity band. (Since the two states have roughly equal cross section, this ambiguity does not affect our discussion of Table 1.2.) By continuing this type of study to higher incident energies,[69] so that possible 10^+ and 12^+ states are *definitely* not disfavored by the reaction dynamics, it may still be possible to make interesting statements about nuclear structure, with only a *skeletal* reaction theory.

By comparing one, two, three and four nucleon transfers on different targets, all leading to the same *final* nucleus, it is possible to bootstrap one's way up through a hierarchy of simple

TABLE 1.2. Experimental and Theoretical Cross Sections for the Reaction $^{12}C(^{11}B, ^{7}Li)^{16}O$.

E_x, J^{π}	$6.05, 0^+$	$6.92, 2^+$	$10.35, 4^+$	$16.23, 6^+$	[illegible]$, 8^+$
$\frac{d\sigma}{d\Omega}$ (EXPT) mb/sr	≈0.0	0.006	0.019	0.250	0.224
$\frac{d\sigma}{d\Omega}$ (TH)	0.000	0.003	0.038	0.250	0.178

stretched, cluster configurations in light nuclei.[67,70] Indeed these experiments have already led to the formulation of literal cluster models by convoluting an α-particle with the core as a function of their separation, adding up all the nuclear-nuclear interactions to generate them from an effective α-core potential.

Another impressive demonstration that few nucleon transfer reactions can proceed by simple α-transfer comes from a comparison of it with the presumed inverse process, α-decay. Nuclei in the lead region are ideally suited to this test. For example, it is possible to derive a "reduced α-width" rate for ^{212}Po (0.727 MeV, 2^+) and ^{212}Po(gs) states from their decay to ^{208}Pb, from the formula,

$$\delta^2 = h/\tau P$$

where τ is the mean life and P the penetrability. Then, $\delta^2(2^+)/\delta^2(0^+) = 0.61$, in excellent agreement with the spectroscopic factor ratio $S(2^+)/S(0^+) = 0.64$, deduced from a direct reaction analysis of $^{208}Pb(^{16}O,^{12}C)^{212}Po$, leading to the conclusion that the basic quantities measured in alpha transfer and decay are homologous.[72,73] (There is, however, an intriguing problem that absolute values of the decay widths are underestimated by the shell model by a factor of 1000--which may indicate substantial clustering of alphas in the surface region,[74,75] and therefore surface phenomena not presently described by the shell model.) However, one is encouraged to look for other alpha particle strengths,[76] e.g., alpha vibrations,[77] analogous to pairing vibrations, so far with a mystifying lack of success.[76]

This type of stimulus is surely what we should expect and demand of heavy-ion transfer reactions. After all we do not need heavy-ions to study one and two nucleon transfers! Many interesting possibilities remain, so far almost completely untapped. Three and four *neutron* transfers are available *only* by heavy-ion reactions but even today there has only been a handful of studies.[78-81] Such reactions enable us to *locate* not only new configurations in nuclei, but also *new nuclei themselves*. Frequently, just the knowledge that a nucleus exists, stable against decay by strong interactions, together with the ground state mass-excess, can lead to new nuclear structure information. A striking case is the Na isotopes, which extend from ^{19}Na to ^{33}Na, the widest range of (N-Z)/A known to man (apart from He isotopes). This information led[82] to the prediction of a sudden shape change from spherical to deformed in the Na isotopes. Perhaps we should be devoting at least as much time to exploring these possibilities of testing our nuclear structure theories on exotic nuclei, as we spend on studying all the complexities of the reaction mechanism. Nevertheless, we must now spend some time looking at these complexities!

The formal quantal evaluation of heavy-ion direct reactions uses the DWBA. Symbolically the reaction can be written[83]

$$(a + c) + b \rightarrow (b + c) + a$$

where a, b, are the heavy-ion cores and c is the transferred particle. Then

$$T_{fi}^{DWBA} = \langle \chi_f \ \phi_{b+c} \ \phi_a \ | V_{ac} | \chi_i \ \phi_{a+c} \ \phi_b \rangle \tag{1.47}$$

where χ_f, χ_i are distorted waves, the scattering eigenfunctions, and ϕ are the eigenfunctions of nuclear Hamiltonians (see Fig. 1.19). The interaction V_{ac} (or V_{bc}) causes the transition (as usual one assumes that the core-core interaction V_{ab} cancels the potential in the initial channel).

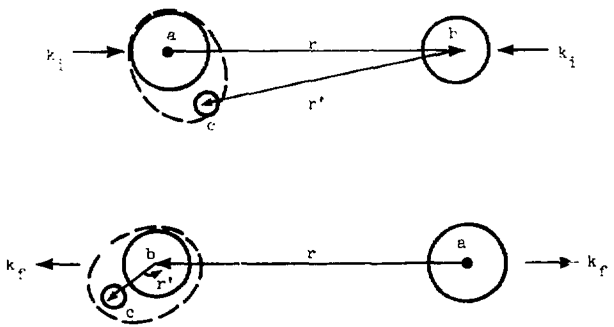

Figure 1.19

Using the coordinates of Fig. 1.19,

$$T_{fi} = \int d^3r \int d^3r' \; \chi_f^{(-)*}\left(k_f;\, r - \frac{r'}{A_f}\right) u_f^*(r') \; V_{ac}(r+r') \cdots$$

$$U_i(r+r') \; \chi_i^{(+)}\left(k_i;\, \frac{A_i - 1}{A_i}\, r - \frac{r'}{A_i}\right) \qquad (1.48)$$

where u_i, u_f are bound-state wave functions for c in the initial and final states, and $A_i = m_a + m_c/m_c$, $A_f = m_b + m_c/m_c$. This integral can be evaluated exactly and the correct procedure for calculating transfer reactions is: determine the distorted waves from an analysis of elastic scattering where the potential is fixed by some prescription such as that of Section 1.3, and then use them in the transfer integral.[84] This prescription has had many successes, but we wish here to concentrate on *failures*. Therefore, it is instructive to disentangle the various contributions to the six-dimensional integral.

A great simplification occurs if "recoil effects" are dropped, i.e., r'/A_f and r'/A_i are removed from the distorted waves. Then:

$$T_{fi} = \int d^3r \; \chi_f^{(-)*} \; (\underline{k}_f; \underline{r}) \quad \chi_i^{(+)}\left(\underline{k}_i;\, \frac{A_i - 1}{A_i}\, \underline{r}\right) G_{if}(r)$$

$$G_{if}(r) = \int d^3r' \; u_f^*(\underline{r}') \; V_{ac}(\underline{r} + \underline{r}') \; u_i(\underline{r} + \underline{r}') \qquad (1.49)$$

and we have two 3-D integrals. If, in addition, we make the "zero range" approximation:

$$G_{if}(r) = u_f^*(-r) \; u_i(0)$$

and

$$T_{fi} \propto \int d^3r \; \chi_f^*(k_f, r) \; \chi_i(k_i, r) \; u_f^*(r) \; . \qquad (1.50)$$

As an example, take an initial state where (a+c) and b are in $\ell = 0$ while in final state c is bound to b with orbital angular momentum L. The angular momentum transfer is L. Thus $u_f^* \propto \psi_L^*(r) \; Y_L^M(\hat{r})$.

Simplifying still further to a ring locus model (strong absorption) with *plane waves* $e^{i\underline{k}\cdot\underline{r}}$, and if the z-axis is chosen perpendicular to the annulus, $\Theta = \pi/2$ in the spherical harmonics, then

$$
\begin{aligned}
T_{fi}^{LM} &\propto P_L^M(\pi/2) \int_0^{\pi} d\phi \, \exp[i(\underline{k}_i - \underline{k}_f)\cdot\underline{r}] \exp(im\phi) \\
&\propto P_L^M(\pi/2) \int_0^{2\pi} d\phi \, \exp(iqR\cos\phi + im\phi) \\
&= 2\pi \, P_L^M(\pi/2) \, J_M(qR) \qquad (1.51)
\end{aligned}
$$

When the cross section is summed over all M-substates, the Legendre function requires L+M even, and therefore even L transfer will have oscillatory angular distributions characterized by:

$$\sum_M [J_M(2kR \sin\Theta/2)]^2 \qquad (1.52)$$

with even M; likewise odd L-transfer will have only odd M and we arrive at the well-known phase rules.

It is found that the main contribution at low energies is associated with $|M| = L$. Classically this corresponds to the transferred particle making the transition between orbits which are nearly perpendicular to the reaction plane; furthermore, as Fig. 1.20 shows,[60] if the initial value of m is $+\ell_i$, the final value will be $-\ell_f$ and the transfer is likely to occur with a large change in the component of L along the z-axis.

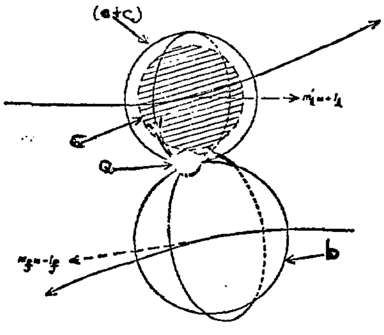

XBL 777-9532

Figure 1.20

The period of the angular oscillations (as usual) is $\approx \pi/kR$ at small angles. Take for example the stripping and pick-up reactions $^{40}Ca(^{13}C,^{12}C)^{41}Ca$ and $^{40}Ca(^{13}C,^{14}N)^{39}K$ which have been studied at 68 MeV. The data for both reactions[85] shown in Fig. 1.21 have oscillatory angular distributions of period $\pi/kR \approx 5°$ ($k \sim 4.97\ f^{-1}$ and $R \sim 8$ fm). For the stripping reaction, the DWBA (dashed line) works perfectly, but for pick-up (which should be mainly L = 1 transfer) the oscillations are exactly out of phase-- in fact, they fit with M = 0, rather than M = 1 in contradiction to our derived rules, and in contradiction to any reasonable attempts at rectification by the usual parameter juggling of optical model and bound-state parameters. An impressive array of escape routes have been brought to bear on this problem, which certainly do credit to the imagination of the theoreticians! Amongst the possible explanations are helicity spin flip,[86] molecular orbital approach[87] in which the interaction of the transferred particle with both cores is treated explicitly during the entire process. (See also polarization phenomena with the two-center shell model wave functions in heavy-ion transfer.[88] Whether such processes are important in heavy-ion reactions depends on the ratio

$$\frac{\text{transit time}}{\text{nuclear period}} \approx \left(\frac{E_{Fermi}}{E/A}\right)^{1/2} \approx \text{[illegible]}$$

for this reaction). An even more formidable explanation may be in the coupled channels approach to heavy-ion reactions.

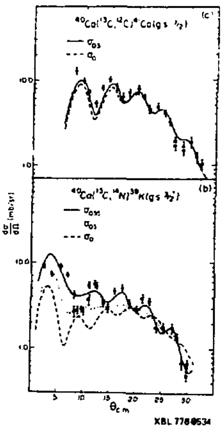

Figure 1.21

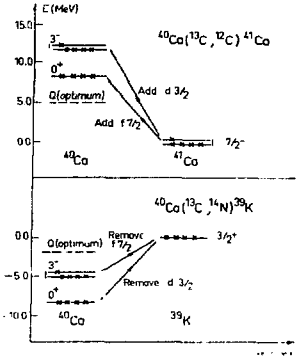

Coupled Channel Effects

It has been suggested that in addition to transferring the particle between the *ground states*, other routes may be important through, for example, pre-excitation of the ^{40}Ca prior to transfer.[89] (Such processes are two-step and go beyond the first-order perturbative treatment of the DWBA.) Some possibilities are illustrated in Fig. 1.22. For the stripping reaction the ^{40}Ca gs can be reached by adding an $f_{7/2}$ particle to ^{40}Ca (*a transition from* $(\ell_i - \frac{1}{2})$ in ^{13}C to $(\ell_f + \frac{1}{2})$ in ^{41}Ca) *or* by adding a $d_{3/2}$ particle to the pre-excited ^{40}Ca, 3^- state $((\ell_i + \frac{1}{2})$ to $(\ell_f + \frac{1}{2}))$. Remember, by our earlier arguments the latter is disfavored; it is further inhibited by the optimum Q-value ($Q_{opt} \approx -\frac{1}{2}mv^2 + \Delta V_C$) which is not very negative for neutron transfer, where $\Delta V_C = 0$. (This expression for Q_{opt} can be derived easily from equs. 1.43, 1.44 by assuming $\lambda_1 \simeq 0$ on the average, evaluating λ_2 from equ. 1.43 and substituting in equ. 1.44.) Therefore the inclusion of these routes does not have much effect on the stripping reaction (see Fig. 1.23).

Both arguments are reversed for pick-up, and we see that inclusion of 3^- and 5^- excitations improve the agreement of the phase of the oscillations.[90] This situation is not very satisfactory, because there are many other routes that could be included, and in fact inclusion of them all would far exceed present computational techniques. Furthermore, the strength required for the inelastic routes appear to exceed those observed experimentally.[91] However, they are still *too few* to produce the average couplings that we know how to handle via an absorptive potential.

The effects of coupled channels not only introduce additional transition routes to the final state; through the inelastic transitions they also modify the optical model wave functions of relative motion. The influence is quite subtle, as illustrated by inelastic scattering[92]

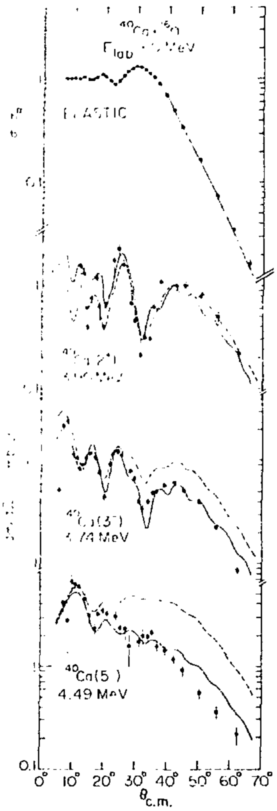

XBL 785-8916

Figure 1.23

of ^{16}O or ^{40}Ca in Fig. 1.23. The DWBA (dashed line) cannot fit all transitions simultaneously. Since the 3^- state is strongly coupled to the ground state, the imaginary part of the optical potential was modified to reproduce the elastic scattering in a coupled channels calculation involving only the ground and the 3^- state. The CCBA calculations then work for all the states (solid line), in particular the 5^- which is not directly coupled. This behavior is in contradiction to the assumption generally made in DWBA that in a direct reaction calculation for a given transition all other non-directly coupled channels can be treated through an average absorptive potential. These observations may account for the failure of DWBA in many heavy-ion transfer calculations, and hopefully will dispense with the ad hoc changes made in optical model parameters.

The previous section may have conveyed the impression that the present status of heavy-ion transfer reactions is a little bit like opening Pandora's Box. Nonetheless, it may be just in these complexities that some of the unique, interesting heavy-ion physics lies for nuclear spectroscopy. Let us look at a striking example. Consider two-neutron transfer, stripping, and pick-up reactions, as illustrated in Fig. 1.24. In pick-up to the 2^+ state, route 2 is direct, and in stripping, 3 is direct. Routes 1 and 4 are branches of indirect routes which can also contribute to transfer via inelastic scattering in the initial and final states. For *vibrational* nuclei the sign of the amplitudes 2 and 3 is opposite and leads to opposite interference patterns with the indirect routes--destructive in stripping and constructive in pick-up.[93,94] A further refinement is introduced by the contribution of Coulomb and nuclear terms to the indirect routes, which enter with opposite signs, and interfere differently with the direct routes.

In the pick-up reaction $^{76}Ge(^{16}O,^{18}O)^{74}Ge$, a very weak interference dip is observed[95] for the 2^+ of $^{74}Ge^*$ but not of $^{18}O^*$. It turns out that the direct transition to the 2^+ of ^{74}Ge is negligible, corresponding to the removal of two neutrons from the gs BCS superfluid vacuum of ^{76}Ge, leaving ^{74}Ge in the 2^+ particle-hole vibration. The main population is from the two-step process, first by the removal of a neutron pair to the gs of ^{74}Ge, followed by the creation of a quasi-particle pair of the 2^+. The dip is then caused by

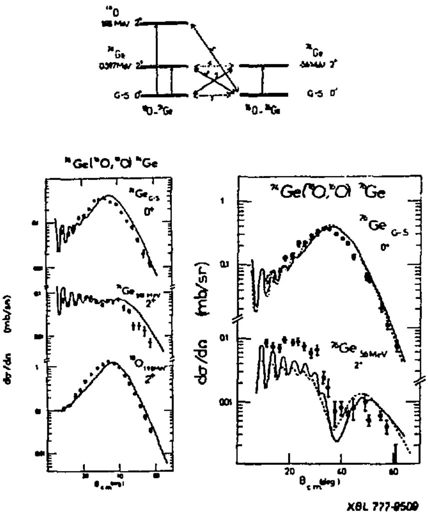

Figure 1.24

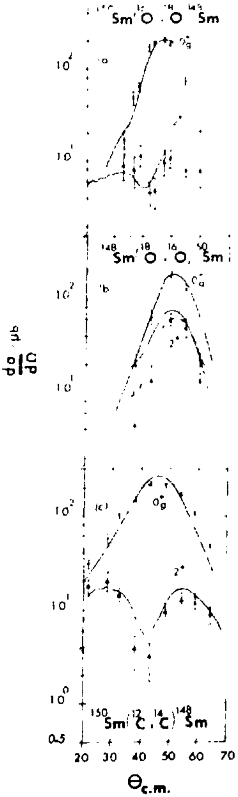

XBL 785-8919

Figure 1.25

Coulomb-nuclear interference in the inelastic scattering section. For the stripping reaction, on the other hand, the direct transition to the 2^+ of [illegible] is strong, and interferes destructively with the nuclear amplitude of the indirect routes, giving rise to a pronounced modification of the characteristic bell-shaped differential cross sections. The ground state transitions are of course identical in the two reactions, since they correspond roughly to time-reversed processes. The theoretical calculations shown require an [illegible] model parameters for the initial and final channels, deformation parameters for the inelastic excitation, detailed spectroscopic amplitudes for all the states involved in the coupling. The success of the theory is an encouraging indicator that this field--almost unique to heavy-ion transfer--could become important for unravelling sensitive details of the structure of collective states.[96-98]

The data for a similar pair of transfer reactions on Samarium isotopes at 100 MeV are shown in Fig. 1.25. Here the interference is the *opposite* sign from the Sm isotopes.[99] The theoretical curves are the first attempt to incorporate the *dynamic deformation method* with the CCBA formalism. This method is to be contrasted with an alternative attempt[100] to explain these data with the *boson expansion method*. In this latter theory the nuclear deformation effects arise as a result of complex mixing of a large number of spherical bosons whereas in the DDM method the nuclear deformations are introduced in the single particle basis, and further the deformations are treated as dynamic variables (in β and γ). The striking shape differences between the 2_1^+ distributions are however still not satisfactorily explained.

As an illustration of the scope for imagination in the study of heavy-ion reactions, it is fascinating to note that the interference phenomena due to multistep processes can be described in a Regge pole parameterization.[101] There occur two poles found at positions of the barrier-top resonances of the entrance and exit channels, i.e. a well matched reaction. If the poles for the transfer are very different from these, it is a clear sign that intermediate channels are important, indicating a multistep process. Another example comes from the old question of whether surface transparent imaginary potentials are necessary to fit the interference oscillations in two particle transfer reactions.[102] These diffractive oscillations are usually attributed to interferences between a peripheral Coulomb-dominated orbit on one side of the target nucleus and a slightly penetrating orbit on the far side. Too strong an absorption reduces the penetrating flux and extinguishes the interference pattern. However, it is also possible that the Coulomb dominated orbit can be weakened by multistep effects, and the final resolution is a very delicate balance.

There are severe technical problems both in the measurement and the computation of two nucleon transfer reactions of the type described above. To resolve the low lying collective states and identify the two neutron transfer products from elastic scattering is difficult. To calculate the absolute magnitude of two neutron transfer, complicated by problems such as simultaneous v. successive transfer,[103] is also no mean feat. We have only to look at the *quality* of both the data and the theory to wonder if our tools[104] would not be of much poorer quality without the challenge of heavy ions.

However, problems are also showing up in the much simpler one nucleon transfer reactions. Recently it has become possible to study heavy-ion transfer reactions over a wide energy range from sub-Coulomb up to 20 MeV/A. An example is the $^{208}Pb(^{16}O,^{15}N)^{209}Bi$ reaction. Because of the variety of low-lying single particle states outside the doubly-magic ^{208}Pb, this reaction has almost become a standard for testing reaction theories.[105]

Techniques for evaluating the finite-range, recoil DWBA are available and have been applied to the ^{16}O + ^{208}Pb data as a function of energy.[105] Such a study is an ideal test of the reaction model, compared to data at a single or closely spaced energies, where deficiencies may be masked by the extreme sensitivity to extraneous details, e.g., the wave functions used to describe the initial and final bound states.

The calculations used optical parameters, $V = 51$, $r_V = 1.11$, $W = 51$, $r_W = 1.11$, $a_V = 0.79$, and $a_W = 0.74$. The bound states were generated in Saxon-Woods wells with the depth adjusted to reproduce the binding energy: for $^{208}Pb + p$, $r_V = 1.28$, $a_V = 0.76$, $V_{spin-orbit} = 6$ MeV, $r_{SO} = 1.09$, and $a_{SO} = 0.60$; for $^{15}N + p$, $r_V = 1.20$, $a_V = 0.65$, $V_{SO} = 7$ MeV, $r_{SO} = 1.20$ and $a_{SO} = 0.65$. The resultant spectroscopic factors, normalized to unity for the ground state are shown in Table 1.3 and compared with other reactions and with theory. The satisfactory agreement is typical of the other beam energies *when each set of data is treated in isolation.*

When we compare experiment and theory as a function of energy (using the theoretical spectroscopic factors with their absolute values, when $S(h_{9/2}) = 0.95$) a failure of the theory by almost a factor of 10 is encountered from the sub-Coulomb energy of 69 MeV

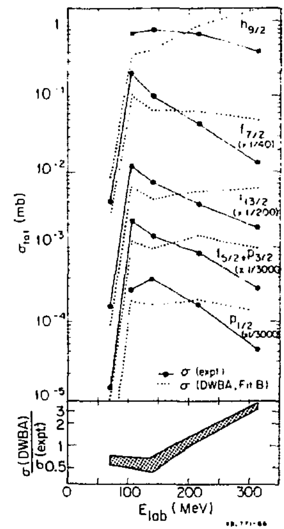

Figure 1.26

TABLE 1.3 Spectroscopic factors for $^{208}Pb(^{16}O,^{15}N)^{209}Bi$ data at 312.6 MeV.

State	E	$S(^{16}O,^{15}N)$	$S(^{12}C,^{11}B)$	$S(^{3}He,d)$	S(Theory)
$1h_{9/2}$	0.00	1.00	1.00	1.00	1.00
$2f_{7/2}$	0.90	0.85	0.96	0.67	0.89
$1i_{13/2}$	1.61	0.77	0.89	0.48	0.74
$2f_{5/2}$	2.84	0.77	0.64	0.75	0.69
$3p_{3/2}$	3.12	0.74	0.82	0.57	0.78
$3p_{1/2}$	3.64	0.69	--	0.38	0.57

up to [illegible] MeV (see Fig. 1.26). Of course such disagreements could be patched up, energy by energy, by ad hoc variations of bound state paremeters and optical potentials, sacrificing if necessary the qualitative relationship of the bound state potentials to the nucleon-nucleon optical potential, as well as the quality of the optical model fits to the elastic scattering. Such strategems miss the spirit of the model and even worse have no predictive power. Rather we should say that the method has failed and look for possible causes, as yet unknown.

1.6 Compound Nuclear Reactions

It may have come as a surprise that our discussion of transfer reactions had nothing to say about multinucleon transfers of more than four nucleons. It was discovered that such reactions usually proceed by the formation of a compound nucleus,[106] with subsequent evaporation of a complex fragment. These reactions also have some striking characteristics. For example, the differential cross sections are symmetric about 90° with a form $1/\sin\theta$, characteristic of emission from a high spin compound nucleus[106]:

$$\left(\frac{d\sigma}{d\Omega} \rightarrow \frac{d\sigma}{d\theta} \cdot \frac{d\theta}{d\Omega} \Rightarrow 1/\sin\theta, \text{ since } \frac{d\sigma}{d\theta} \text{ is constant}\right).$$

Sometimes the spectra show a highly selective excitation of high spin states (reminiscent of a direct reaction) and often they are entirely featureless. Compare for example the reactions $^{14}N(^{14}N,\alpha)^{24}Mg$ and $^{10}B(^{12}C,d)^{20}Ne$ in Fig. 1.27.[107,108]

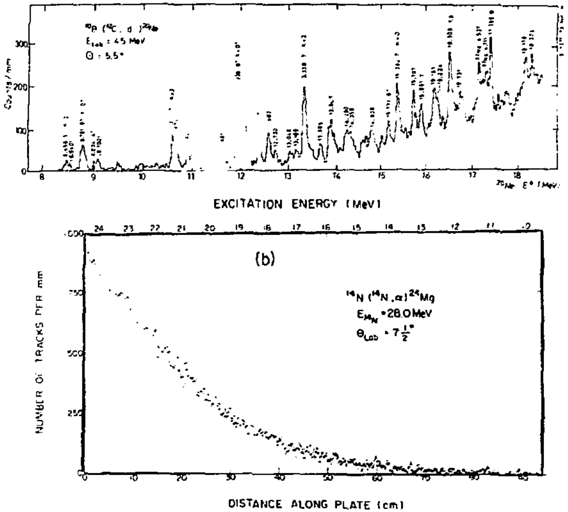

XBL 777 9569B

Figure 1.27

It turns out that both the formation and decay of the compound nucleus are dominated by a few partial waves close to the grazing value, and therefore it is plausible that only those levels located inside or near the curve defined by $L_{inc}^{grazing}$ and $L_{out}^{grazing}$ (which is a function of the Q-value and excitation energy of the reaction, i.e. $E_f = E_{CM} + Q - E_X$ and $L_{out}^{grazing} \approx R_f\sqrt{2M_fE_f}$) will be strongly excited. The shape of the spectrum is determined by the overlap between this curve and the yrast line of the final nucleus, the lowest excitation possible in the nucleus for a given J. Above this locus the level density increases exponentially. So one expects *for example, from Fig. 1.28,* that the (^{12}C,d) reaction would be selective[109] and the (^{14}N,α) reaction not,[110] which is just the

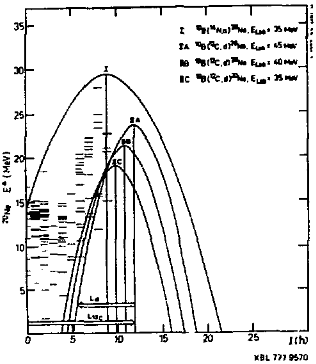

Figure 1.28

experimental observation.

For a detailed quantitative treatment, Hauser-Feshbach calculations are necessary,[111] with many attendant technical and philosophical difficulties. In the formation of the compound nucleus, the summation over angular momentum may have to be truncated, because the compound nucleus is unable to support large amounts before fission. The spin cut-off and level density parameters have to be determined. It turns out that the calculations of the *ratio* of two cross sections is relatively stable against all these multifarious uncertainties. The fits of the ratio of the statistical theory cross sections for states at E* = 11.92 and 12.14 in

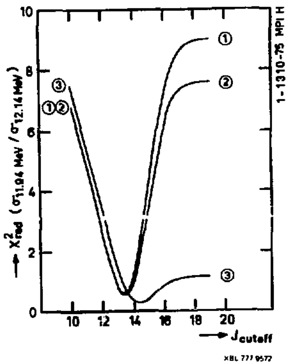

Figure 1.29

^{20}Ne to the ratio of the experimental cross sections for different choices of the level density parameter "a" (curves 1 and 2 average "a" over shell effects (a ~ A/6); curve 3 takes into account the final nucleus shell effects) are shown[112] in Fig. 1.29, as a function of the angular momentum cut-off, J_{crit}. Clearly this quantity can be deduced with high accuracy(14 ± 1) for this $^{10}B(^{12}C,d)^{20}Ne$ reaction at 45 MeV. (We shall discuss the origins of J_{crit} in the next lecture.) But clearly, having determined it for states of known spin, the procedure can be turned around, and new spin assignments made from the observed relative cross sections. (For a more detailed discussion see my lecture notes in Ref. 30.)

Now, we go *beyond conventional spectroscopy* and we discuss the evidence for nuclear molecular states, which are formed by the two colliding ions rotating in a dumb-bell configuration.[113,114] These have manifested themselves as resonances in the excitation functions of heavy-ion elastic scattering[115] and of reactions. For $^{12}C + ^{12}C$ and $^{16}O + ^{16}O$ elastic scattering the resonances are shown[116] in Fig. 1.30. There are wild oscillations which continue unabated to high energies (the equivalent excitation energy in ^{24}Mg for the $^{12}C + ^{12}C$ system is E_{CM} + 13.93 MeV). At the lower energies the resonances have been interpreted as shape resonances and fitted[117] with a potential of the form shown in Table 1.4.

The fits obtained have the correct characters (see Fig. 1.31) and at certain energies are almost pure $[P_L(\cos\theta)]^2$. The values of

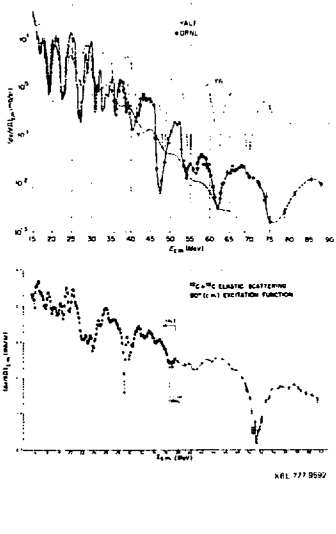

Figure 1.30

TABLE 1.4

System	V	R	a	W	R_I	a_I
$C^{12} + C^{12}$	14	6.18	0.35	$0.4 + 0.1E$	6.41	[illegible]
$O^{16} + O^{16}$	17	6.8	0.49	$0.8 + 0.2E$	6.40	[illegible]

[illegible] are shown at the right. At these energies the phase sh[illegible] close to $\pi/2$. The quality of fit for the $^{16}O + ^{16}O$ system [illegible] high energies with the above potential appears in Fig. [illegible] curve Y6. Weak absorption is essential for a descripti[illegible] resonance width ($\approx 2W$); only if the surface regions rem[illegible] parent can the interacting nuclei retain their identity for a [illegible] ficiently long period to make a molecular description meaning[illegible] (For a microscopic justification of this transparency, see [illegible] 11?, 119.)

Closer examination of the excitation functions re[illegible] that in addition to the potential shape resonances there is a superimposed fine structure of $\approx$ 100 KeV width. Such structure [illegible] been discovered in the excitation functions of many reaction [illegible]. A good example is the $^{12}C(^{12}C,p)^{23}Na$ reaction illustrated in Fig. [illegible]

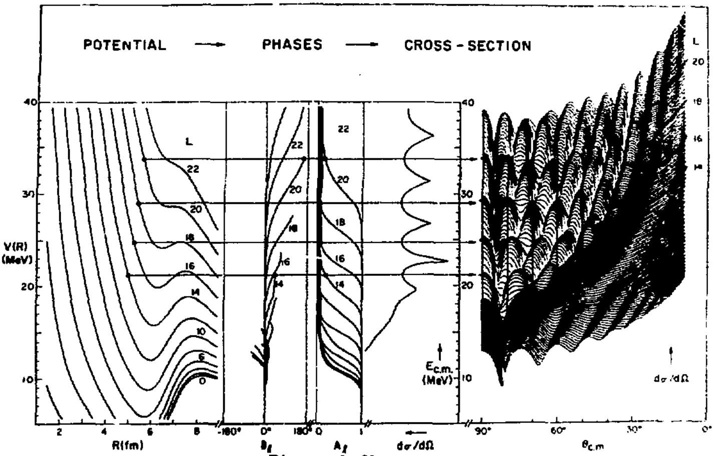

Figure 1.31

XBL 772-9666

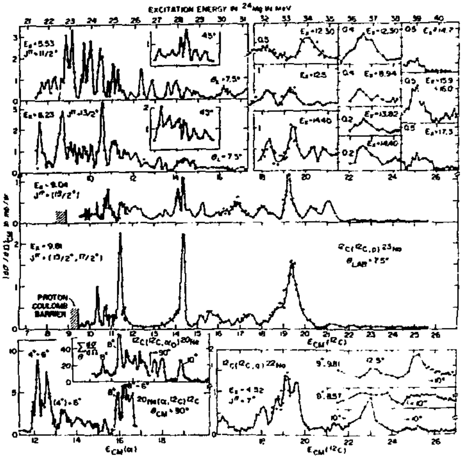

XBL 777 9571

Figure 1.32

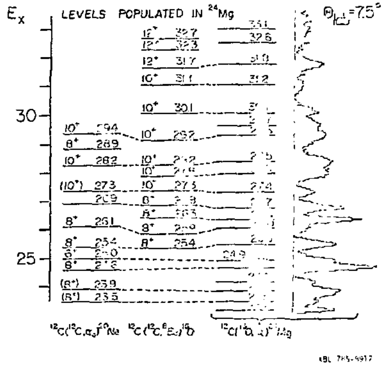

XBL 785-9917

Figure 1.33

for several different residual states in ^{23}Na, and compared with other outgoing α, d channels.[120] The equivalent excitation energies of the compound ^{24}Mg system is shown at the top. There exist pronounced narrow resonances at 11.4, 14.3 and 19.3 MeV which are strongly correlated in different channels. By comparing branching ratios, spins of 8^+, 10^+ and 12^+ were assigned.

Another example is the $^{12}C(^{16}O,\alpha)^{24}Mg$ *reaction*[121] *for which* the energy spectrum, averaged over incident energies from 62–100 MeV, is shown in Fig. 1.33, and compared with other "α-particle" channels. Possible correspondences in the spectra are indicated by the dashed lines. Because of the differing non-resonant background which can interfere with the resonant amplitude, the energy of the resonance is not necessarily the same in all channels; however the shift cannot be much larger than the width (note that in contradistinction to our discussion of this type of reaction earlier, there is evidence for direct aspects in the observed selectivity—e.g., there is a preponderance of positive parity levels, whereas positive and negative natural parity states in the $J = 6$ to 12 ħ region are expected on the compound picture; these multinucleon transfers may therefore also be useful for populating states of particular structure in a direct process). We notice that the levels appear to be grouping themselves into clusters of a given J^π.

A summary of all reported resonances[114] appears in Fig. 1.34; the groups fall on a line constituting a Regge trajectory[122], or quasi-molecular rotational band, where

$$E_J \propto \frac{\hbar^2}{2\mathcal{I}} J(J+1) \tag{1.53}$$

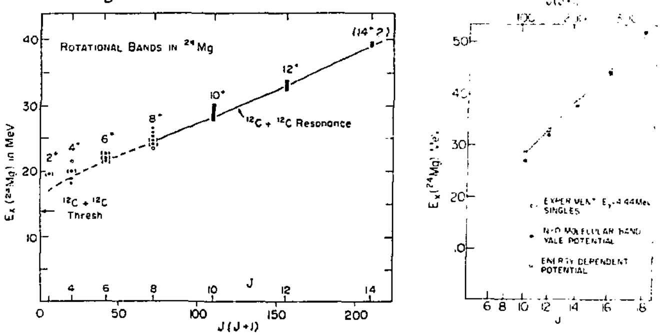

Figure 1.34

XBL 777-9560

The resonances correspond to pockets in the potential for the different partial waves (see Fig. 1.31). The slope of the line in Fig. 1.34 corresponds to the $\hbar^2/2\mathcal{J} \approx 100$ KeV, just the value we calculate for two carbon nuclei in dumbell rotation at the grazing distance (see Fig. 1.35). (For comparison, the $\hbar^2/2\mathcal{J}$ of the ground state band is ≈ 200 KeV, i.e. a lower moment of inertia $\approx \frac{2}{5} MR^2$. Extrapolation of the band to the 0^+ member on the vertical axis shows that the band begins almost at the threshold for $^{12}C + ^{12}C$ in ^{24}Mg, as predicted in a cluster molecular model.[123] Pushing the picture still further, we obtain the value 2.6×10^{21} sec^{-1} for the frequency of rotation corresponding, e.g. to the 8^+ resonance at ≈ 25 MeV, and considering the envelope of all the 8^+ resonances (≈ 3 MeV) as the width of the molecular resonance, we obtain a lifetime of 4×10^{-22} sec. Thus the two ^{12}C nuclei would perform $\approx 1/10$ of a full rotation before either coalescing a splitting into the $^{12}C + ^{12}C$ exit channel.[124]

The fact that the resonances of a given spin group and secondly that their centroids fall close to the value of the Yale potential (Table 1.4) suggests that, because of the gross structure, windows exist for the specific angular momenta. These windows permit the carbon nuclei to be in close contact, to interact and thereby to fragment into a number of narrow doorway state resonances. This interaction must be weak, because a strong one would have moved the resonances out of the window. Also the summed widths of a resonance of given J is an appreciable fraction of the gross structure width. Several models of this fragmentation exist,[114] one of which involves the excitation of the ^{12}C nucleus to its 2^+, 4.43 MeV level, or the double excitation of both nuclei.[125,126] A resonance occurs at an

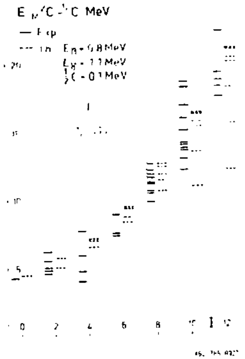

Figure 1.35

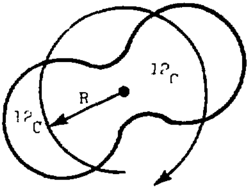

$$\mathcal{J} = 2 \times 2/5\ MR^2 + MR^2$$

$$\hbar^2/2\mathcal{J} = 100\ \text{keV}$$

$$R \doteq 2.7\ \text{fm}$$

Figure 1.36

energy such that after the excitation of the nuclei, they are in a quasi-bound state of the appropriate angular momentum. Thus the doorway state consists of excited ^{12}C nuclei trapped in a potential well pocket. Another approach[124] lets the shock of the initial collision lead to surface vibrations in the system, similar to β,γ vibrations. These split up the wide rotational resonance. Applying the first order rotation-vibration model[127] leads to a rather satisfactory agreement with the data (Fig. 1.36).

Support for the first picture of the resonances comes from a recent experiment[128,129] on the integrated cross sections for the reactions $^{12}C(^{12}C, ^{12}C^*)\ ^{12}C^*$ where either of the final ^{12}C can be excited into the 2^+ level at 4.43 MeV. Figure 1.37 shows that both

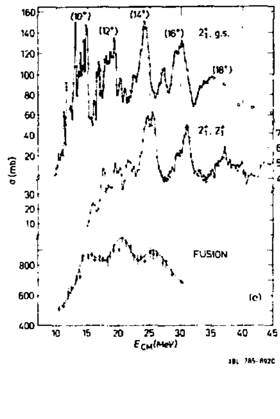

Figure 1.37

the double and single excitation functions are dominated by broad resonances *and* underlying fine structure. The upper three resonances fall nicely on the continuation of the molecular band, with the same moment of inertia, and with suggested spins 14^+, 16^+, 18^+ (see Fig. 1.34). The resonances also appear to line up with data on the fusion cross section. A partial width decomposition for the $J^\pi = 10^+, 12^+, 14^+$ gross structure resonance is made by assuming that the experimental total width is given by:

$$\Gamma = \Gamma_C + \Gamma_{2^+} + \Gamma_{2^+,2^+} + \Gamma_{cn}$$

and that, 1.54

$$\sigma_i = 2(2J+1)\pi\lambda^2 \frac{\Gamma_c\Gamma_i}{(\Gamma/2)^2}$$

(with $i = 2^+$, $2^+\cdot 2^+$ and cn) relates the resonant total cross sections σ_i and the various partial widths. The compound nucleus cross section σ_{cn} and width Γ_{cn} are identified with the resonant component of the fusion cross section. One of the resultant solutions of the quadratic equations is given in Table 1.5, and compared with the predicted total width of the quasi-molecular model.

TABLE 1.5

J^π	Ex ^{24}Mg	Γ_{TOT}	Γ_C	Γ_{2^+}	$\Gamma_{2^+2^+}$	Γ_{cn}	Molecular Band Ex.	Molecular Band Γ_{tot}
10^+	28.5	1.8	1.35	0.11	≤0.01	0.13	28.6	1.1
12^+	33.0	3.0	2.41	0.22	≤0.04	0.33	32.8	2.0
14^+	39.0	2.5	1.94	0.27	0.13	0.16	37.8	3.4

The extracted widths are somewhat less than those of the quasi-molecular rotational band, indicating the intermediate structural nature of the states. It is also true that this type of intermediate structure, believed once to be almost unique to the $^{12}C + {}^{12}C$ system, is also emerging [130-132] in the $^{12}C + {}^{16}O$ and, more excitingly, in much heavier systems, as we now discuss.

Recall the system $^{16}O + {}^{28}Si$ which we discussed earlier (Section 1.3.1) as an example of elastic scatterings over a wide energy range to determine the optical potential. Recently[133] angular distributions have been extended into the backward hemisphere (Fig. 1.38), and reveals an oscillatory pattern, which is quite distinct from the forward angle Fresnel and Fraunhoffer diffraction patterns. In fact a continuation to backward angles of the angular

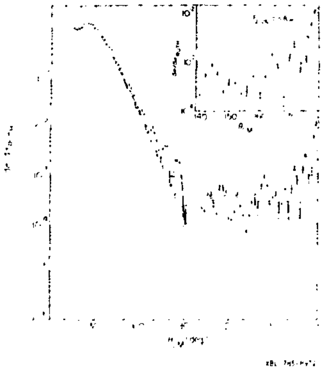

Figure 1.38

distributions predicted by the "unique" potentials established in section 1.3 leads to the dashed curve. The oscillations are characteristic of $|P_{\ell} = 26(\cos\theta)|^2$, with $\ell = 26$ close to the grazing partial wave, and *may* find a natural explanation in terms of a surface Regge pole resonance.[101,134]

It is therefore perhaps no surprise to find that excitation functions for $^{16}O + {}^{28}Si$ and $^{12}C + {}^{28}Si$ also give rise to resonance structure[135,136] very similar to the lighter systems we have been discussing, as the examples in Fig. 1.39 show.[135] At each of the resonances, the differential cross sections have a fairly pure $|P_{\ell}(\cos\theta)|^2$ form, and for the peaks in $^{16}O + {}^{28}Si$ at E_{CM} = 21, 26, 32 and 35 MeV, the ℓ values are 9, 17, 22 and 24 $\hbar$. The irregular

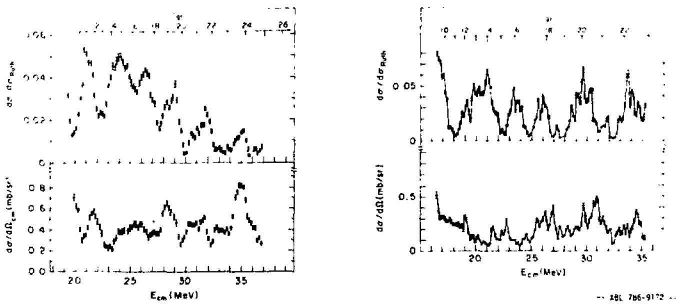

Figure 1.39

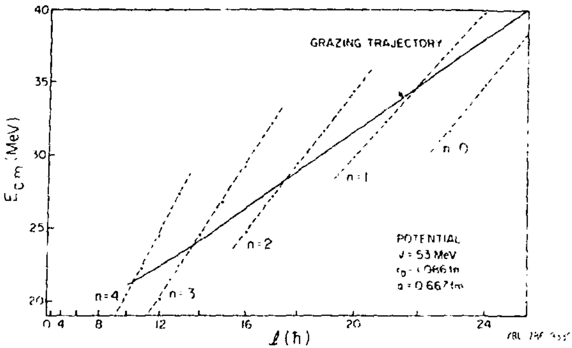

Figure 1.40

spin sequence is very difficult to reconcile with the Regge molecular band,[137] which follows the grazing trajectory. However a calculation of shape resonances using a folding model potential leads to several rotational bands, all with moments of inertia smaller than the grazing trajectory. The observed irregular sequence could be due to the intersection of the grazing trajectory (see Fig. 1.40) with rotational bands of different principal quantum numbers.[135] It would

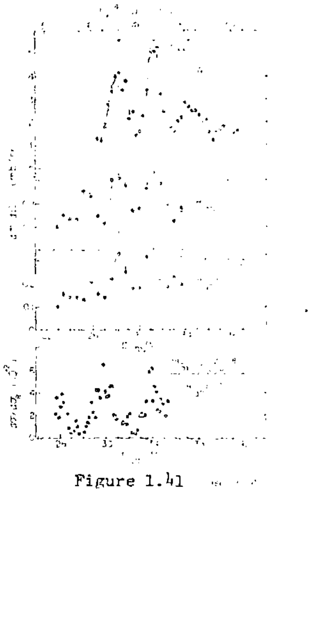

Figure 1.41

also be interesting to know whether interferences between the reflected waves from the inner and outer potential barrier as have been recently discussed[137(a)] might produce the structures. A very recent explanation has been given in terms of a parity-dependent potential.[137(b)]

Since we have primarily discussed elastic scattering and transfer reactions in this lecture, it is appropriate to end with a synthesis of the two, which gives a new direction towards the understanding of these resonances. If these phenomena indeed occur in the grazing partial waves, then similar effects might show up at forward angles in *transfer* reactions, where the contributing ℓ-waves are also strongly surface peaked. The excitation function[138] for the ^{24}Mg (^{16}O, ^{12}C) ^{28}Si reaction appears in Fig. 1.41. (Here the *exit* channel is one in which resonances in elastic scattering are observed.) There is indeed strong resonant behavior, which coincides with, elastic and inelastic channels. Are these also shape resonances, generated by surface transparent potentials, or are they evidence for more subtle effects in the structure of ^{40}Ca at high angular momenta? Perhaps the α-transfer plays a special role, and therefore many other channels have to be tested. It seems clear however that even complicated systems at very high excitation are revealing a most unexpected simplicity.

There is hope that this simplicity can be treated in a microscopic model which describes the fragments by displaced oscillator shell model wave functions.[450] For ^{16}O + ^{16}O and + ^{40}Ca the minima of the energy expectation values for various angular momenta are in good agreement with the experimental resonance energies, confirming the concept of an underlying quasimolecular structure. A first test of this interpretation is provided by the fact that the intrinsic state of such a nuclear molecule has mixed parity. Whereas shell model states show a gap of $\approx \hbar\omega$ between positive and negative parity states, a nuclear molecule should have positive and negative parity states in a common band. Hence, if the concept of a nuclear molecule is applicable one should find little or no splitting between bands of positive and negative parity. For the system α + ^{40}Ca the experimental splitting is less than 0.6 MeV. The microscopic description also yields resonances in the ^{16}O + ^{40}Ca system and therefore they appear to be a widespread feature of heavy-ion systems both experimentally and theoretically. The microscopic treatment shows that a description in the framework of a simple optical potential must be non-local and energy dependent. This fact may explain the recent spurt of activity which "explains" the resonances in the ^{16}O + ^{28}Si system by a variety of unusual potentials, e.g., a parity dependent potential,[137(b)] or an energy dependent, surface transparent potential.[451]

Only a short time ago, the resonances in the $^{12}C + ^{12}C$ system were believed to be unique, giving us only a glimpse of shape resonances and also the next stage in the hierarchy of increasing complexity of doorway states. The carbon nuclei avoided both the Scylla of being too easily polarizable and the Charybdis of not being polarizable at all.[114] Now we are through these straits, and the whole ocean lies ahead to explore for years to come. This exploration can be made with the low-energy, Tandem Accelerators scattered around the world. Compared with the mighty ocean-going Titanic of the Berkeley Bevalac, these "outboard motor boats" are inexpensive to run, and it is exciting that they continue to reveal fundamental aspects of the nucleus. Hopefully the Berkeley Bevalac will lead to its own fundamental discoveries, but that subject must wait until the last lecture. In the next lecture, we move on to much higher perturbations of the nucleus, beyond the region of discrete excitations, which has dominated our discussion of Microscopia.

2. MACROSCOPIA (FUSION AND FISSION)

The last lecture ended on a hopeful note. By means of heavy-ion reactions, the possibility is at hand of observing nuclei under unusual conditions of rotation and shape. Already discrete states of spin 18 $\hbar$ have been observed in nuclei at excitation energies of over 50 MeV. The theoretical description of this state of motion presents a challenge comparable to understanding the rotation of homogeneous masses as idealized representations of planets and stars back in Newton's days. It is a challenge that has been met in a remarkable series of experimental and theoretical developments. In this lecture we convey some idea of violent changes of shape undergone by the nucleus as more angular momentum is added to the fused system. Eventually the nucleus cannot sustain the centrifugal forces and it flies apart in fission. This behavior has an important bearing on the problem of synthesizing superheavy elements, once regarded as the prime motivation for the construction of heavy-ion accelerators.

2.1 Nuclei at High Angular Momentum

Before embarking on a discussion of nuclei subjected to these extreme stresses, we should note that the determination of nuclear matter and charge distributions of nuclei near their ground states has long been an important stimulus to the development of nuclear structure theories. Information on the moments of the nuclear charge distribution comes from experiments with electromagnetic probes, whereas the nuclear matter distributions come from hadronic scattering experiments. The availability of high energy, heavy-ion beams has expanded the horizons for inelastic excitation by hadrons, because they display interesting interference effects between Coulomb and nuclear excitation. In the DWBA, the excitation of a collective level is described in the interaction form factor $F_L^C(r) + F_L^N(r)$, where

$$F_L^C(r) = \frac{eZ_1 \; 4\Pi_1 \sqrt{B(EL)}}{2L+1} \; \frac{1}{r^{L+1}} \tag{2.1}$$

$$F_L^N(r) = \beta_L^N(V_R R_R \frac{df}{dr} + i \; W_I R_I \frac{dg}{dr})$$

Here L is the multipolarity of the transition and F^C and F^N are Coulomb and nuclear excitation forces. The latter is proportional to the derivative of the optical potential. β_L^N is the potential deformation. Since V_R is usually attractive, while the Coulomb potential is repulsive, there result minima in the scattering angular distribution of excitation functions.

From vast and beautiful literature on this subject,[139,140] we select an example from the collision of very heavy nuclei,[141] Kr + Th and Ar + U (Fig. 2.1). The excitation functions for back-scattered particles in coincidence with the de-excitation γ-ray cascade are shown. The solid line is the prediction of pure Coulomb excitation (using a semi-classical approach[142]), which agrees with the low spin data. But there is a rich variety of interference phenomena due to Coulomb-Nuclear interference; the sign, strength and energy for onset are state dependent. The solid and dashed-dot lines use proximity nuclear potentials[143] of the type we discussed in Lecture 1. Since these potentials fit some states but not others we infer that inelastic excitation carries information about the nuclear potential *beyond* that contained in elastic scattering. It may therefore be possible to probe the nuclear surface directly, and we may learn even more about the delicate shapes of nuclei such as ^{234}U, at present known to carry both quadrupole (β_2) and hexadecupole (β_4) deformations (Fig. 2.2).[139] There are also some remarkable experiments on Coulomb excitation of low lying states in Pt with Xe projectiles, that suggest rigid triaxial shapes,[144] contradicting theories of γ-soft nuclear potential surfaces.[145]

Another recent development in the study of deformations describes the Coulomb excitation of collective states by a long range imaginary potential.[146] The remarkable merit of this approach is that a nontrivial theory with no free parameters can be evaluated without a computer, and gives specific cross-section predictions.[147] Indeed the beauty of *both* the above methods is the reliance on semiclassical, analytical methods, originally touted as the great virtue of heavy-ion collisions, but which fell into disrepute for a few years, to return *now* with renewed vigor.

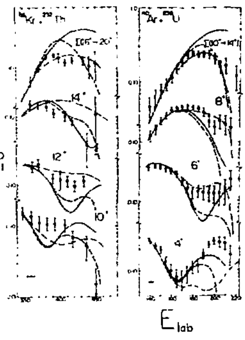

Figure 2.1

Figure 2.2

The discovery in 1971 of a pronounced irregularity around spin 16ħ (called backbending) in the otherwise very regular behavior of the rotational sequence of even-even rare earth nuclei, has opened up a vigorous research field in the study of high angular momentum in nuclei.[149,150] An illustration of the backbending phenomenon appears in Fig. 2.3.

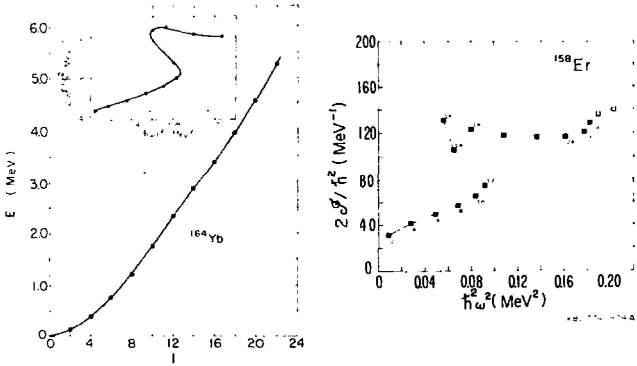

Figure 2.3

A slight discontinuity is evident in the plot of:

$$E_J \propto \frac{\hbar^2}{2\mathcal{J}} J(J + 1) \tag{2.2}$$

at $J = 14$. On the Variable Moment of Inertia model[151] we write:

$$E_J = \frac{\hbar^2}{2\mathcal{J}} J(J + 1) + \tfrac{1}{2} C \left[\frac{\mathcal{J}}{\hbar^2} - \frac{\mathcal{J}_0}{\hbar^2} \right]^2 \tag{2.3}$$

and

$$\frac{\mathcal{J}}{\hbar^2} = \frac{\mathcal{J}_0}{\hbar^2} + \frac{3}{4C} (\hbar\omega)^2 \tag{2.4}$$

Therefore a plot of moment of inertia versus the rotational frequency squared should yield a straight line. The Inset in Fig. 2.3 shows a marked departure from this trend, with a sudden increase in the moment of inertia.

Three effects have been given serious consideration as the causes for backbending. These are:[150]

- a collapse of the pairing correlations;[152]
- a shape change, i.e. change of deformation;[153]
- an alignment of the angular momenta of two high j nucleons with that of the rotating core.[154]

The fact that the moments of inertia of a most deformed nuclei are about one-half of the rigid body value is attributed to pairing correlations, which partly prevent the nucleons from following the rotation. It now appears more likely that backbending is due to the breaking of one pair rather than total pairing collapse (the gradual reduction of pairing appears rather to account for the

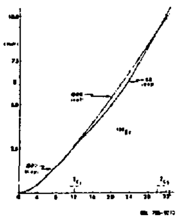

Figure 2.4

variable moment of inertia up to the backbend). The physical process involved in breaking the pair is the Coriolis force which forces the angular momentum vector j of the particle to decouple from the deformation (symmetry) axis and align with the rotation axis. In the $i_{13/2}$ orbit, for example, this effect gives a total of $12\hbar$ which can replace an equal amount of core rotational angular momentum.

On this model, at still higher angular momenta, additional pairs of high-j nucleons will tend to be aligned, and just such a discontinuity appears to be observed[155] in the $^{122}Sn(^{40}Ar,4n)^{158}Er$ reaction at 166 MeV, in which large amounts of angular momenta are deposited (Fig. 2.3). Here the second discontinuity at $J = 28\hbar$ appears to make a further step towards the formation of an oblate nucleus in which all the angular momenta is carried by aligned particles.[156] At the first backbend, two different rotational bands cross. Below the crossing, the levels belong to the ground state band, and above they belong to a superband with a larger moment of inertia. Another explanation of the *second* discontinuity operates from the assumption that if the superband is really based on an aligned two particle (high $j)^2$ configuration, then the superband should cross the ground state band not once but *twice*.[157] In this case, (see Fig. 2.4) beyond the second crossing, the lowest band is again the ground state band. A test of this model would be to follow the ground state band beyond the first crossing to see how the energies of these levels compare with the prediction.

The existence of two bands has been demonstrated *directly* in some cases by following the ground state band *beyond the backbending* region. Such is the case in ^{164}Er for which the γ-deexcitation spectra following Coulomb excitation with a ^{136}Xe beam, and the

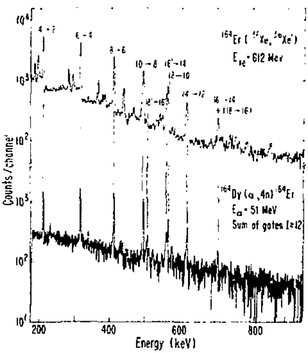

Figure 2.5

^{164}Dy(α,4n) reaction, are compared[158] in Fig. 2.5. The spectrum for (α,4n) demonstrates how backbending manifests itself experimentally, when a gate is set on a certain (high-J) transition and the coincidence E2 cascade to the lower levels is observed. It is clear that the transitions labelled 16'-14 and 18'-16' are "out of sequence" compared to the regular spacing of the 4-2, 6-4, 8-6 etc. transitions. Note, however, that in the upper part of the spectrum from Coulomb excitation there are, in addition, regularly spaced transitions 16-14, 18-16 which are the continuation of the ground state band *beyond* the J = 16 backbending region (compare Fig. 2.3). Only recently have sufficiently heavy beams become available to Coulomb excite very high spin states.

The rotation-alignment model actually predicts a *series of similar* rotation-aligned superbands. The lowest one discussed above has only even spin members, and evolves (in ^{164}Er) from a $K = 0^+$ band (at spin 0) to a structure at $I \geq 16$ which is mainly two $i_{13/2}$ quasineutrons coupled to J = 12, aligned with the core rotation. The next two superbands are predicted to start out as a single $K = 4^+$ band, evolving into the lowest odd spin (yrast odd) and the *second* lowest even spin (yrare even) rotation-aligned bands. They still have a dominant $(i_{13/2})$ configuration at high spin, and in the extreme limit, the rotation-alignment model predicts that yrast even-spin (I), the yrast odd-spin (I-1) and the yrare even-spin (I-2) states all have the same rotational energy. The structure of the superbands can be probed by studying their interactions with the ground and γ-vibrational bands. The higher lying γ-band is an excellent probe because it intersects both the even *and* the odd-spin states of the superbands. All these bands have been sorted out by a variety of (H·I,xn) coincidence experiments[159] (Fig. 2.6); an excellent and truly remarkable agreement between experiment (a) and theory (b) is observed.

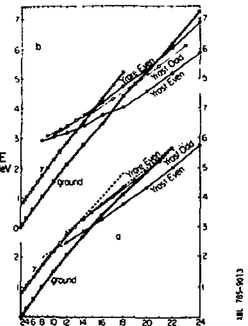

Figure 2.6

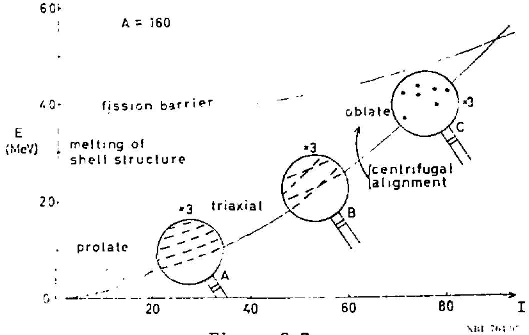

Figure 2.7

Guided by this introduction to high spin phenomena, let us now speculate[160,161] on the possible behavior of nuclei as even large amounts of energy and angular momentum are deposited (Fig. 2.7). The lower, approximately parabolic, line is the yrast line so there are no levels in the nucleus below this. The upper line gives the fission barrier, which sets an upper limit to the study of levels of the nucleus. The intersection of the two gives the effective *maximum angular momentum for the nucleus.* Nuclei in the rare earth region have prolate shapes near the ground state as a result of shell structure, and they have strong pairing correlations. The hatched region indicates where pairing correlations exist, which terminate as we have seen, around I = 20, where the two bands cross.

Some insight into the region above I = 20 comes from the liquid drop model. A rigidly rotating charged drop prefers an oblate shape until shortly before fission. The large moment of inertia of oblate shapes minimizes the total energy. Although the nucleus cannot rotate about a symmetry axis, it has been shown[162] that for a Fermi gas the states obtained by aligning the angular momenta of individual particles along the symmetry axis is the same as would be obtained by rigid rotation about that axis. These deformation-aligned states in oblate nuclei therefore generally are lower than the rotation-aligned states in prolate nuclei. At high angular momentum the nucleus becomes oblate and the angular momentun is carried by aligned individual nucleons (region C in the figure). This region may be identified by the occurrence of isomeric states,[160] due to the absence of smooth rotational band structure. At the very highest spins the nucleus may become triaxial before fission. The increase in deformation and moment of inertia is predicted to be so rapid that the rotational frequency will decrease, leading to a "super-backbend." Between the prolate and oblate regions, nuclei are also expected to become triaxial. Wobbling motion is then

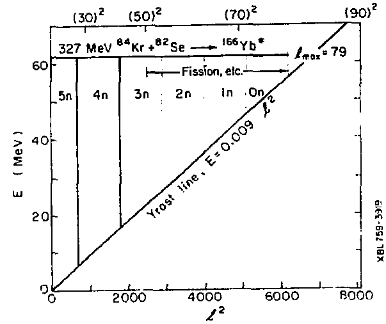

Figure 2.8

possible in addition to rotation about the axis with largest moment of inertia, and could give rise to a series of closely spaced parallel bands.[163] (Note that two aligned high-J orbits represent a triaxial bulge in prolate nuclei.)

How do we get an experimental handle on these new modes of *motion of the nucleus? The problem is to learn about high spin* states above l = 20, as discussed above, especially those along the yrast line, where the nucleus is thermally cool and does not have a high density of states. The remarkable feature of the (HI,xn) reaction is that it can locate us along different regions of the yrast line.[164-165] *This works as follows: in Fig. 2.8,* the compound nucleus ^{166}Yb is formed with an angular momentum distribution from $J = 0$ to $J = \ell_{max}$ at excitation energy $E_{CM} + Q \approx 60$ MeV by the partial cross sections:

$$\sigma_\ell = \pi\chi^2(2\ell + 1)\, T_\ell \tag{2.5}$$

The successive evaporation of x neutrons from these states is assumed to remove practically no angular momentum and an average of 2 MeV kinetic energy plus the binding energy of ≈ 8 MeV. Neutron evaporation continues until the available energy above the yrast line is less than 10 MeV. Since

$$E_y = \frac{\hbar^2}{2\mathcal{J}}\ell(\ell + 1) \tag{2.6}$$

a given value of x occurs in the sharply defined "bin" ℓ_i to ℓ_f where:

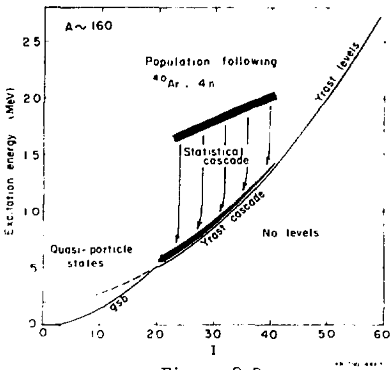

Figure 2.9

$$
\begin{aligned}
E_y(\ell_i) + 10 &= E_{CM} + Q - 10x \\
E_y(\ell_f) &= E_{CM} + Q - 10x
\end{aligned}
\tag{2.7}
$$

The partial cross section for the evaporation of x neutrons is then:

$$\sigma_x = \pi ƛ^2 \sum_{\ell_i}^{\ell_f} (2\ell + 1)T_\ell \approx \pi ƛ^2[\ell_f(\ell_f + 1) - \ell_i(\ell_i + 1)] \tag{2.8}$$

As long as $0 < \ell_i < \ell_f < \ell_{max}$, it follows that

$$\sigma_x = \pi ƛ^2 \frac{2\mathcal{J}}{\hbar^2} \cdot 10, \textit{ independent of } x . \tag{2.9}$$

(The largest and smallest bins can be truncated due to the limits $\ell_i = 0$, $\ell_f = \ell_{max}$.) Furthermore, the mean angular momentum $\overline{\ell}$ of the states on which the neuron evaporation chains terminate is predicted for each bin:

$$\overline{\ell} = \frac{2}{3} \frac{\ell_f^2 + \ell_f\ell_i + \ell_i^2}{\ell_f + \ell_i} \tag{2.10}$$

Channels corresponding to different numbers of evaporated neutrons have different angular momentum ranges and the highest angular

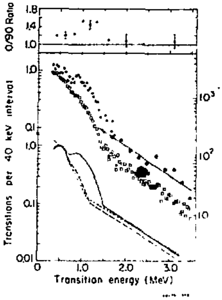

Figure 2.10

momenta are in the channels with the fewest evaporated neutrons. These results have been demonstrated experimentally.[166]

A specific application is shown[165] in Fig. 2.9 for the initial production of A ~ 160, with an Argon beam of 170 MeV. The initial excitation is 70 MeV and the 4n channel drops down to roughly 10 MeV above the yrast line, without removing much angular momentum. There is still a high density of levels, and there follows a high-energy statistical cascade of dipole transitions, which still do not carry off much angular momentum. Approaching the yrast line the level density becomes small; and the most likely mechanism is then stretched E2 transitions along the yrast collective bands. Eventually these run into the discrete levels of the ground state band (like Fig. 2.5). By setting gates on the lines corresponding to the 4n channel one can look at the corresponding spectrum in several NaI counters placed around the target.

The observed continuum spectrum for the $^{126}Te(^{40}Ar,4n)^{162}Yb$ reaction is shown in Fig. 2.10, by the hollow squares.[167] The dots show the corrected spectrum after efficiency unfolding. The exponential tail is associated with the statistical dipole emission, and the lower energy bump with the E2 cascade (confirmed by the anisotrophy shown at the top of the figure, obtained by comparing the spectra at 0° and 90°). The integral of the bump gives the number of gamma rays.

Then we determine the average angular momentum $\bar{\ell}$ carried in the cascades as

$$\ell = 2(\bar{N}_\gamma + \delta)$$

Figure 2.11

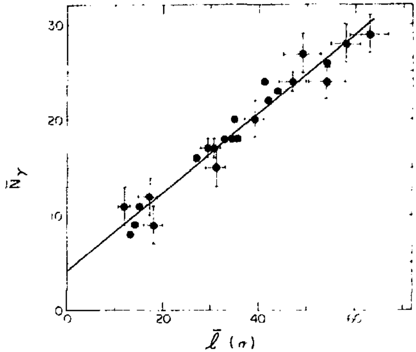

where δ is the number of statistical γ-rays removing no angular momentum. (Note however that some very recent measurements indicate that a dipole component is present in the yrast cascade, the precise origin of which is not understood.[168]) Our earlier theorems about the bins and the associated $\bar{\ell}$ of the different xn reactions, now enable the construction[165] of Fig. 2.11. The slope is not *exactly* one half, but close at 0.43. If we also associate the bump edge with transitions from the states of highest spin in the bin, we can determine the moments of inertia at these high spins from the relation:

$$E_\gamma = \frac{\hbar^2}{2\mathcal{J}}(4I - 2) \tag{2.11}$$

describing the transition energies in a rotor.

The results are shown[165,167] in Fig. 2.12 for ^{162}Yb, plotted in the backbending fashion of Fig. 2.3. Since ^{162}Yb has not been tracked completely through a backbend, ^{160}Yb is also shown (open circles). At the highest rotational frequency, the moment of inertia approaches the rigid sphere value with A = 162, $\mathcal{J} = 2/5\ MR^2$, $2\mathcal{J}/\hbar^2 \approx 140\ \text{MeV}^{-1}$. The last point on the plot is associated with the (^{40}Ar,4n) reaction, which as we saw earlier, originates from angular momentum ≈ 35ħ. Since the deformed moment of inertia would be a little larger (by 10%) and since the measured values fall below this line, some residual pairing correlations may still persist even at this high angular momentum.

A great deal of experimental ingenuity is presently invested in methods for unravelling the information about nuclear shapes at still higher rotational angular momentum. A promising technique[169,170]

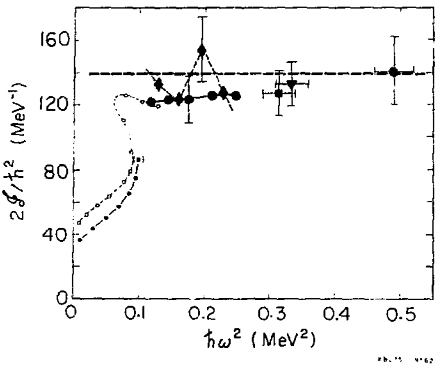

Figure 2.12

is to look at the multiplicity (the number of γ-rays) associated with each transition in the continuum. If there is some relationship, like:

$$E_\gamma = \frac{\hbar^2}{2\mathcal{J}} I(I+1)$$

at work this will be reflected as structure in the spectrum and imply a *prolate* nuclear shape. The absence of structure, on the other hand, is an indication of non collective motion and hence spherical or *oblate* shapes. An array of NaI counters is placed around the beam axis and the spectrum in another detector is unfolded in coincidence with one, two, three....counters of the array. Examples of coincidence and singles spectra for three reactions are shown in Fig. 2.13. (The singles spectrum shows the yrast and statistical cascades just as in Fig. 2.10.) In coincidence the yrast cascade yields a bump in the E_γ v multiplicity curve, the upper edge of which moves to higher energies as more angular momentum is brought in at higher incident energies (remember $E_\gamma \propto I(I+1)$). The spectrum is well reproduced in (b) with a cascade of $I/2$ rotational transitions from spin I to 0 whose energies are,

$$E_\gamma = \frac{\hbar^2}{2\mathcal{J}} (4I-2).$$

The data determine the moment of inertia to be 95% of the rigid sphere value. By contrast, the ^{100}Mo + ^{48}Ca example leads to nuclei in the N = 82 closed shell region, and the absence of structure in the multiplicity spectrum remains up to high spins. The rotational competition starts only at 50ħ, implying that this system is still

Figure 2.13

oblate up to this spin, and then becomes prolate. These trends are actually *in agreement with detailed calculations of potential energy* surfaces over the full (β,γ) plane, which use cranked modified-oscillator potentials with a Strutinsky-type normalisation to the liquid drop![171] Clearly we are on the way to finding out about the dynamics of nuclear rotation at very high spins indeed.

For a nucleus with oblate shape and with the angular momentum oriented in the direction of the symmetry axes, we encounter a form of rotational motion which is radically different from the usual prolate rotation. In the oblate case, the average density and potential remain static. (See Fig. 2.14.)

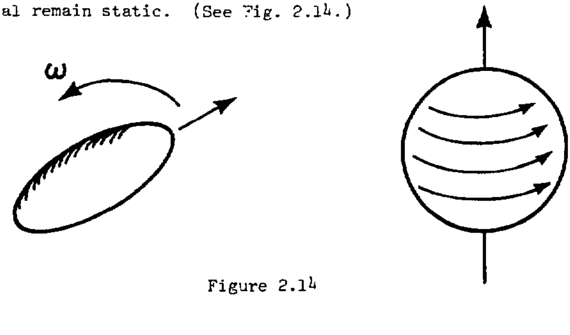

Figure 2.14

Each single particle orbit contributes a quantized angular momentum in the direction of the rotation axis. The transitions from one state to the next along the yrast line involve successive rearrangements in the filling of single particle orbits, and the energies along the yrast line exhibit irregularity, although on the average the yrast states have a rotational dependence of energy on spin with a mean effective moment of inertia equal to that of a rigid body rotating about the oblate axis of symmetry. The deviations from the mean, enhanced by shell effects, may cause large irregularities in the yrast sequence, and the nucleus may become trapped in isomeric states[160] with lifetimes orders of magnitude longer than rotational transitions. A systematic search for such yrast traps has been undertaken with beams of Ar, Ti and Cu in a hundred different target-projectile combinations.[172] The γ-emission from the recoiling compound nuclei were studied by detectors selecting high multiplicity (see above). The survey identified an island of high-spin isomeric states centered around neutron number 84 with lifetimes in the region of a few to several hundred nanoseconds. The interpretation will be quite speculative until the spin and decay schemes are pinned down, but it is fascinating to note that several theoretical calculations[171,173,174] point to this region of isotopes as especially favorable for the occurrence of yrast traps based on the oblate coupling scheme.

So far we have concentrated on γ-emission for transmitting information about nuclei at high angular momentum. However, once formed the compound nucleus has to decay by particle emission, from which important properties of the compound system become accessible, such as the temperature, distribution of angular momenta, moments of inertia, and degree of equilibration. Analysis of the data requires a comparison with the predictions of a statistical evaporation code. Remarkable progress has been made in refining the

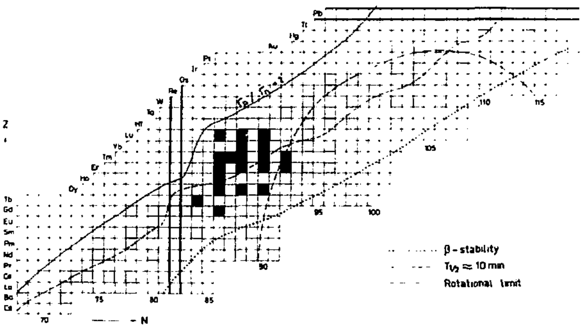

Figure 2.15

XBL 786-9019

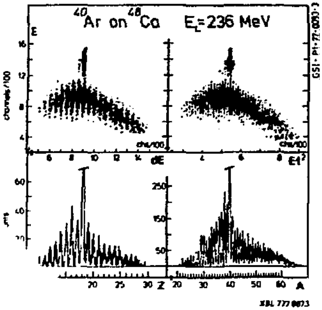

Figure 2.16

calculational[175,176] and experimental techniques. Experimental data and evaporation residues (the remnant of the compound nucleus after particle decay) can be obtained for individual A,Z by an apparatus which measures ΔE, E (to determine Z) and time-of-flight (to determine $A \propto Et^2$). A "state of the art" example is shown in Fig. 2.16 for $^{40}Ar + {}^{48}Ca$ at E = 236 MeV. In this particular experiment[177] evaporation residues were not being measured, but the figure demonstrates that it is possible to resolve individual Z up to 30 (in fact, up to 65 has been achieved) and individual A up to 60.

The measured evaporation residues in the reaction $^{19}F + {}^{27}Al$ at 76 MeV are compared with statistical calculations[176] in the bottom part of Fig. 2.17. The upper sections decompose the

Figure 2.17

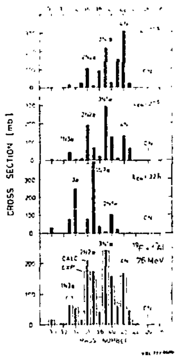

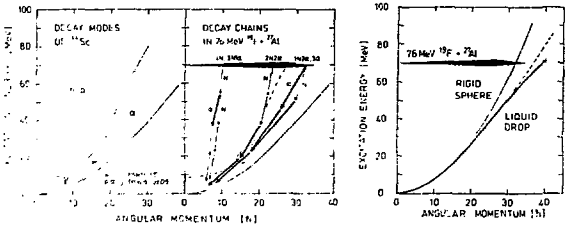

Figure 2.18

XBL 777-9678

calculation into contributions from different angular momenta in the compound nucleus. It is clear that increased α-particle emission is associated with higher angular momentum and therefore these residues probe the region of the energy-angular momentum space closest to the yrast line of the compound nucleus. A reconstruction of the "decay scheme" of the compound nucleus is shown in Fig. 2.18. (It is clear from this figure that our earlier discussion of the particle emission down to the yrast line producing the γ-cascades was oversimplified for light nuclei--see Fig. 2.9.

An important input to the statistical calculations is the level density in the nucleus at (in this example) excitations up to 70 MeV, and angular momenta up to 40ħ. Nuclei in this region are likely to behave like liquid drops, and the influence of individual shell structure of a nucleus on the level density and pairing energy vanishes. Based on theoretical predictions[178] one assumes in those calculations[179,180] that above a given excitation energy, U (liquid drop model) ≈ 15 MeV, the shell effects disappear. An appropriate allowance for the deformability under rotation is made by using:

$$\mathcal{J} = \mathcal{J}_o \, (1 + \delta L^2) \tag{2.12}$$

In this way we obtain an yrast line deviating from that of a sphere, as shown in the third section of Fig. 2.18. Because of the connection between the shape of the yrast line and the shape of the nucleus itself, information on the latter may be forthcoming from measuring the ratio between nucleon and α-particle emission (see the left-hand sections of the figure). The quantitative analysis yielded $2 \times 10^{-4} < \delta < 5 \times 10^{-4}$, which is to be compared with the prediction of 2.5×10^{-4} for the detailed shape calculation[181,182] (to be discussed in the next section).

Yet another method for extracting moments of inertia at high excitation and angular momentum is the measurement of coherence widths Γ. These can be evaluated in terms of the number of open

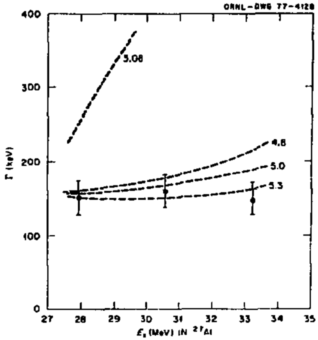

Figure 2.19 XBL 785-9012

channels (Hauser-Feshbach denominated) at a given compound nucleus J and of the level density in the compound system of (Ex,J) at excitation Ex. The slope of Γ versus Ex is primarily a function of the effective moment of inertia, via the spin cut-off parameter $\sigma^2 = \mathcal{J} T/\hbar^2$, with T the nuclear temperature.[183] For the $^{12}C(^{15}N,\alpha)^{27}Al$ system[184] a comparison of Γ v Ex in ^{27}Al is shown in Fig. 2.19 for different statistical model predictions labelled by $\mathcal{J}/\hbar^2$. The moment of inertia $\mathcal{J}/\hbar^2$ of 5.3 MeV^{-1} greatly exceeds[185] that extracted by fitting the low lying member of the ground state rotational band (≈ 3 MeV^{-1}). It will certainly be exciting to learn more about the predicted exotic shapes that nuclei, under the influence of heavy-ion collisions, will assume from experiments such as those described in the section. Since our whole discussion presupposed the formation of the compound nucleus, we must now check this assumption.

2.2 To Fuse or Not to Fuse

That is certainly a question at the forefront of much modern research with heavy ions. It is well known that if a deformable fluid mass is set spinning it will flatten and eventually fly apart.[182] To discuss the equilibrium shapes of a rotating nucleus we set up an effective potential energy and look for configurations that are stationary:

$$P.E = E_{Coul} + E_{nuc} + E_{rot} \qquad 2.13$$

where

$$E_{rot} = \frac{\hbar^2 \ell(\ell+1)}{2\mathcal{J}(\alpha_2\alpha_3\alpha_4)} \qquad 2.14$$

It is convenient to introduce two dimensionless numbers, specifying the relative sizes of the three energy components.[182,186,187] Choose the surface energy of a spherical drop as a unit:

$$E_S^{(0)} = 4\pi R^2\gamma = C_2 A^{2/3} \qquad 2.15$$

with $C_2 \approx 17.9$ MeV. Then specify the amount of charge on the nucleus by

$$x = \frac{\frac{1}{2}E^o{}_C}{E_S^o} \approx \frac{1}{50}\;\frac{Z^2}{A} \qquad 2.16$$

For the angular momentum, specify

$$y = \frac{E^o_{rot}}{E^o_S} \approx \frac{\frac{1}{2}\hbar^2\ell^2}{\frac{2}{5}MR^2}\cdot\frac{1}{C_2A^{2/3}} \approx \frac{2\ell^2}{A^{7/3}} \qquad 2.17$$

In terms of these parameters, Fig. 2.20 illustrates some shapes, in each case for the ground-state (stable) shape and the saddle point (unstable shape) — labeled H and PP respectively. As the rotation speed increases, the ground state flattens and the saddle point thickens its neck. In the bottom figure the ground-state pseudospheroid loses stability and becomes triaxial, resembling a

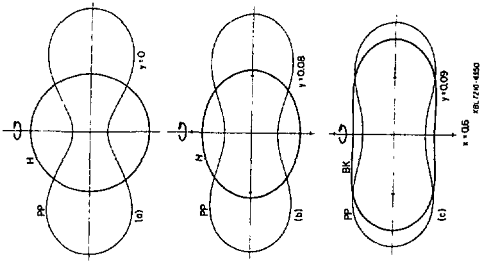

Figure 2.20

Figure 2.21

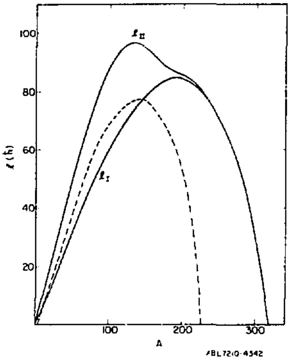

flattened cylinder with rounded edges, beginning to merge with the saddle shape. At slightly higher angular momenta the stable and unstable families merge and the fission barrier vanishes.

This behavior can be translated into an angular momentum plot versus mass (Fig. 2.21). For vanishing of the fission barrier the resultant curve is ℓ_{II}. No nucleus can support more than $100\hbar$, and neither light nor heavy nuclei can support very many units. The dashed curve shows the angular momentum required to lower the fission barrier to 8 MeV; this curve is indicative of the maximum the nucleus could support and still survive the risk of fission in the de-excitation process.

By conservation of energy and angular momentum, it follows that the closest distance of approach of projectile and target is given by r_{min}, where for impact parameter b,

$$\left(\frac{b}{r_{min}}\right)^2 = \left(1 - \frac{V}{E}\right) \qquad 2.18$$

which, for given r_{min}, is a hyperbola for b^2 versus E. If r_{min} is chosen as the strong interaction radius (R_1+R_2), this curve divides the plane (b v E) into two regions: distant collisions where the nuclei pass each other without appreciable interaction, and close collisions where the corresponding πb^2 gives the reaction cross section. Because of diffuseness, this region is given some width in Fig. 2.22. The curves are constructed for R_1+R_2+d. The plane can be further subdivided by curves corresponding to the locus of fixed angular momentum ℓ:

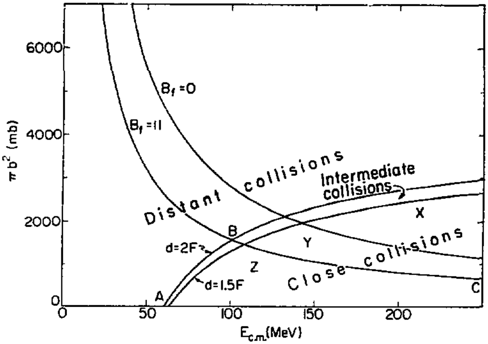

XBL7210-4343

Figure 2.22

$\ell = b\sqrt{2\mu E}$ $\qquad$ $b^2 = \dfrac{\ell^2}{2\mu}\ \dfrac{1}{E}$ $\qquad$ μ = reduced mass

The value of b (or ℓ) at which the fission barrier vanishes can be inserted to construct the additional curves on Fig. 2.22 (both for zero fission barrier and where it has become equal to the binding energy of a nucleon, which marks where the de-excitation mode changes to nucleon emission and the compound nucleus would be detectable).

To the left of B_f=0, a compound nucleus could form, and to the left of B_f=11 it would definitely survive. We shall see later however that the prediction of the *formation* of a compound nucleus

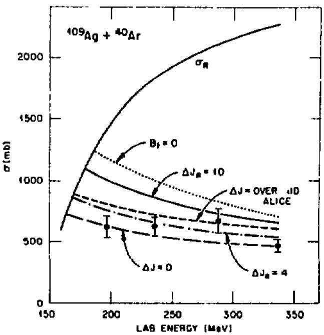

Figure 2.23 XBL 785-9011

is a dynamical question, beyond the scope of these considerations. Only if this critical curve lies *totally* above ABC, can the curve ABC represent the cross section for formation and survival of the compound nucleus. The figures are constructed for $^{20}Ne+^{107}Ag$. Now we compare with actual data[188] for a much heavier system, $^{40}Ar+^{109}Ag$.

The fusion products are experimentally identified by detecting evaporation residues after evaporation of nucleons and alpha particles[189] and are shown in Fig. 2.23; the trend follows that of Fig. 2.22. The line $B_f = 0$ is marked and also more precise calculations using the computer code ALICE, which deals more properly with particle evaporation, and in particular with the angular momentum they carry off (represented by $\Delta J = 10$ etc). Detailed discussions of the fusion of heavy systems are given in the reviews of Refs. 190 and 191.

In many cases we find that the fusion cross section is much less than the reaction cross section, although the fission barrier has still not disappeared. It appears that the ions have to reach a critical *distance* of overlap of nuclear matter before fusion sets in.[192,193] To take into account the effects of a critical distance we write[194] for the fusion and the total reaction cross sections:

$$\sigma_f = \pi \lambda\!\!\!^{-2} \sum_{0}^{\infty} (2\ell+1)\, P_\ell \qquad 2.20$$

$$\sigma_R = \pi \lambda\!\!\!^{-2} \sum_{0}^{\infty} (2\ell+1) \qquad 2.21$$

where P_ℓ are the probabilities that fusion takes place after the barrier is passed. For P_ℓ we assume:

$$P_\ell = \begin{cases} 1 & \ell \leq \ell_{cr} \\ 0 & \ell > \ell_{cr} \end{cases} \qquad 2.22$$

Then the summation in Eq. 2.20 leads to

$$\sigma_f(E) = \pi \lambda\!\!\!^{-2} (\ell_{cr}+1)^2 \approx \pi \lambda\!\!\!^{-2} \ell_{cr}{}^2 \qquad 2.23$$

The turning point for the partial wave $\ell = \ell_{cr}$ is deduced from the expression:

$$E = V(R_{cr}) + \frac{\hbar^2 \ell_{cr}(\ell_{cr}+1)}{2\mu R_{cr}^2} \qquad 2.24$$

Substituting for ℓ_{cr} in Eq. 2.23, gives

$$\sigma_F = \pi R_{cr}^2 \left(1 - \frac{V(R_{cr})}{E}\right) \qquad 2.25$$

This expression is just equivalent to the usual formula for the reaction cross section (see for example Eq. 2.18) with R_{cr} replaced by the interaction barrier radius R_B:

$$\sigma_R = \pi R_B^2 \left(1 - \frac{V(R_B)}{E}\right) \qquad 2.26$$

It turns out that $R_{cr} \approx 1.00\ (A_1^{1/3} + A_2^{1/3})$ for a wide range of ions. *This interpenetration distance corresponds to the overlap* of the half density radii of the nuclear matter distributions.[195] The radius is marked[196] on Fig. 2.24 for $^{16}O + ^{48}Ca$. Up to a certain critical energy, for all partial waves that surmount the outer barrier, the two ions succeed in interpenetrating to the critical distance (assuming there is not too much radial friction near the barrier top -(dashed line) and fuse. Above this critical energy, however, the increasing centrifugal barrier does not allow the ions to penetrate for all partial waves, and the fusion cross section becomes smaller than σ_R. (This scheme is valid when the dynamical path for fusion lies inside the saddlepoint, a situation which is not usually fulfilled for heavy systems — see the discussion in Ref. 30).

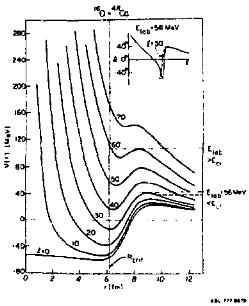

Figure 2.24

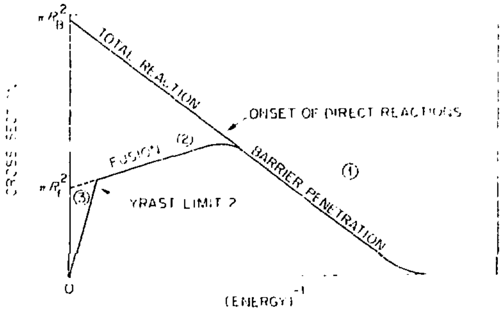

Characteristic Energy Regions for Fusion.

XBL 777 9660

Figure 2.25

From these equations we generate the schematic representation[107] of fusion and total reaction cross sections as a function of 1/E in Fig. 2.25. In region 2, the critical energy is passed and the fusion cross section changes slope — it may increase, stay constant or decrease, depending on the value of $V(R_{cr})$ at this point. In region 3, the limit of maximum angular momentum in the compound system is surpassed. Just these features appear to be observed[108] in $^{14}N+^{12}C$ system shown in Fig. 2.26. If the data are represented in terms of the critical angular momentum, as in Eq. 2.22, then the value $\ell_{cr}(\ell_{cr}+1) = 734\hbar^2$ does indeed correspond to the limit of $26.6\hbar$ expected from Fig. 2.21 for $A \approx 26$. The predicted shape is that of a very deformed, triaxial nucleus with $R_{max} \approx 2R$ and $R_{min} \approx 0.4R$, with R the radius of the spherical ground state. In view of these extreme shapes, it is perhaps more realistic to

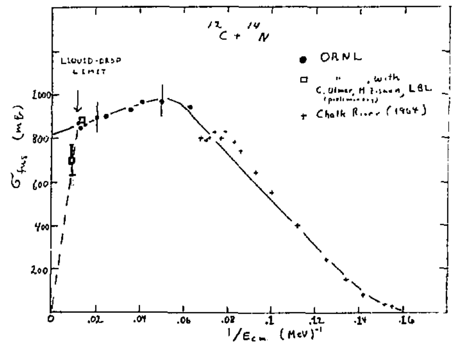

Figure 2.26

consider[199] a critical deformation, or moment of inertia, which determines whether fusion occurs or not; in a more formal derivation[104] R_{cr} is introduced via the equation $\mathcal{J}_{cr} = \mu R_{cr}^2$. The study of much heavier systems, beyond the liquid drop fission limit, should soon be possible with the higher energies becoming available.[200]

Since the slope and intercept beyond the critical energy determine V_{cr} and $R_{cr} \approx 1.0(A_1^{1/3} + A_2^{1/3})$, these measurements can be used to determine the potential at much smaller distances than is possible from elastic scattering[52] (we call $R_{1/4}$ and R_s in Lecture 1), and indeed were used to construct some of the points in Fig. 1.14. A thorough analysis of potentials, synthesizing information from the total reaction cross section, the fusion cross section, elastic and transfer reactions is given in Ref. 34; such an approach may help to remove the ambiguities we discussed for $^{16}O+^{28}Si$ in Lecture 1. However if there is significant radial friction (and the next lecture will show that there is) then our earlier equations should contain $(1 - \frac{V+E_F}{E})$ rather than $(1-\frac{V}{E})$, where E_F is the energy loss due to friction on that portion of the trajectory leading up to the barrier. Roughly we can see that neglect of friction produces an underestimate of the potential.[52] At the critical distance where frictional dissipation is very strong the whole method of analysis presented here becomes questionable. Nevertheless a variant of this analysis,[53] using a proximity potential has been used to extract potential depths down to values of s (in Fig. 1.14) which are negative, i.e., very strong overlap of the nuclear matter. A questionable assumption in many of these treatments is the sudden approximation, i.e., a potential which conserves the structure of each nucleus.[201] At the opposite extreme is the adiabatic approach, which allows a continuous change of potential.[202] Ultimately a full dynamical calculation is required, in which the fusion cross section depends not only on the static shapes but also on coupling to internal degrees of freedom.[203-206] In the classical limit this approach leads to an equation of motion with frictional forces.[207] Then it becomes possible to describe in complete fusion events, or deeply-inelastic scattering; in the next lecture we shall see that these processes consume the missing cross section[208] of region 2 in Fig. 2.25.

2.3 More Microscopic (and Speculative) Aspects

In our introduction to these lectures we mentioned that the microscopic, and the macroscopic were not really distinct subjects, but so far in our discussion of fusion processes we have ignored any effects of individual nucleons, the fundamental constituents of nuclei. In Fig. 2.27 is a plot of the $^{40}Ca+^{40}Ca$ fusion cross section,[209] plotted in our familiar framework. In the notation of Eqs. 2.25, 2.26, the solid line uses the parameters,

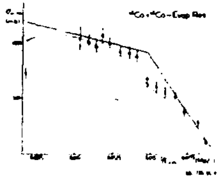

Figure 2.27

$$V(R_B) = 51.5 \text{ MeV}, \quad R_B = 1.49\ (A_1^{1/3} + A_2^{1/3}) = 10.2 \text{ fm}$$

$$V(R_{cr}) = 24 \text{ MeV}, \quad R_{cr} = 0.97\ (A_1^{1/3} + A_2^{1/3}) = 6.65 \text{ fm}$$

The critical potential is positive, which classifies the system as "heavy" (compare Fig. 2.26 where it is negative). Since this system comprises two closed-shell nuclei, the tightness associated with shell effects could manifest itself by a decrease of the radius parameter, compared with neighboring systems; such a comparison could give some information on the role of individual nucleons in the fusion process. The dashed curve in fact corresponds to a calculation with a smaller critical distance determined from Hartree-Fock densities for ^{40}Ca. One physical interpretation of the critical radius comes from the two-center shell model.[210] This is illustrated in Fig. 2.28 for $^{16}O+^{16}O$; at distances less than 3.4 fm the lowest configuration becomes the ground state of ^{32}S and at large distances it is the $^{16}O+^{16}O$ ground state. At the level crossing, strong energy losses should occur. It would appear from Fig. 2.27 that there is no evidence for this closed-shell effect. However, another doubly magic system $^{48}Ca+^{208}Pb$ does

Figure 2.28

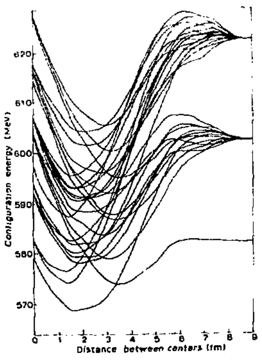

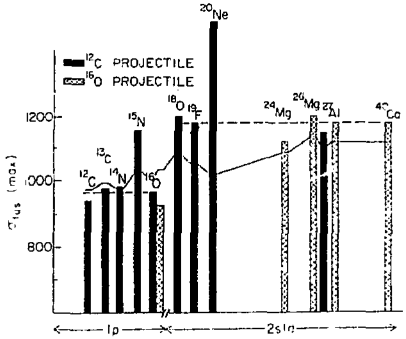

Figure 2.29 XBL 786-9017

indicated[illegible] a lowered fusion cross section.

In lighter nuclei, there is some evidence for a shell effect. For example, in Fig. 2.29 the valence nucleons of a new oscillator shell appear to cause a discontinuous jump in cross section of 100 mb at the sd-shell. Unfortunately the systematic trend is broken[illegible] by one point for ^{15}N,[213] and also by some recent results with ^{20}Ne.[illegible] The microscopic aspects, and the exact manner in which the valence nucleons affect the fusion cross section via the complexity of Fig. 2.28 is still poorly understood. An even more challenging observation is the presence of oscillations in the fusion cross sections of light, closed shell systems,[212,214] such as ^{12}C + ^{12}C and ^{12}C + ^{16}O, whereas the ^{12}C + ^{18}O system behaves according to the systematics we have described in section 2.2.

Figure 2.30

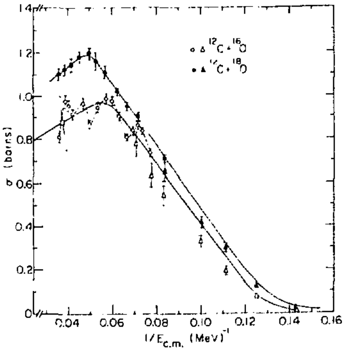

XBL 777 9682

Some examples are shown in Fig. 2.30. The story becomes even more subtle with the observation that these oscillations are correlated with the resonances appearing in the excitation functions $^{12}C + {}^{12}C \rightarrow {}^{12}C(2^+) + {}^{12}C(2^+)$, which, as we discussed in the first lecture, have been attributed to molecular shape resonances.[12[illegible]] (See Fig. 1.27) (For a detailed discussion, see Ref. 211.) Even the association with closed shell systems, and/or even partial waves, appears dubious with the recent observation[215] that the oscillations are *also* present in $^{14}C + {}^{16}O$, ^{12}C.

To return to the $^{40}Ca + {}^{40}Ca$ system, which did not exhibit shell effects, it is conjectured that fast, collective excitations[216] could provide the first step in overcoming the shell gap before adiabatic effects (such as level crossings) become important. In this model, the two nuclei move on trajectories constrained by the proximity potential, and at the turning point of the radial motion dissipate energy into vibrational and intrinsic motion. Fusion happens predominantly close to the orbiting angular momenta, and a satisfactory description of the data in Fig. 2.27 is obtained.

The smaller impact parameters tend to make the ions bounce off one another, a feature which is also present in the time dependent Hartree-Fock Model.[217-219] So far we have been largely concerned with the "macrophysics" of nuclear matter. Of course this is not a new subject, since fission has been with us for a long time. But there have not been many studies of the *dynamics* of fission. It has mostly been an attempt to understand the energetics and other properties of the fission barrier. Is it possible to get some understanding of all these processes in some microscopic framework? A convenient starting point is the mean field or Hartree-Fock approximation, which has enjoyed great success in the static case.[[illegible]] This works because the density is high, the effective forces are strong, and the Pauli principle inhibits collisions. In a time-dependent generalization the rate of change of the mean field must be small enough so that it does not produce large excitations of the independent particles in a short time. The kinetic energy per nucleon should not be too large compared to the Fermi energy ($\approx$30 MeV). The last lecture will carry us beyond this regime.

The TDHF equations for the single particle wave functions ψ_n are given by

$$i \frac{\partial}{\partial t} \psi_n(\underline{r},t) = H(t)\psi_n(\underline{r},t)$$

$$H(t) = -\frac{\hbar^2}{2m} \nabla^2 + V(t) \qquad (2.27)$$

and V(t) is an integral over the two-body interaction calculated

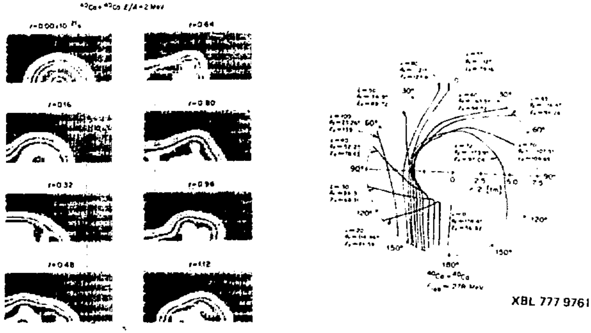

Figure 2.31

self-consistently with the single particle wave functions. At each instant of time one has to calculate a mean field produced by the influence of all other particles. As the solutions are stepped in time, the self-consistent field is simply the Hartree-Fock potential at the previous step. The initial systems are represented by a product of single particle wave functions calculated in a moving potential; after the collision, one needs a mixture of both sets of wave functions.

A computer display of the density distributions of these calculations for ^{40}Ca + ^{40}Ca at 8 MeV/nucleon in a head-on collision is shown in Fig. 2.31(a), as a function of time.[218] (Because of the symmetry the complete picture should be visualized with an identical pattern below the bottom axis and to the left of the vertical axis.) The contour stripes mark density intervals of 0.04 nucleons/fm^3. We see that taking these calculations at face value (which is premature regarding the state of the art) the nuclei do not fuse, but separate after 0.65×10^{-21} sec oscillating in a predominantly octupole mode. In earlier stages of the diagram all the aspects of fission dynamics, including the neck formation and scission, are in evidence. In Fig. 2.31(b), a "trajectory diagram" is constructed showing the final energy and scattering angle for different partial waves. The small waves "bounce" backwards up to ℓ = 30. Some waves fuse and others go into partial orbiting with deflection to negative angles. (This diagram is considerably more sophisticated than our sketch in Fig. 1.6, but it contains the same information.) As shown in Fig. 2.32, the calculation using TDHF Force III gives a reasonable description[221] of the Ca + Ca fusion data.

The possibility that low partial waves do not fuse (i.e., that there is a lower cut-off in partial wave as well as an upper) is an

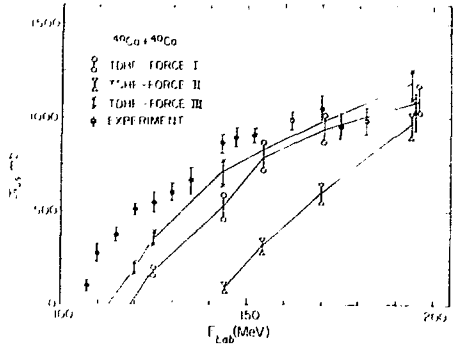

Figure 2.32 XBL 786-9016

idea that has been around in the literature for some time.[191, [illegible]] A detailed study was made of evaporation residues from the formation of the compound system ^{158}Er by comparing the results of different formation experiments ^{16}O + ^{142}Nd, ^{40}Ar + ^{118}Sn, ^{84}Kr + ^{74}Ge, and ^{63}Cu + ^{96}Zr (the last giving a slightly different compound nucleus). The excitation functions for a particular evaporation channel [illegible] are shown in Fig. 2.33. We recall from the "bin diagram" of Fig. 2.8 that this channel should be associated with the *same excitation energy region* of the compound nucleus, regardless of how it was formed, but the evidence in Fig. 2.33 clearly indicates a shift in the onset of this decay channel for the heavier projectiles. (The thresholds are indeed found to be identical for different light projectiles, C, O, and Ne.) Figure 2.8 also reminds us that the lower energy part of the curve must be associated with the low

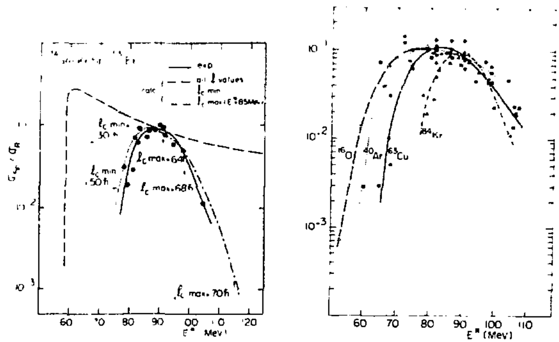

Figure 2.33

XBL 777-9760

[illegible] population, since all the available excitation energy has to be removed by five neutrons. For the Kr case in Fig. [illegible], the large shift in the threshold implies a [illegible] population of the compound nucleus. The quantitative [illegible] in Fig. [illegible](b) indicates that $J_{lower} \approx$ [illegible] would [illegible] there is a J_{upper} [illegible] in this example [illegible].

The implied lower ℓ cut-off is at variance with experiments which measure the fusion cross section via average quantities [illegible] the evaporation residues, or the number of [illegible]-rays in the de-excitation of the residues.[228] [illegible] suggestion for the resolution of this paradox is that the apparent thresholds for specific xn channels in the Ar and Kr bombardments may be [illegible] by the presence of non-equilibrium effects in the decay of the evaporation residues. There is certainly evidence for signs of forward-peaked [illegible] [illegible] fusion [illegible] at low angular momenta. [illegible] from low ℓ values is then shifted [illegible], and [illegible] the question of a lower cut-off is still not finally [illegible].

[illegible] Superheavy Elements

The [illegible] of heavy-ion fusion have been discussed, and it will [illegible] no surprise that fusion into superheavy elements has presented enormous obstacles. Schiffer has described the problem in a picturesque metaphor.[229] Suppose you lived in the age of Columbus and you were convinced that his idea of finding an easy trade route to the East Indies was wrong. There were plenty of clever geographers who calculated that the earth was much larger, or that it was flat....and he would never make it to India. Should he have been discouraged? He would certainly have missed something interesting that turned up on the way! Without the elusive goal of Superheavy Elements, perhaps we would have missed some of the discoveries described in this lecture--and the next.

Despite intensive searches in major laboratories in the U.S., U.S.S.R., Germany and France, no evidence for superheavy elements in nuclear reactions have been found (for a recent review see Refs. [illegible]). (Brief successes[232] in Monazite inclusions were short-lived.[illegible]) Upper limits for the cross sections are shown on the left side of Fig. 2.34. Most of the limits are obtained by failing to detect any spontaneous fission activity; one event would correspond to the quoted cross sections, and it is questionable whether the methods would make us believe one event. Some other experimental techniques, and their attainable limits, are illustrated on the right. It seems clear that one must turn to methods capable of exploring shorter lifetimes and (preferably) yielding higher cross sections particularly since the most

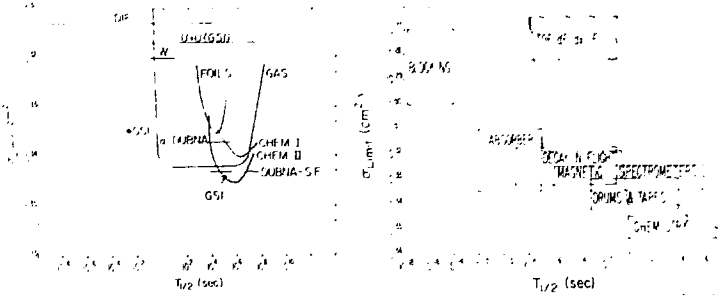

Figure [illegible]

The most [illegible] combination [illegible] + [illegible] with [illegible] results.

There may be a way, by bombarding Uranium with Uranium. [illegible] is a plot of the total kinetic energy [illegible] different [illegible] collision as a function of the Z of the observed fragment. [illegible] The two horizontal lines indicate the total available kinetic energy and the Coulomb repulsion energy for spherical fragments; the

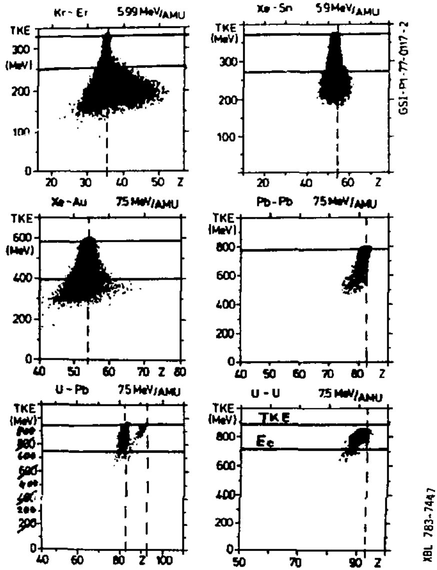

Figure 2.35

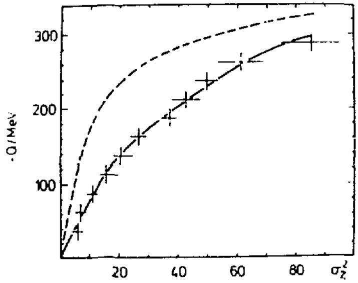

Figure [illegible]

[illegible] mark the projectile [illegible]. The principle feature of the [illegible] reactions is that the width of the Z distribution increases with energy loss. This trend can be explained in a diffusion [illegible] an increased interaction time [illegible] be discussed in the next lecture). The functional relationship for systems such as [illegible] + A [illegible] shown in Fig. [illegible] by the dashed line. The encouraging feature is that this curve does not apply to U + U (solid line) [illegible] smaller energy loss for a given σ_Z, and therefore less [illegible] for the product to fission. To set a scale, the difference between the two curves is 10 orders of magnitude in the production [illegible] for element 114, but the calculated cross section [illegible] two orders of magnitude smaller than the present limit [illegible]. We devote the whole of the next lecture to a discussion [illegible] reaction, known as Deeply-Inelastic Scattering.

[illegible] DEEPLY-INELASTIC [illegible]

[illegible]tions, nuclear reactions—induced by either light [illegible] classified into two *extremes*. In quasi-elastic [illegible], a few nucleons were exchanged between target and [illegible] of kinetic energy was small, and the [illegible] a minor perturbation [illegible] system. [illegible] other hand, the projectile was completely [illegible] the target, and all the initial kinetic energy [illegible] intrinsic excitation energy, or carried away [illegible] particles. We know now that such a treatment [illegible] hierarchy of intermediate processes [illegible] reactions, there is a well-developed theory [illegible] reactions intermediate between [illegible] In heavy-ion reactions, a similar interme- [illegible] called deeply-inelastic scattering. [illegible] theoretical approaches [illegible] phenomena will lead the way [illegible] light or heavy, at higher [illegible] history of nuclear physics [illegible] the study of deeply-inelastic scattering will [illegible] new directions in nuclear physics. [illegible] captured the imaginations of nuclear [illegible] and theorists all over the world, who have [illegible] traditional research areas in droves. They have created a [illegible] which by sheer size alone inspires awe. There are many [illegible] the new reaction process—quasi-fission, damped [illegible], partially-relaxed phenomena, deeply-inelastic scattering and, [illegible] they are Characteristic of Heavy-Ion Processes,[illegible] [illegible] suggested a new compromise which captured [illegible] processes, of FISSION CHIPS, but it does not appear [illegible] been accepted. Recently I noticed a misprint[illegible] in a [illegible] Review Letter, which introduced a new word to the English language, FUSSION. Since deeply-inelastic scattering is betwixt and between fusion and fission, I now suggest a new name, FUSSION CHIPS, a [illegible] dialectic variant of this English delicacy!

3.1 *The Phenomenon*

To see why "fussion *chips*" is an appropriate terminology, let us look at some of the paths taken by heavy-ion collisions[22] as they have *emerged* in the first two lectures (see Fig. 3.1). The time scale is in units of $\tau = 10^{-22}$ sec. It shows how the composite system may proceed towards compound nuclear formation, preceded and succeeded by particle emission, and possibly ending in symmetric fission. *But there is also a new path*, where the composite system *never* fuses completely; rather, it separates on a relatively short time scale into two fragments, reminiscent of the initial ions which *went* into partial orbit. (Is there a connection with the

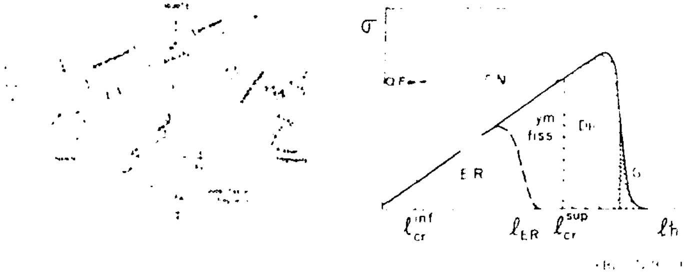

Figure 3.1

[illegible] This is the new [illegible] reaction [illegible] The [illegible] line represents [illegible] For high partial waves [illegible] with [illegible] direct reactions such as transfer and [illegible] Then at [illegible] the onset of [illegible] For the upper ℓ-values, [illegible] primarily by fission; [illegible] lower [illegible] survives to emit particles and lead to [illegible] Finally there may exist a lower boundary where the [illegible] result (possibly) in other [illegible]

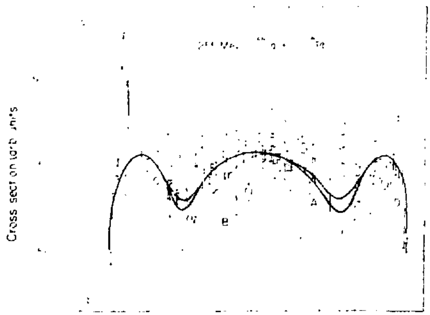

XBL 779-2016 A

Figure 3.2

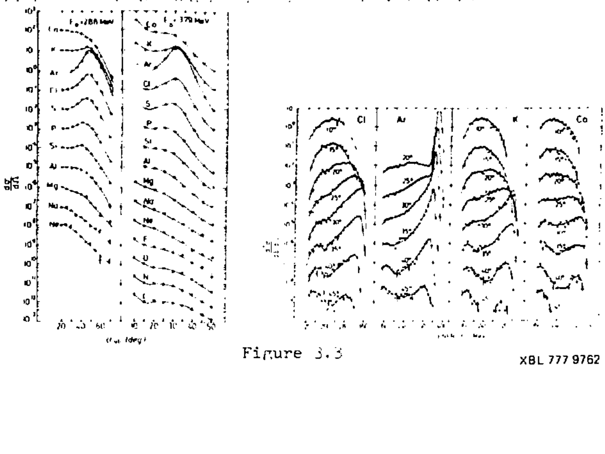

Figure 3.3

XBL 777 9762

[illegible]

[illegible] illustrated [illegible] alternative interpretations [illegible] explained in [illegible]. The [illegible] grazing collisions, in the region [illegible] compare [illegible] peak. Between the grazing and [illegible] are [illegible] by the [illegible] the two [illegible] form a *temporary dinuclear* system [illegible] form [illegible] nucleus, which happens [illegible] the [illegible] in the last [illegible] contour plot [illegible] then [illegible] with *negative angle scattering*. The longer the [illegible] and the greater the angle of rotation, the more the [illegible] distributions approach the form [illegible]. Figure [illegible] transfers will occur during the time the two [illegible] contact and the magnitude of the exchange is [illegible] with the kinetic energy dissipation and with increasing [illegible]. A comparison of the contour plot in Fig. [illegible] with those in Fig. [illegible] shows that the detailed behavior depends strongly on the Z_1Z_2 product of the colliding system. For [illegible] for example the angular distributions become broader with significant fractions *backwards* of the grazing angle, indicative of a grazing angle, Coulomb dominated deflection.[246] A critical parameter is the reduced Sommerfeld parameter,

$$\eta' = \frac{Z_1 Z_2 e^2}{\hbar v'} \quad .$$

Here v' is the velocity of the two ions at the interaction barrier. The quantity is roughly the ratio of the Coulomb force $Z_1 Z_2 e^2/R^2$ and the frictional force (responsible for dissipating the initial kinetic energy) which is proportional to the velocity and the product of the nuclear densities $\propto 1/R^2$. Systems with $\eta' \lesssim 150$-200 give rise to orbiting whereas those with $\eta' \gtrsim 250$-300 do not.[247] Another important parameter defining the characteristic behavior is the ratio E/B of the center of mass energy to the Coulomb barrier.[248] (Some of the many extensive reviews on the subject of deeply-inelastic scattering are given in Refs. 249-254.)

Before proceeding further with the logical analytical predictions of the rotating, dinuclear model, we must describe some experiments relating to direct experimental evidence for its validity. An important aspect is that these reactions are basically binary processes, and this has been established by coincidence measurements of the projectile and target-like fragments (see e.g. Ref. 255).

Another consequence of Fig. 3.4 is that the direction of rotation of the quasi-elastic (positive angle) and deeply-inelastic (negative angle) fragments should be opposite. Further, in a classical picture of a peripheral collision, we expect the angular momentum to be oriented perpendicular to the reaction plane. For the quasi-elastic transfer, the semi-classical model discussed in Lecture 1 gives some predictions[66,67] of the polarization. Evaluating λ_2 from the Eq. 1.43 and substituting Eq. 1.44 gives:

$$\ell_{eff} \approx \frac{\lambda_1 \hbar v}{R_1} - \frac{\hbar v}{R}\ \frac{k_o R}{2} \approx \frac{\lambda_1}{R_1}\hbar v - \tfrac{1}{2} m v^2 \qquad 3.1$$

Since the incident nucleus is left in a hole state of the transferred particles, the sign of its polarization should just be opposite to λ_1. Vanishing polarization is predicted at the "optimum Q-value", best satisfying the semi-classical matching conditions:

$$Q_{opt} = -\tfrac{1}{2}\, m v^2 + (Z_1^f Z_2^f - Z_1 Z_2^i) e^2/R \qquad 3.2$$

If $Q > Q_{opt}$, the polarization is negative and if $Q < Q_{opt}$, it is positive. (For a more detailed investigation using DWBA theory see ref. 256).

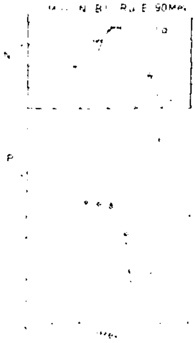

Figure 3.5

[illegible] these features have been studied[257,258] in the reaction $^{100}Mo(^{14}N, ^{12}B)^{102}Ru$ at 90 MeV by measuring the β-decay asymmetry of the $^{12}B(J^{\pi} = 1^{+}$, $E_{\beta max}$ = 13.37 MeV, $t_{1/2}$ = 20.3 ms). The angular distribution of β rays with respect to the polarization $\underline{P}$ is given by $W(\theta) = 1 - P\cos\theta$. The apparatus is sketched in Fig. 3.6(a). The beam irradiation was cyclic and on alternate cycles the spin direction of the ^{12}B was reversed with an RF field to eliminate instrumental asymmetries. The results are shown in Fig. 3.5(b). We see that the energy spectrum of the ^{12}B (determined for N_{β}) peaks in the continuum at a Q-value of ≈ −23 MeV, compared to $Q_{opt} - \frac{1}{2}mv^{2} + \Delta V_{c}$ ≈ −21 MeV. Calculations for both the energy spectrum and the polarization are shown. The value of P indeed reaches zero at the peak of the distributions, but for more negative Q-values the values of P do not become sufficiently positive. Therefore, for these larger energy losses, we need a process tending to give additional polarization of the opposite sign, e.g. deeply-inelastic scattering.

For the ^{40}Ar + Ag system at 300 MeV quasi- and deeply inelastic processes are clearly separated. The polarization of the fragments

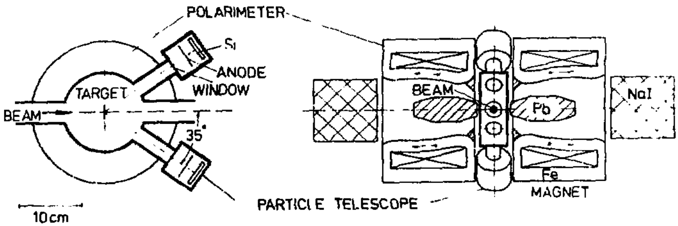

Figure 3.6

XBL 786-9069

[illegible] projectile and target fragment spin in the same direction, has been determined[29] from the circular polarization of the subsequent de-excitation γ-radiation. The direction of polarization can be measured by scattering the emitted γ-rays from the polarized electrons in magnetized iron. (Remember the classic experiment demonstrating parity violation in weak interactions.) The experimental apparatus, sketched in Fig. 3.6, used two polarimeters in a magnetic field [illegible] normal to the scattering plane defined by the two [illegible] counters at 45°, which detected the fragments. The observed polarizations are consistent with the dinuclear positive and negative angle scattering model, although the absolute values are less than expected. I have described both these experiments in some detail because they are characteristic of the sophistication of techniques in current use.

One of the striking characteristics of deeply-inelastic scattering is the rapid dissipation of the initial kinetic energy into internal excitation on a time scale comparable to direct reactions. The complete equilibration hypothesis implies that the composite system reaches a common temperature and divides into fragments with excitation energies proportional to their thermal capacities (mass). In a recent analysis of the ^{86}Kr + ^{124}Sn reaction at [illegible] and [illegible] MeV incident energies, this division has been convincingly demonstrated.[illegible] The bottom part of Fig. 3.7 shows the observed average mass of each projectile-like element emitted (upper triangles for [illegible] MeV, lower for 720 MeV). Since we are interested in the difference in mass numbers at each Z, the ordinate has been expanded by making zero equal a mass division having the same Z/A as the composite system (achieved by subtracting 201/86 Z_f). If the observed products really represented the primary fragments, the points would all line up at zero for complete relaxation; indeed the solid points are an attempt at reconstruction of the primary

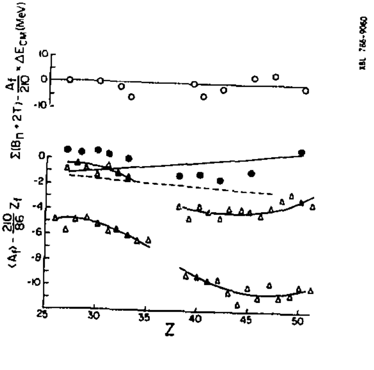

Figure 3.7

distribution for the lower energy, and the straight lines are other theoretical reconstructions. The fact that the data are displaced from zero is simply a reflection of the subsequent neutron emission of the excited prefragments, and these displacements therefore contain information on this excitation energy. The displacement [illegible] is just related to the difference in partition of the extra [illegible] MeV difference of the center of mass energies of internal excitation. If this energy is divided in proportion to the masses, the fragment A_L should receive the fraction [illegible]. As the upper part of Fig. [illegible] shows, this quantity is indeed equal to [illegible], where the summation is over the [illegible] neutron difference seen in the [illegible] part of the figure, [illegible] is the neutron binding energy and [illegible] is the average kinetic energy of the emitted neutron. The temperature T was estimated [illegible] equilibration of the energy. Clearly the clustering of the points around zero confirms the division of energy in the [illegible] manner.

The examples we have discussed in this section should indicate the [illegible] inventiveness and imagination in the study of heavy-ion reactions. Now we proceed to discuss the underlying mechanisms [illegible] the large and fast damping of the energy, and the [illegible] degrees of freedom.

[illegible] Energy Dissipation in Deeply Inelastic Scattering

Two [illegible] theories are currently in vogue to explain the dissipation of large amounts of the initial kinetic energy into intrinsic excitation of the dinuclear complex. Since they approach the problem from the antithetical viewpoints of one-body dissipation and collective dissipation, it is likely that the ultimate truth will involve a synthesis, just as our understanding of nuclear structure involves single particle and collective aspects. We should recall that the transition between direct and compound nuclear processes is not unique to heavy-ion reactions. A typical energy spectrum for a light-ion reaction (e.g., (p, p')) appears[261,262] in Fig. 3.8. The energy spectrum can also be regarded as a time variable; the low energy compound region corresponds to a long interaction time and the high energy direct region to a short time. There is a continuous evolution from direct and multistep direct reactions to compound nuclear reactions. The relationship to heavy-ion reactions becomes plausible if we compare the evolution of the differential cross sections in Fig. 3.3 and those of Fig. 3.9, which pertains to direct and multistep reactions leading to *discrete final states*.[196,263] In this type of reaction the microscopic techniques we discussed in Lecture 1 are well developed and there is hope that similar approaches can be applied to heavy-ion reactions.[264-266]

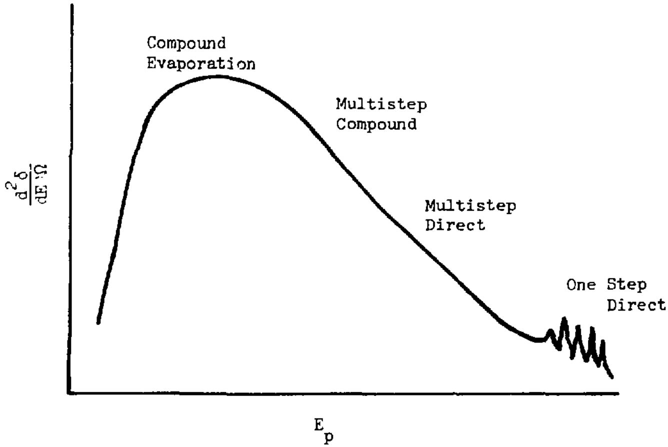

Figure 3.8

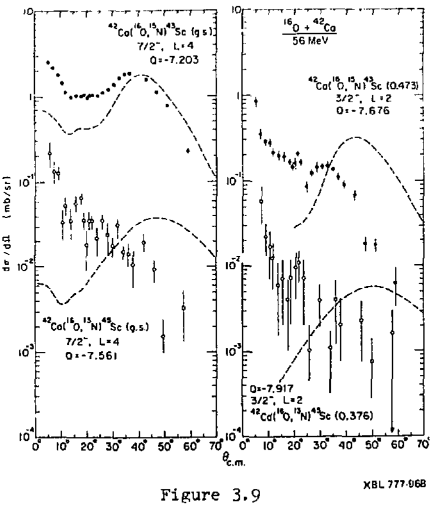

Figure 3.9

In searching for a fast dissipative mode, we are led naturally to think of giant multipole excitations. The dipole resonance has a characteristic time of 10^{-22} sec, and is one of the fastest motions known in nuclear physics. There are two characteristic times in heavy-ion collisions. The first is the time during which the nuclei are in contact, i.e.

$$\frac{\tau_{coll}}{\hbar} \approx \left[\frac{E}{A}\left(1 - \frac{V_c}{E}\right)\right]^{-\frac{1}{2}} \text{MeV}^{-1} \qquad (3.3)$$

For collisions not too far above the barrier this time is of the order [illegible] MeV^{-1} ($\approx 6 \times 10^{-22}$ sec). *The second one measures the* degree of adiabaticity of the process, which is concerned with the time, τ_{char}, over which the form factor changes by a factor of two. For peripheral collisions τ_{char} may be an order of magnitude shorter than τ_{coll}, i.e. $\approx 6 \times 10^{-23}$ sec. The quantum transitions, that can take place during the collision, are therefore limited adiabatically to have $\Delta E \lesssim \hbar/\tau_{char} \approx$ 10-20 MeV. This region of excitation is just where the major fraction of the sum rule for inelastic excitation of giant resonances is exhausted.[267] A number of theoretical papers deal with these modes as the mechanism for deeply inelastic scattering,[268] via multistep excitation.

From the experimental point of view one might hope to get a clue about the role of these modes by looking for structure in the deeply inelastic continuum. So far this has appeared as a featureless bump, but more refined data for the Ca + Ca and Cu + Cu at approximately 300 MeV, acquired with a magnetic spectrometer, reveal quite a complex structure. (See Fig. 3.10: (a) for Ti isotopes from Ca + Ca; (b) for Zn isotopes from Cu + Cu, and (c) ^{63}Cu produced in Cu + Cu; the total excitation energies are also indicated).

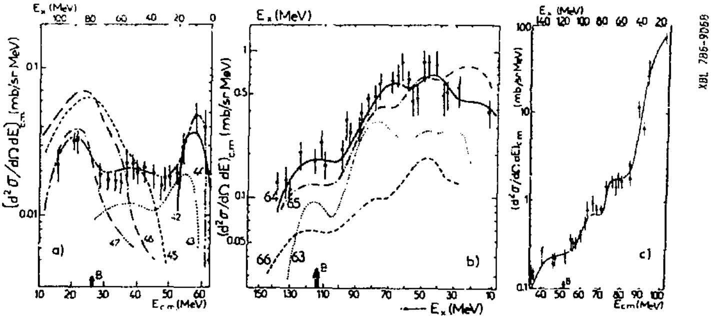

Figure 3.10

Even more pragmatically, we might look for the direct excitation of giant multipoles in inelastic heavy-ion scattering. The probability that either fragment will emerge in a single giant resonance depends, however, on the system. For heavy systems, the large energy loss implies a dominance of multiple excitation, but for lighter systems, the shorter collision times and the higher excitation, lead to stronger single excitation. The E2 mode has been observed in $^{16}O + {}^{27}Al$,[270] $^{16}O + {}^{208}Pb$,[271,272] and ^{12}C, ^{14}N + Zr, Pb.[273] For the $^{16}O + {}^{27}Al$ system, Fig. 3.11(a) shows the excitation probability for different regions of θ, together with the ratio (shaded) for excitation of the giant quadrupole resonance compared to everything else.[274] Even for this light system the probability is unexpectedly small, and it remains to be seen if the quantitative models[268] account for the strength. In (b) is shown a "Wilczynski Plot" for the inelastic scattering (compare Fig. 3.4) which also shows the ridge, between -7 and -20 MeV, characteristic of deeply-inelastic scattering and negative angle scattering.

Finally an example of E2 excitation for $^{16}O + {}^{208}Pb$ at 315 MeV is shown[272] in Fig. 3.12. Both at 140 MeV and at 315 MeV, the observed strength apparantly exhausts the energy weighted sum rule;[271] therefore the multiple step excitation of the deeply-inelastic continuum (a cross section of 400 mb at 135 MeV[275]) does not reduce the single excitation, possibly raising an element of doubt over the role of these resonances for the damping. Further comparisons at different energies are required. An interesting feature of Fig. 3.12 is the appearance of higher lying structures. The frequency of oscillation of multipole modes can be derived[275] from the liquid drop model to depend on the multipolarity as $\ell^{3/2}/A$; for quadrupole oscillations $\omega_2 \cdot \hbar \approx 0.8$ Mev. An evaluation of ω as a function of ℓ and A, tells us that the associated

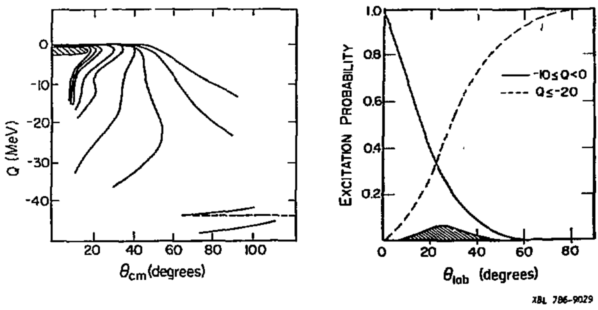

Figure 3.11

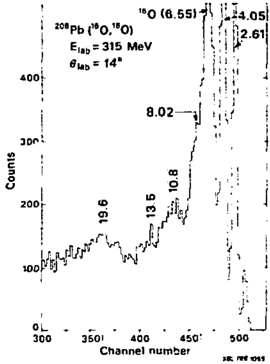

Figure 3.12

velocities, v = ω·R, will call for collision speeds in excess of 20 MeV/A for the excitation of higher lying multipoles, which may therefore be appearing in Fig. 3.12. (The giant quadrupole resonance corresponds to the bump at 10.8 MeV.)

Now let us turn to the alternative energy dissipation mechanism via single particle motion. In this picture, as the two nuclei rotate in close contact, an exchange of nucleons takes place through the window that opens up in the neck between them. Consider the nuclei as containers in which the nuclei have a random motion. A nucleon in nucleus 1 can escape through the neck and be absorbed by nucleus 2, and vice versa. Let the area of the interface of the composite system be A(t), and the window integral in the reaction,

$$\bar{A}\Delta t = \int_{orbit} A(t)\, dt \tag{3.4}$$

The probability per second that a nucleon crosses the interface from 1 to 2 is $n_{12}A$ and similarly from 2 to 1 is $n_{21}A$. These rates depend on dynamics and are functions of time. This dependence will be weak if the number of transferred nucleons is much less than the total. So say n_{ik} is constant. Then the variance of the number transferred is:

$$\delta n = \left[(n_{12} + n_{21}) \int A(t)\, dt\right]^{1/2} \tag{3.5}$$

while the flow of mass from 1 to 2 is

$$\langle n \rangle = (n_{12} - n_{21}) \int A(t)\, dt \tag{3.6}$$

and the normalized distribution of the number transferred might be expected to be a Gaussian,

$$P(n) = \frac{1}{\sqrt{2\pi}\ \delta n} \exp - \left[\frac{(n - \langle n \rangle)^2}{2\delta n^2} \right] \tag{3.7}$$

Now a good guess for the transfer rate is:

$$n_{12} \approx n_{21} \approx \frac{1}{6} \rho v \tag{3.8}$$

where ρ is the nuclear matter density, 0.17 nucleons/fm^3, and $v \approx 9 \times 10^{22}$ is the typical speed of a nucleon inside the nucleus. With an interface area of $\bar{A}$ = 10 fm^2 and a typical direct reaction time of $t \approx 5 \times 10^{-22}$ sec for the collision of ^{40}Ar on ^{50}Ti at 236 MeV,[177] we get $\delta n \approx 5$. The Z and A distribution of fragments in this reaction are illustrated in Fig. 3.13 (which were obtained by combining the Z and A information of Fig. 2.16) and we see that the spread in A values is indeed *the order* of δn. (It is difficult to see the Gaussian profiles in the 2-D plot, but such indeed are the observed shapes.)

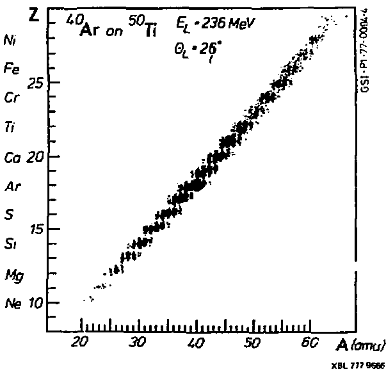

Figure 3.13

3.3 More Formal Theory

The theory presented here will be only slightly more formal, with an emphasis on the extraction of physical quantities from the data. Rigorous approaches are described in other Lectures of this School. The generalization of the discussion in the previous section to diffusion processes in the rotating dinuclear system leads to the Fokker-Planck equation[251,253,277,278] for the population distribution of a macroscopic variable x as a function of time, P(x,t):

$$\frac{\partial P(x,t)}{\partial t} = -v\,\frac{\partial P(x,t)}{\partial x} + D\,\frac{\partial^2 P(x,t)}{\partial x^2} \tag{3.9}$$

the solution of which is:

$$P(x,t) = \frac{1}{\sqrt{4\pi Dt}}\exp\left[-\frac{(x-vt)^2}{4Dt}\right] \tag{3.10}$$

The mean value of the distribution x moves with time at constant velocity, and the variance $\sigma^2 = \langle x - \langle x\rangle\rangle^2 = 2Dt$ increases linearly with time (see Fig. 3.14). The transport coefficients v and D are known as the drift and diffusion coefficients. The FWHM of the curve is given from $\Gamma^2 = 16\,\ell n\,2(Dt)$. Amongst the macroscopic variables which have been measured are kinetic energy, the N/Z degree of freedom and the mass asymmetry degree of freedom $A_1 - A_2/A_1 + A_2$.

As an example of how these methods work,[279,280] consider the charge distribution as a function of angle. This can be derived

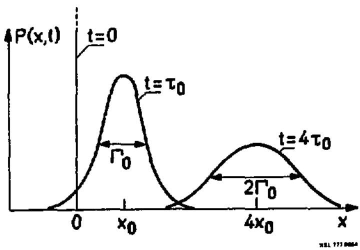

Figure 3.14

from an analysis of distributions of cross sections such as Fig. 3.3 for each Z. They would be expected to have Gaussian distributions,

$$P(z,t) = \frac{1}{\sqrt{4\pi D_z t}} \exp\left[-\frac{(z - z_o - v_z t)^2}{4D_z t}\right] \tag{3.11}$$

where $z - z_o$ stands for the number of protons transferred during the interaction time t. The quantities v_z and D_z represent average proton drift and diffusion coefficients. In order to relate *angle* information to *time* information we write,

$$\tau_{int} = \frac{1}{\bar{\omega}}(\theta_{gr} - \theta) \tag{3.12}$$

where τ_{int} is the interaction time for the rotating dinuclear system, rotating with mean rotational frequency $\bar{\omega}$. (The rotation is measured from the grazing angle.) Now,

$$\bar{\omega} \approx \frac{\hbar \ell}{\mathcal{J}} \tag{3.13}$$

where $\mathcal{J}$ is the moment of inertia of the system, and

$$\bar{\ell} \doteq \frac{2}{3}\,\frac{\ell_g^3 - \ell_{crit}^3}{\ell_g^2 - \ell_{crit}^2} \tag{3.14}$$

where we attribute deeply-inelastic collisions to the band of partial

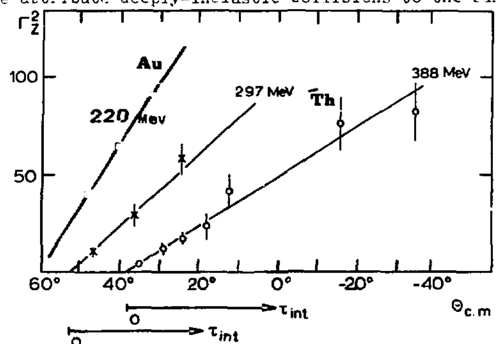

Figure 3.15

XBL 777-9672

waves from ℓ_{crit} (inside of which fusion takes place) to ℓ_g (see Fig. 3.1).[281]

For the reaction Ar + Th depicted in Fig. 3.3 at 388 MeV, ℓ_g and ℓ_{crit} have been determined as 222 and 94 respectively.[243] For $\mathcal{I}$ we can assume rigid body rotation of the dinuclear complex:

$$\mathcal{I} = \frac{2}{5} M_1 R_1^2 + \frac{2}{5} M_2 R_2^2 + \mu R^2 \quad . \tag{3.15}$$

The plot of Γ^2 versus θ in Fig. 3.15 can then be regarded as a plot of Γ^2 versus $\tau_{int} = t$, and the slope $\Gamma^2/t \propto D_Z$. In fact, the same value of D_Z is derived for the different reactions studied at different energies (on the figures, the t-scale is different for the different reactions, since this is transformed by $1/\bar{\ell}$). The derived value was $D_Z \approx 10^{22}$ (charge units)^2/sec. Other quantities can be determined by similar analysis. One finds typically:[251,277]

$$\text{Energy drift coefficient } v_E \approx 4 \times 10^{23} \text{ MeV/sec}$$

$$\text{Energy diffusion coefficient } D_E \approx 4 \times 10^{24} \text{ (MeV)}^2\text{/sec}$$

$$\text{Charge drift coefficient } v_z \approx 10^{21} \text{ (charge units)/sec}$$

$$\text{Charge diffusion coefficient } D_z \approx 10^{22} \text{ (charge units)}^2\text{/sec}$$

These values are not expected to be very accurate due to the crude method of estimating the interaction time. In a more refined approach[282] a better relation between impact parameter ($\equiv \ell$) and scattering angle is derived by constructing a proper deflection function. Energy and angular momentum dissipation are taken into account. Interaction times calculated in this way can vary by a factor of 3 from the simple estimate.

A characteristic of the deeply-inelastic collision is the large energy damping. This energy loss also appears to take place rapidly while the two ions are in contact. On a microscopic picture the energy loss could be mediated by particle-hole excitation and also by transfer of nucleons between the colliding ions. Such a nucleon, with mass m, deposits a momentum $\Delta p = m|\dot{r}|$, where $\dot{r}$ is determined from the energy of the system prior to the transfer, and the *resultant energy loss is therefore proportional to the energy available* ($\delta E \propto (\Delta p)^2$). This argument justifies the introduction of a frictional damping force proportional to the velocity[279,283-285]

$$F_t = -kv \tag{3.16}$$

Then we can write for the rate of energy loss:

$$\frac{dE}{dt} = \mu v \frac{dv}{dt} = v \cdot F = -kv^2 = -2 \frac{k}{\mu} E \qquad (3.17)$$

Integrating the expression,

$$\ln\left(\frac{E_o}{E}\right) = 2 \frac{kt}{\mu} \qquad (3.18)$$

Now we have just shown that a time scale is established by the relation $t = \Gamma_Z^2/2D_Z$, and therefore we expect that there should be a linear relation between $\ln(E_o/E)$ and Γ_Z^2: the gradient yields a value for $k/\mu D_Z$. As Fig. 3.16(a) dramatically demonstrates,[280] there certainly is a clear correlation between the width of the charge distribution and kinetic energy loss, which is shown on this figure for successive 50 MeV wide bins in the reaction of Bi + Xe.

In Fig. 3.16(b), the values of σ_Z^2 from Fig. 3.16(a) are plotted as a function of the interaction time $\tau(\ell)$ in units of 10^{-22} sec, and appear to increase linearly, i.e., $\sigma_Z^2(\ell) = 2D_Z(\ell)\,\tau(\ell)$. The time scale on the figure was derived from the deflection function. This deflection function was constructed by assuming a sharp cut-off model, where the cross section up to ℓ_j is given by $\sigma_j = \pi\lambda^2(\ell_j+1)^2$. Then using the experimental results on the cross section as a function of kinetic energy loss, the angular momentum can be related[286] to the energy loss by:

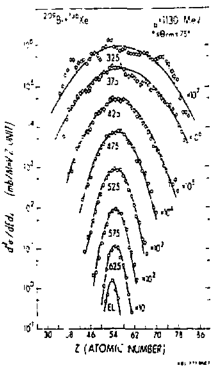

Figure 3.16(a)

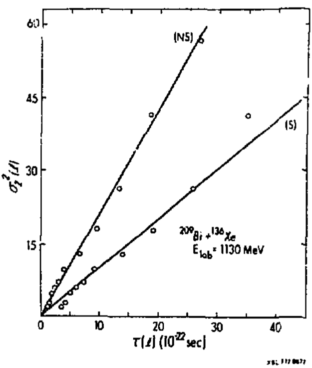

Figure 3.16(b)

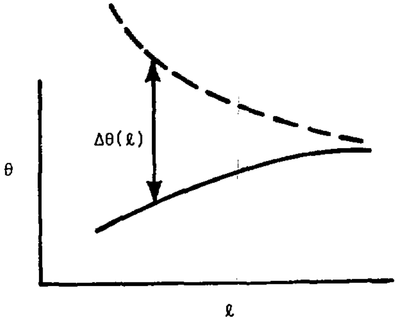

Figure 3.16(c)

$$\ell_i = \left[(\ell_j+1)^2 - \frac{\Delta\sigma_{ij}}{\pi\lambda^2}\right]^{1/2} - 1 \qquad (3.19)$$

where $\Delta\sigma_{ij} = \sigma_j - \sigma_i$ is the cross section in an energy window between E_i and E_j. The average scattering angle for a particular energy loss is also an experimental quantity (see Fig. 3.4), so the curve of θ versus ℓ can be deduced as in Fig. 3.16(c). The angular momentum dependent interaction time is then calculated from the expression[287,288]

$$\tau(\ell) = \frac{\Delta\theta(\ell)\,\mathcal{J}(\ell)}{\hbar\ell} \qquad (3.20)$$

where $\Delta\theta$ is the difference between the Coulomb deflection angle (dashed) and the actual reaction angle. From these results we extract the values of Γ_Z^2 (the FWHM of the Gaussian functions in Fig. 3.16(a)) as a function of E and construct the plot shown in Fig. 3.17, which is indeed remarkably linear. Since we previously deduced a value of D_Z we can now use these results to calculate the coefficient of friction $k = 0.6 \times 10^{-21}$ MeV sec fm^{-2}. (A much more sophisticated treatment involving deformation is given in Ref. 289.)

It is instructive to see how the large value of k can be understood,[276] using the simple model of matter transfer discussed earlier in section 3.2. Suppose that the speed of nucleus 1 relative to 2 is tangential and equal to v_t. The rate of nucleon "hits" from 2 to 1 through the window is:

$$\frac{dn}{dt} = \frac{1}{2}\rho v A \cos\theta\, p(v) \qquad (3.21)$$

where θ is the inclination of the *nucleon* speed v, of distribution p(v). Each nucleon of mass m deposits the excess momentum $-mv_t$, and therefore the average force acting in the tangential direction is:

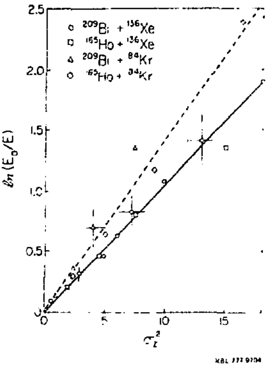

Figure 3.17

$$F_t = -\frac{1}{2} m\rho A v_t \int_0^{\pi/2} v\, p(v)\, \cos\theta\, \frac{d\Omega}{2\pi}\, dv \tag{3.22}$$

$$\approx -\frac{1}{4} m\rho A v_t\, \bar{v}$$

By identifying this expression with the fruction force -kv, we derive that

$$k \approx \frac{1}{4} m\rho A\bar{v} \tag{3.23}$$

Assume, as in Equ. 3.5, a window area of $A \approx 10\ \mathrm{fm}^2$, and the average nucleon speed $\bar{v} = 3/4\ v_F \approx 3/16\ c$ and the nucleon density of nuclear matter, $0.17\ \mathrm{fm}^{-3}$. Then:

$$k \approx 200\ \mathrm{MeV/fm \cdot c} \tag{3.24}$$

i.e., 0.7×10^{-21} MeV sec fm^{-2}, in good agreement with the value extracted from experiment! In fairness, however, we must note that comparable agreement can be reached[90] using the relation,

$$\frac{dE}{dt} = \frac{dE}{dn} \cdot \frac{dn}{dt} = \langle \Delta E \rangle \frac{2}{\hbar} W \tag{3.25}$$

where $\langle \Delta E \rangle$ is the average loss per collision, taken as a typical giant resonance excitation and W is the imaginary optical potential, deduced from direct reactions (Lecture 1).

A more careful examination suggests that the agreement with the one body dissipation mechanism may be less than perfect.[291,292] Remember that the basic tenet of this model is expressed via the relation:[293,294]

$$\delta E = \frac{m}{\mu} E \qquad (3.26)$$

where δE is the loss of kinetic energy per nucleon exchange and E is the available energy at that time. (This equation is quite consistent with our earlier equations. Thus in equ. 3.17 we can write $dE/dt = \delta E\, dn/dt$ where dn/dt is the nuclear flux, and by the analysis leading to equ. 3.22 this is just $2k/m$; hence the above result for δE. The validity of the equation relies on weak coupling of intrinsic and collective degrees of freedom, an assumption that has been challenged.[295]) Now δE must be deduced from the experimental data (Fig. 3.17) which essentially gives energy loss as a function of σ_Z^2. Regarding the nucleon exchange process as a random walk process, the number of protons exchanged is just $N_Z = \sigma_Z^2$. The experimental observation of the fast equilibration of the mass to charge asymmetry degree of freedom indicates that neutron and proton exchange rates must be very similar[242] and therefore the total number of nucleons exchanged is $N = (A/Z)\,\sigma_Z^2$. Differentiation of the curve of E v σ_Z^2 with respect to $(A/Z)\,\sigma_Z^2$ leads to $\delta E = dE/dN$, which is plotted versus $\frac{m}{\mu}E$ in Fig. 3.18. The dashed line represents the one body dissipation of Equ. 3.26 and it appears that this mechanism accounts for only 30% of the energy loss. Before attributing the additional loss to other mechanisms such as the fast collective dissipation, discussed in section 3.1, the whole validity of the analysis must be examined. It has been pointed out, for example, that the relation between angular momentum and energy implied by eqn. 3.19 is oversimplified,[296] and a more rigorous treatment may remove the discrepancy with the one body dissipation model.

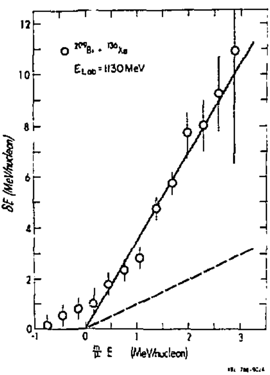

Figure 3.18

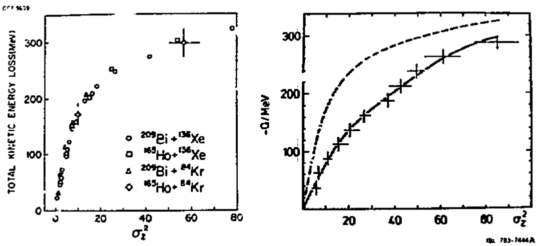

Figure 3.19

The simple approaches have nonetheless given great encouragement to the researchers on superheavy elements, as we mentioned briefly at the end of Lecture 2. It has been found that the curve of energy loss v. $\sigma_Z{}^2$ (represented in Fig. 3.19, with a different ordinate from Fig. 3.17) is not universal. For U + U, as shown in the right hand portion, a much wider charge distribution is found.[237] This observation has important repercussions for making superheavy elements, where the problem is to keep the excitation energy low enough for survival against fission. Consider[230] as an example $^{238}U(^{238}U,\ ^{181}Yb^*)^{295}SH_{114}{}^*$. For a relative fission width $\Gamma_f/(\Gamma_f+\Gamma_n)$ of 50% the excitation energy of the superheavy must be about 30MeV. Assuming partition of the energy according to the mass (as we justified in Section 3.1) the Yb nucleus then carries 18 MeV and the total excitation energy is 48 MeV. The Q-value for the reaction is -55 MeV, so we can tolerate a total energy loss of 103 MeV and still have reasonable survival probability. From Fig. 3.19, the associated charge variance is $\sigma_Z^2=14$. The cross section can then be calculated from $(114) = \sigma_0(92)\ \exp(-(\Delta Z)^2/2\sigma_z{}^2)$ for a total kinetic energy window of ± 10 MeV, $\sigma_o(92)$ is 4 mb and with $\Delta z = 22$, we obtain $\sigma(114) = 10^{-34}\ cm^2$.

The hope of reaching the Holy Grail of superheavy elements will no doubt stimulate more accurate calculations of the production cross sections. There is much to be done. The mechanisms of dissipation we have discussed may be adequate for the early stages of deeply-inelastic reactions, where the window is open, i.e., whenever there is solid contact between the ions. There is also "two body" friction, analogous to viscosity in liquids.[297] More generally, a friction force of the type we have been discussing can be represented[298] as:

$$F = -k \int d^3 r \, \rho_1 \rho_2 \, |\dot{\bar{r}}| \qquad 3.27$$

where ρ_1 and ρ_2 are the density distributions of the two nuclei and the integral is taken over the overlap region. The rate of dissipation has also been calculated using a proximity formalism (rather similar to our discussion of proximity potentials in Lecture 1), with the result[294,299,300]

$$\frac{dE}{dt} = 4\pi \frac{n_o}{\mu} \frac{R_T R_P}{R_T + R_P} b\chi(\xi_o)E \qquad 3.28$$

where $n_o = 2.5 \times 10^{-23}$ MeV•sec•fm^{-4} is the transfer flux density, R and b are the nuclear half-density radius and diffuseness, and $\chi(\xi_o)$ is a universal flux function. An application of this formalism to the above reactions for Kr and Xe on heavy targets yields[242]

$$\frac{1}{E}\frac{dE}{dt} \approx 10^{21} \chi(\xi_o) \approx 0.7 - 2.1 \times 10^{21} \text{ sec}^{-1} \qquad 3.29$$

which is actually in very good agreement with the value of $2k/\mu \approx 2 \times 10^{21}$ sec which follows from Fig 3.17.

3.4 Dynamical Aspects

The previous section was intended to give the flavor of the approaches to understanding the diffusion processes in deeply-inelastic scattering. The evidence strongly suggests the idea of an intermediate complex consisting of two well defined fragments in contact, undergoing equilibration, and the time constants of these relaxation processes have been determined. Now we consider the transfer of orbital angular momentum into the rotation of the two fragments constituting the complex. The angular momentum transfer induced by the frictional forces passes through several stages.[298] Initially, a sliding friction term makes the two bodies start to roll on each other, and then a rolling friction term causes the two bodies to get stuck in rigid rotation.

At the onset of sliding the moment of inertia characterising the system is simply

$$\mathcal{J}_{NS} = \mu R^2 \qquad 3.30$$

where μ is the reduced mass and R the distance between the centers of the fragments. For the sticking configuration (using the theorem of parallel axes) the moment of inertia is

$$\mathcal{J}_S = \mu R^2 + \mathcal{J}_1 + \mathcal{J}_2 \qquad 3.31$$

where $\mathcal{J}_{1,2}$ are the moments of inertia of the fragments, $2/5\, M_i R_i^2$. The *maximum* value $\Delta\ell$ of orbital angular momentum transformed into intrinsic spin can then be calculated from $\ell_i \mathcal{J}_{NC} = \ell_f \mathcal{J}_S$ as

$$(\ell_i - \ell_f) = \Delta\ell = \frac{(\mathcal{J}_S - \mathcal{J}_{NC})}{\mathcal{J}_S}\ \ell_i \qquad 3.32$$

which appears as *intrinsic spin* of the fragments. For equal mass nuclei we obtain $\Delta\ell = 2/7\ \ell_i$, and the fraction varies depending on the mass asymmetry, as shown below:

$\alpha = \frac{M_1}{M_1+M_2}$	$\frac{\mathcal{J}_S}{\mathcal{J}_{NC}}$	$\frac{\Delta\ell}{\ell_i}$
0.1	2.87	0.65
0.2	1.83	0.45
0.3	1.54	0.35
0.4	1.43	0.30
0.5	1.40 = 7/5	0.29 = 2/7

In the case of *rolling* friction, however, the friction $\Delta\ell/\ell_i = 2/7$ *independent of the masses of the two nuclei.*[298]

For certain cases, it is possible to show that the nuclei must have reached the sticking configuration from an analysis[301,302] of the final channel kinetic energies. The total kinetic energy of a rotating system at scission is given by:

$$E_f = V_c(R) + V_N(R) + \frac{L_f(L_f+1)\hbar^2}{2\mu R^2} \qquad 3.33$$

In classical friction models it is usual to rewrite the last term as $f^2\, L_i(L_i+1)\hbar^2/\, 2\mu R^2$, where f is a numerical factor depending on the relevant type of friction. For sticking $f = \mu R^2/(\mu R^2 + \mathcal{J}_1 + \mathcal{J}_2)$, and the value of f often leads[303] to the experimental E_f values, using a value of $R \approx R_{crit}$ as discussed in Lecture 2.

A better test is to measure $\Delta\ell$ from the γ-ray multiplicity associated with different fragments arising from the decay of the complex.[304-306] As discussed in Lecture 2 it is reasonable to assume that the intrinsic angular momentum is just twice the

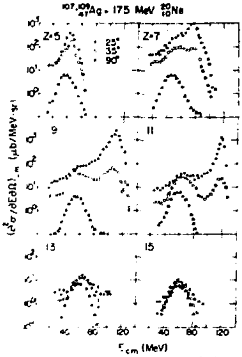

Figure 3.20(a)

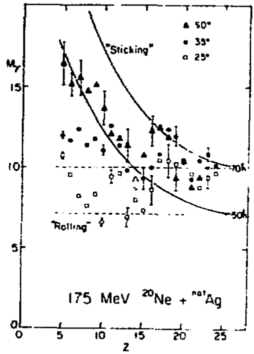

Figure 3.20(b)

multiplicity (assuming that the angular momentum is carried off mainly by the E2 yrast cascade). An example is the ^{20}Ne + Ag system at 175 MeV for which energy spectra are shown in Fig. 3.20(a) at three different angles. We see that in proceeding to more backward angles the quasi-elastic component disappears and the deeply-inelastic dominates, just as in Fig. 3.3. The multiplicities as a function of the Z of the detected fragments are shown in Fig. 3.20(b) for the deeply-inelastic component. For comparison the predicted values for the cases of rolling and sticking are drawn for two values of entrance channel angular momenta (50ħ and 70ħ). The value 70ħ is expected from the sum of the known evaporation residue cross section of 900 mb (corresponding to ℓ_{crit} = 50ħ) and the deeply-inelastic cross section of 400 mb, using our customary formulae. (The line for 50ħ corresponds to the limit for compound nuclear formation.) Then the rolling limit is given by

$$\Delta\ell = \frac{2}{7}\,\ell_i = 20\hbar \doteq 2M_\gamma \qquad 3.34$$

At 90°, where the rotating dinuclear complex has remained in contact for a long time, the sticking limit appears to be reached, with ℓ_i between 50 and 70ħ. At more forward angles the fragments appear to be still rolling on each other. These data furnish strong evidence that the intermediate complex approaches rigid rotation in a time comparable to the rotation period.

A similar experiment has been conducted[307] on the much heavier systems ^{86}Kr+^{165}Ho and ^{86}Kr+^{197}Au. (See Fig. 3.21). On the left hand side (quasi-elastic transfer) the multiplicities reflect simple transfer reactions where the angular momentum is transferred by particles without the formation of the dinuclear complex.

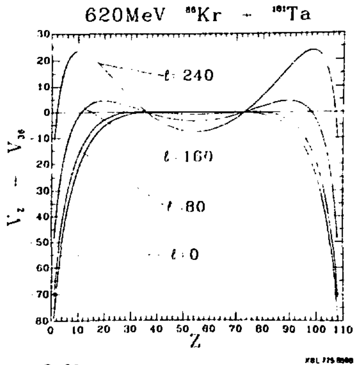

Figure 3.21

In that case we expect $\Delta\ell \approx \Delta M/M\ \ell_i$ where ΔM is the transferred mass and M is the incident mass. This formula leads to the characteristic V-shape in the figure. In contrast to our above example, the deep-inelastic components seem to be closer to the rolling limit (calculated as 2/7 $\langle \ell \rangle$, with $\langle \ell \rangle$ taken to be 2/3 ℓ_{MAX}, i.e, a triangular ℓ-distribution). This result is paradoxical since the energy is completely relaxed. The plausible escape from the dilemma is to assume that the low Z fragments are preferentially populated by low ℓ-waves. This explanation is supported by inspection of the curves of potential energy versus the Z of the fragment for a similar system in Fig. 3.22. At the Z of entrance channel (where the potential is scaled to be zero), the potential slopes towards symmetry for small angular momentum, becoming progressively steeper for higher ℓ. Therefore only the lowest ℓ-waves contribute to the

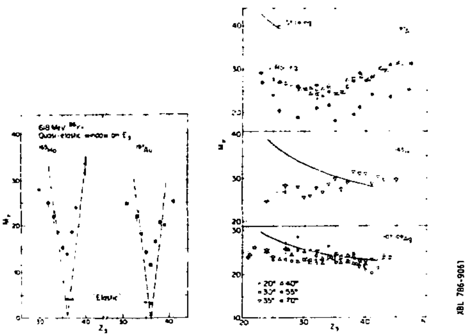

Figure 3.22

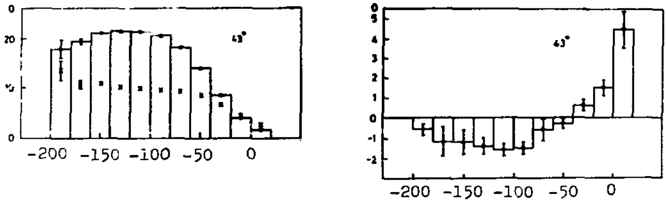

Q-Value MeV

XBL 786-9063

Figure 3.23

population of fragments much lighter than the projectile, a so-called "fractionation of the angular momentum distribution."

Clearly a better test of the theories will come from measuring higher order quantities in the experiments. For example, a recent experiment[308] with ^{86}Kr on ^{144}Sm at 490 MeV, in addition to measuring the mean multiplicity $\langle M \rangle$ of γ-rays in coincidence with quasi- and deeply-inelastic scattering, also measured the distribution of multiplicity by using an array of γ-detectors (as we described in Lecture 2). Then quantities such as the standard deviation $\nu = (\langle M^2 \rangle - \langle M \rangle^2)^{\frac{1}{2}}$ and the skewness $\langle (M - \langle M \rangle)^3 \rangle / \nu^3$ are accessible, examples of which are plotted in Fig. 3.23. The **left** part shows $\langle M \rangle$ and ν as a function of reaction Q-value. The **right** part shows the skewness. For Q-values close to zero, the skewness is positive indicating a preponderance of low M events, with the reverse in the deeply inelastic region. On a sticking model is it not possible to get the correct values of $\langle M \rangle$, ν and the skewness simultaneously. Another piece of experimental fine tuning comes from measurement of γ-rays to discrete final states. These determine the degree of alignment of the final fragments, which can be compared with the predictions of the sticking model.[309]

Another classic experiment has capitalized on the fission decay mode (rather than γ-decay) which is dominant in heavy systems. The experimental arrangement[310] in which ^{209}Bi was bombarded with 610 MeV ^{86}Kr ions is shown in Fig. 3.24(a). The angular correlation of one of the fission fragments, in coincidence with a projectile-like fragment, was measured both in-plane and out-of-plane. Classical arguments tell us that the fission fragments should be most intense in the plane, if the target-like fragment has a large angular momentum perpendicular to the reaction plane. The out-of-plane correlation for the fission fragments depends on the quantum number K, the projection of the total angular momentum on the symmetry axis of the fissioning nucleus. Then,

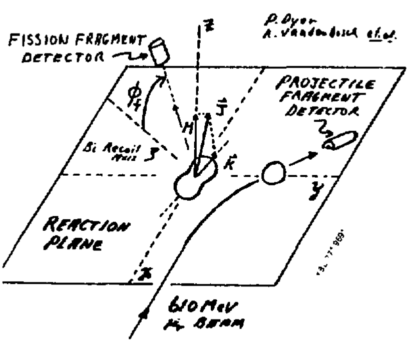

Figure 3.24(a)

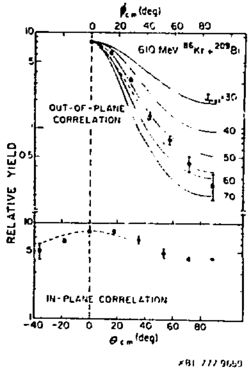

Figure 3.24(b)

$$\text{Yield} \propto \sum_{JMK} P(J)\ P(M)\ P(K)\ W^J_{MK}(\phi) \qquad 3.25$$

where

$$W^J_{MK}(\phi) \propto (2J+1)\left|d^J_{MK}(\phi)\right|^2 \qquad 3.26$$

The distributions P(K), P(M), and P(J) represent the probability for finding the system with these quantum numbers. P(K) can be determined from independent fission experiments. As a first estimate we can also assume complete alignment, so P(M) = P(J) with M=J. To determine P(J), the probability that a target-like fragment has angular momentum J, is the goal of the experiment. Assuming that the amount of angular momentum transferred, J, is proportional to the initial orbital momentum ℓ,

$$P(J) \propto (2J+1)$$

(because the partial deeply-inelastic cross section $\sigma_{DI}(\ell) \propto (2\ell+1)$). The distribution has an upper limit J_{max} to be determined.

The results are shown in Fig. 3.24(b) and indicate that $J_{max} = 58\hbar$, from a simultaneous fit to the in-plane and out-of-plane correlations. (Note that a recent study of sequential fission in a similar reaction attributes the out-of-plane distribution to the deeply-inelastic process itself by the excitation of collective bending oscillations.[311]) For the $^{86}Kr+^{209}Bi$ system, the *fraction* of the initial orbital angular momentum transferred is 0.29 ℓ_i for sticking. The value of ℓ_i in this reaction is 235ħ and therefore the measured value of J = 58ħ is close to the sticking limit of 68ħ.

This experiment is a refinement on the previously described γ-ray experiment, because in principle it could determine *the angular momentum associated with one of the fragments*. Now the angular momentum is divided between the fragments as follows:[298]

$$\text{For sticking:} \left(\frac{J_1}{J_2}\right) = \left(\frac{M_1}{M_2}\right)^{5/3} \tag{3.37}$$

$$\text{For rolling:} \left(\frac{J_1}{J_2}\right) = \left(\frac{M_1}{M_2}\right)^{1/3} \tag{3.38}$$

As the asymmetry becomes larger, this becomes a highly sensitive method for distinguishing between rolling and sticking.

The separation of γ-ray multiplicities between light and heavy fragments is possible in principle by measuring[312] the energy as well as the multiplicity. Then we can write:

$$\begin{aligned} \langle M_\gamma\rangle_H \langle E_\gamma\rangle_H + \langle M_\gamma\rangle_L \langle E_\gamma\rangle_L &= \langle M_\gamma\rangle\langle E_\gamma\rangle \\ \langle M_\gamma\rangle_H \langle M_\gamma\rangle_L &= \langle M_\gamma\rangle \end{aligned} \tag{3.39}$$

and extract $\langle M_\gamma\rangle_H$ and $\langle M_\gamma\rangle_L$. The results for 237 MeV $^{40}Ar + {}^{89}Y$ give a ratio of $\langle M_\gamma\rangle_L/\langle M_\gamma\rangle_H$ in the region of 12 for fragments far removed from the initial channel. By the above equation this result implies an approach to the sticking limit.

Ultimately it will be necessary to make a full solution of the dynamical equations of motion with conservative and dissipative forces for comparison with the experiments.[298,313] For the Kr + B_i case discussed above these equations have been solved using a tangential friction component which was weak compared to the radial component[314] and resulted in a total angular momentum transfer to both fragments of only 38ħ, considerably below the experimental value.

3.5 The Limits of Space and Time

We have seen that in deeply-inelastic scattering, macroscopic concepts such as viscosity and friction, are of great current interest. On the other hand, in conventional nuclear physics, the statistical model, which assumes thermodynamical equilibrium, has been generalized to include pre-equilibrium behavior.[315] Since energy dissipation includes not only viscosity but also heat conductivity, it may be possible to make a link between the two approaches.[316,317] A new generation of experiments is aimed at studying the formation of "hot-spots" in nuclear matter.[318] This concept is very old. To quote from an historical paper,[318] "If a nuclear particle of energy E, comparable with the nuclear interaction energy, strikes a nucleus, it will lose practically all its energy in the 'surface layer' of the nucleus. This process will cause intense local heating of the part of the nucleus struck. The 'heat' will then gradually spread over the whole nucleus." A calculation[319] of the heat conductivity, specific heat etc. of nuclear matter from a Fermi gas model was already completed in 1948.

First consider some typical time scales of deeply-inelastic reactions.[197] For the rotational motion, we have an angular velocity ω and an angle of rotation θ through which the fragments remain in contact. Therefore:

$$\tau_{\mathrm{int}} \approx \theta/\omega \qquad (3.40)$$

Values of E_{rot}, ℓ and $\mathcal{J}$ can be estimated, so we can use

$$\omega = \frac{2E_{rot}}{\hbar\ell} \qquad \text{or} \qquad \omega = \frac{\hbar\ell}{\mathcal{J}} \qquad (3.41)$$

to obtain ω. For example, a reasonable estimate of ℓ is $5/7\,\ell_i$, corresponding to rolling fragments, and $E_{rot} = E_{CM} - E_{Coul} + Q$. For the reaction ^{40}Ar + ^{232}Th at 379 MeV (Fig. 3.3) $E_{rot} \approx 150$ MeV, $\ell \approx 150$ (see discussion of Equ. 3.15) so $\omega \approx 3 \times 10^{21}$ sec^{-1} and $\tau \approx 3 \times 10^{-22}$ sec for a typical rotation angle of 1 radian.

We can also estimate the time it takes an equilibrated excited nucleus to emit a particle. An empirical fit to the measured widths of compound nuclei for A = 20-100 yields:[111]

$$\Gamma(\mathrm{MeV}) = 14 \exp(-4.69\sqrt{A/E^*}\,) \qquad (3.42)$$

Relating the temperature T to the excitation energy by $E = aT^2$, where $a \approx A/8$, we have

$$\tau_{\mathrm{particle}} \approx 0.5 \exp(13/T) \qquad (3.43)$$

where T is in MeV and τ in units of 10^{-22} sec. An excitation energy of 3.25 MeV/A yields a temperature of 5 MeV and a lifetime of 7×10^{-22} sec. If local temperatures of this magnitude should be produced in heavy-ion collisions, then the lifetime for particle emission is so short that the rotating dinuclear complex will emit particles before it scissions. We say *local* temperatures because *total* center of mass energies in deeply-inelastic experiments are < 10 MeV per *projectile* nucleon, and therefore the achievement of, say, 3 MeV/nucleon in some region requires a concentration of energy into a "hot-spot."[316-318]

Delving slightly deeper we can write the relaxation time for dissipating the initial energy deposition as:[316]

$$\tau_R = \frac{R^2}{\chi} = \frac{R^2}{v_F\Lambda}\ ,\ \chi = \frac{K}{\rho c_p}\ . \qquad (3.44)$$

Here v_F is the Fermi velocity, Λ is the mean free path for nucleon-nucleon scattering, K is the thermal conductivity, ρ is the density and c_p the specific heat of nuclear matter. Expressions for K and c_p can be derived from the Fermi gas model.[319,320] Thus,

$$K = \frac{7}{48\pi\sqrt{2}}\ \frac{\varepsilon_F^{3/2}}{m^{1/2}\,TQ}\ ,\ c_p = \tfrac{1}{2}\,\frac{\pi^2 T}{\varepsilon_F} \qquad (3.45)$$

where ε_F is the Fermi energy, T is the temperature and Q is the effective nucleon-nucleon cross section. ($\approx$ 27 mb). For a temperature of $\approx$ 1 MeV, τ_R is 4×10^{-22} sec. From the above equations, τ_R varies as T^2 (essentially because the mean free path decreases as more nucleons are excited above the Fermi level), and, at high enough temperatures, becomes longer than the time for particle emission. These trends are illustrated in Fig. 3.25 from an old calculation[321] (left hand side) and a recent calculation.[322] In both calculations as the incident energy (temperature) increases we reach a point where the compound nuclear lifetime is less than the

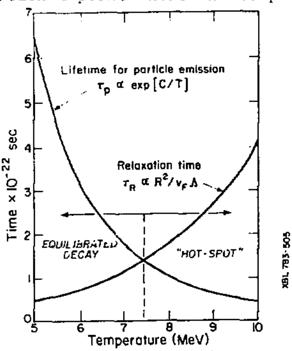

Figure 3.25(a)

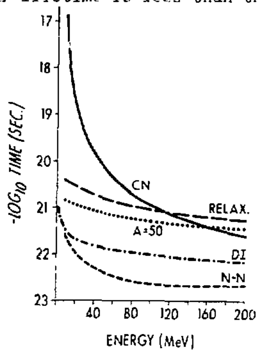

Figure 3.25(b)

relaxation time, just the condition for the formation of a hot-spot. (Also shown on the right are the passing times for two A = 50 nuclei, the nucleon-nucleon collision time.) The critical temperature appears to be around 8 MeV[323]. (We shall return to this temperature in Lecture 4.)

Several coincidence experiments have recently been performed, with the general philosophy directed at observing hot-spots.[324] All these experiments have studied the angular correlation of light particles (e.g., alphas) in coincidence with the projectile-like heavy fragment emitted in quasi- or deeply-inelastic scattering at a fixed angle. A typical example[325] is shown in Fig. 3.26 for reactions of ^{16}O + ^{208}Pb at 140 MeV and 315 MeV. For a variety of projectile fragments, the correlations are very narrow and peak roughly in the direction of the fragment (marked with an arrow) or between this direction and the beam axis. Note that the channel attainable by *pure* projectile fragmentation ($^{12}C + \alpha$) has a double peak, as expected, but the other channels (e.g. $^{14}N + \alpha$) give very similar overall distributions. The fact that all these patterns are reminiscent of the decay of an excited projectile-like fragment is also confirmed by a kinematic contour plot. This is shown in Fig. 3.27 for a similar reaction,[326] ^{14}N + ^{93}Nb at 90 MeV leading to ^{10}B and α fragments. The two islands are consistent with decay of a prefragment $^{14}N^*$ at an excitation of ≈ 1 MeV (denoted by the dotted kinematic constraint) traveling with a kinetic energy of ≈ 55 MeV (dashed lines).

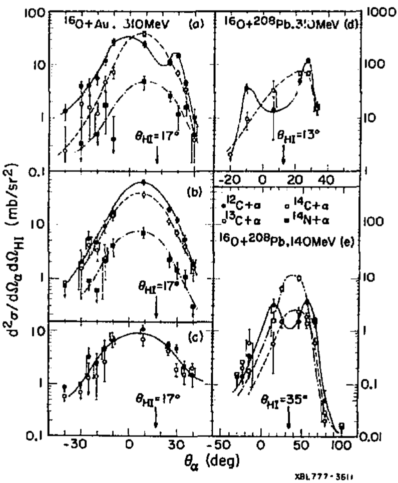

Figure 3.26

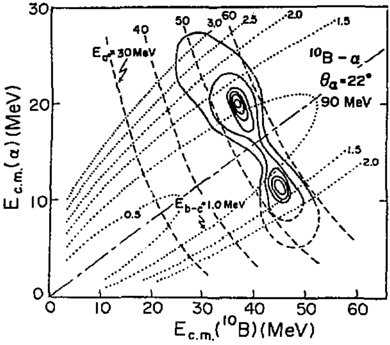

Figure 3.27

A possible interpretation of similar correlations of α-particles observed in reactions of $^{32}S + ^{197}Au$ at 12 MeV/nucleon[327] is given in Fig. 3.28. The ^{32}S moves along the Rutherford trajectory up to the distance of closest approach. Then it emits an alpha from the surface in any possible direction. The subsequent motion of the α, ^{28}Si and ^{197}Au nuclei in the Coulomb field is calculated numerically, generating two peaks in the correlation. Only the left hand peak appears in the data, which is associated with the region of the projectile between the projectile and target (i.e. a localized region). The first experiment[328] to reveal such a phenomenon (actually emitted from a "hot-spot" on the target) was the reaction $^{16}O + ^{58}Ni$ at 92 MeV. The confusing effects of projectile break-ups were eliminated by searching for α-particles in coincidence with ^{16}O scattering. The rather detailed analysis[329] of this

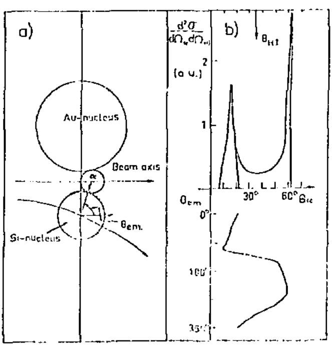

Figure 3.28

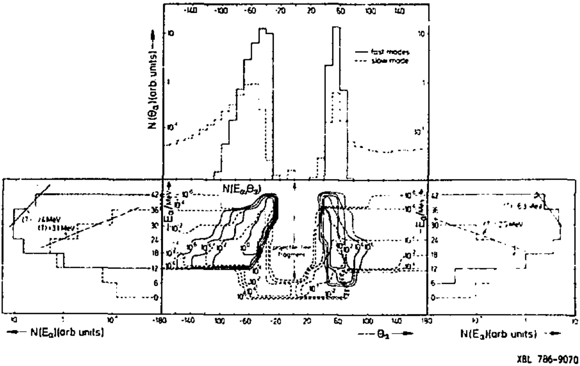

Figure 3.29

experiment assumes that a hot-spot is created on the surface of the target, the α-emission from which has a high temperature component emitted outwards from the pole, and a low temperature component from the diffusion of the α-particles through the nuclear matter in the opposite direction. The final solution is complicated by Coulomb and nuclear deflections and by angular momentum, which makes the hot spot rotate. Nevertheless, some idea of the results is conveyed in Fig. 3.29. The top part shows the α-correlation measured from an origin in the direction of the projectile. Both the fast and the slow modes lead to the narrow angular correlations, characteristic of all the experiments we have been discussing. The bottom middle section displays contour plots of the cross section in an Eα-θα diagram, the projections of which onto the Eα axes (left and right) show the expected α-particle spectra. The high temperature component (≈ 7 MeV) is close to the temperatures required for the observation of a hot-spot (see Fig. 3.25) whereas the low temperatures are characteristic of greater equilibration. The experiment[323] yielded temperatures of 3-4 MeV in the forward direction. Using the expressions $E_x = aT^2$ and the value of E_x = 28 MeV extracted from the experiment, the value of $a = N/8$ given $N \approx 18$ particles. For a fully equilibrated system $N \approx 70$ and the temperature would have been only 1.8 MeV. Such experiments can lead to a determination of the thermal conductivity and specific heat of nuclear matter, and are an alternative to preequilibrium theories.[316,317]

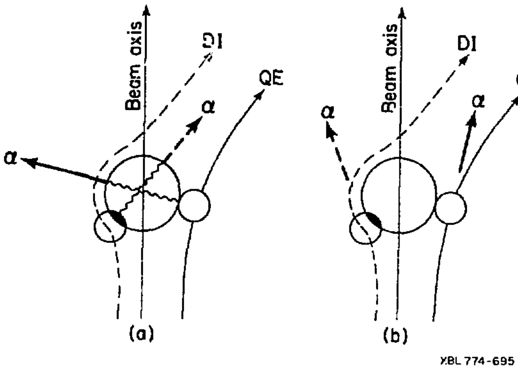

Figure 3.30

There are several other experiments on the production of fast non-equilibrium light particles,[227,228,330-332] with interpretations ranging over emission from the neck between the colliding nuclei[330] (like ternary fission and maybe even like a hot-spot) to backward splashes of α particles accompanying fusion.[228] The fun is just beginning. The theoretical possibilities are also diverse. A possible mechanism[333] for the production of fast, non-equilibrium α-particles is the strong radial friction damping force, which ejects a particle on the opposite side of the nucleus from where the projectile and target first make contact (see Fig. 3.30). This leads to a correlation with the α and the heavy fragment on the *same* side of the nucleus which would not be consistent with many of the above experiments. Another possibility is illustrated in part (b) of the figure,[325] which by similar arguments would attribute the α-production to strong *tangential* friction, certainly essential as we have seen to account for the results of γ-ray multiplicity and the fission fragment experiments. This picture can explain how in Fig. 3.26 alpha particles are observed in coincidence with heavy fragments that could not arise from simple projectile fragmentation, but which nevertheless bore close resemblances. This picture has also been said to represent a "sparking process,"[334] and is consistent with our discussion of "hot-spots" in this section, i.e., a zone of slightly higher complexity and concentration than occurs in simple projectile excitation. We note in Fig. 3.26, however, that at the higher energy the relative importance of these more complicated channels diminishes and the pure fragmentation channel becomes dominant. This simplification sets our path towards Asymptotia, the subject of the last lecture.

4. ASYMPTOTIA

In this lecture we leave behind the familiar territory of *Microscopia*, and even the still recognizable landmarks of *Macroscopia*, to venture into the New World of *Asymptotia*. Before setting out it is just as well to have a navigation chart,[335] which appears in Fig. 4.1. The abscissa is the projectile energy in MeV/nucleon and the ordinate is the projectile mass plotted as $A^{1/3}$. The shaded bands define regions of fundamental parameters such that when we cross a band, we can be confident that the underlying physics will change. The three characteristic center of mass energies of 20 MeV, 140 MeV and 930 MeV are estimates of where the subsonic, mesonic and relativistic domains merge. Macroscopic phenomena come into prominence when $A^{1/3} \gg 1$. The band at $Z \approx \frac{1}{2}$ (170) is a reminder of the changes that may occur when (2Z× fine structure constant) becomes large compared to unity. Most of this space is unexplored apart from the two axes, the left-hand side with the low energy heavy-ion machines and the horizontal axes with high energy, hadron accelerators. Although some possibility for exploring the remaining space (where most of the crossing bands lie) has existed with Nature's own accelerators, the Cosmic radiation,[336,337] it is the development of high energy, heavy-ion accelerators, such as the Berkeley Bevalac, that has sharpened and focussed these studies. Combined with parallel developments on increasing the energy of existing Cyclotrons (at Berkeley and Texas A and M) up to 35 MeV/nucleon, it is now possible to trace the evolution of heavy-ion reaction mechanisms across some of the critical boundaries of Fig. 4.1. We begin with a discussion of this evolution in peripheral collisions, then deal with the more dramatic (possibly) central collisions and end with a few words on exotic phenomena.

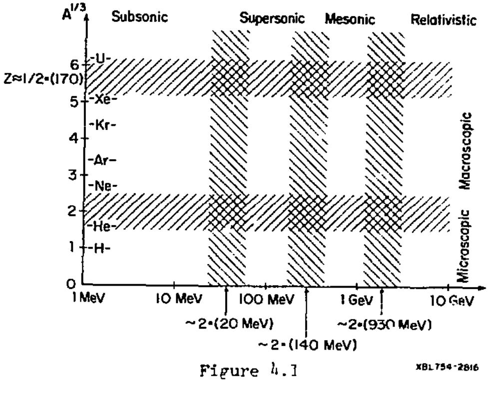

Figure 4.1

XBL754-2816

4.1 Evolution of Peripheral Collisions

In order to make a conceptual link with the last lecture, let us consider how deeply-inelastic scattering might evolve with energy.[338] Imagine two nuclei with radii R colliding with relative velocity u. The collective kinetic energy is

$$E \approx \left(\frac{4}{3}\pi R^3 \rho\right) u^2 \tag{4.1}$$

(We are dropping factors of order unity.) If the nuclei are in communication through a window of area πa^2 (as discussed in Lecture 3, equ. 3.21, etc.), we have

$$\frac{dE}{dt} \approx \tfrac{1}{4}\, \rho\, \bar{v}\, (\pi a^2)\, u^2 \tag{4.2}$$

where $\bar{v}$ is the average intrinsic nucleon speed. Therefore the characteristic damping or stopping time is of order:

$$t_{stop} \approx R^3\, \rho\, u^2/\rho\, \bar{v}\, a^2 \approx \left(\frac{R}{a}\right)^2 \left(\frac{R}{\bar{v}}\right) \tag{4.3}$$

We compare this time with the collision time, $t_{coll} = R/u$ to give:

$$\frac{t_{stop}}{t_{coll}} \approx \left(\frac{R}{a}\right)^2 \left(\frac{u}{\bar{v}}\right)^2 \left(\frac{R}{a}\right)^2 \sqrt{\frac{\text{Energy/nucleon}}{\text{Fermi Energy}}} \tag{4.4}$$

Therefore if "a" is not too small, as the incident energy approaches the Fermi energy, complete damping plays less of a role. We must then ask the question, what process takes over the large deeply-inelastic cross section?

It appears that multibody fragmentation phenomena replace the essentially two-body processes of deeply-inelastic scattering.[339] Below 10 MeV/nucleon, the collision time is longer than the transit time of a nucleon at the Fermi level; consequently the whole nucleus can respond coherently to the collision, and the dominant phenomena are characteristic of the mean field.[340] At relativistic energies of GeV/nucleon, on the other hand, the reaction processes are dominated by independent collisions of individual nucleons.[341] The transition region might be set by requiring the complete disjunction of the two colliding nuclei in momentum space, i.e., at a few tens of MeV/nucleon. This transition, which could be labelled[323] "from nuclei to nucleons," has been observed in peripheral collisions.

The approach is to measure the production cross sections and energy spectra of projectile-like fragments from ^{16}O induced

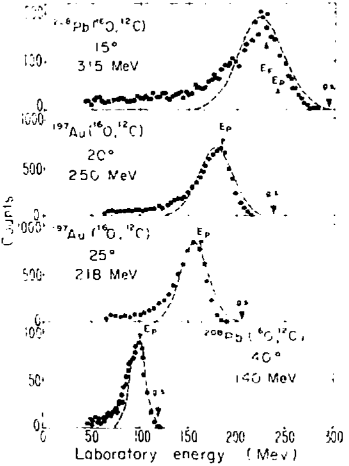

Figure 4.2

reactions on targets such at Pb, Au as a function of incident energy.[342,343] Some typical spectra for outgoing ^{12}C products at incident energies of 140, 218, 250 and 315 MeV are shown[344] in Fig. 4.2. The spectra all have a characteristic Gaussian form, peaked at an energy (labelled Ep) corresponding to the fragment travelling with a velocity close to that of the incident beam. At low energies, if two-body deeply-inelastic scattering is the relevant mechanism, this behavior implies a high excitation of the residual fragments (compare the energy, labelled g.s. in Fig. 4.2, associated with the production of the nuclei in the ground states). The continuum could also correspond to transfer reactions to a high density of states[345,346] in the continuum, with an optimum Q-value.[347]

The continuum is also characteristic of multibody fragmentation at high energies. An example of similar spectra at 2.1 GeV/nucleon is shown[348] in Fig. 4.3. Here the spectrum is plotted in the projectile rest frame, so that a fragment emerging with beam velocity would correspond to $P_{11} = 0$, where P_{11} is the longitudinal momentum in the projectile frame. In fact, just as in Fig. 4.2, the Gaussian shaped distributions are shifted slightly below this point. Both at 2.1 GeV/A and 20 MeV/A this shift (ΔP_{11}) is well accounted for by the separation energy of the projectile into the observed fragment together with residual nucleons and alpha particles[349,350] (e.g. the arrow labelled E_F in the top part of Fig. 4.2). In Fig. 4.2 we observe that the widths of the spectra increase rapidly with energy, which is a manifestation of the transition in the nature

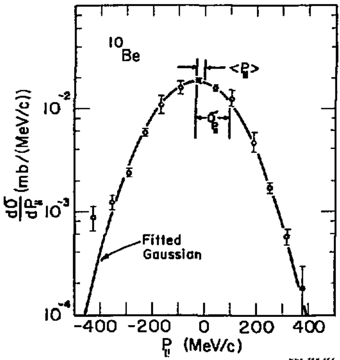

Figure 4.3

of the reaction mechanism.

First we use the concept of temperature to find systematic trends in the data. At low energies (< 10 MeV/A) the production cross sections of isotopes, in reactions of the type reported here, have an exponential dependence,[351,352] $\sigma \propto \exp(Qgg/T)$, where Qgg is the two-body, transfer ground state Q-value. A good example is shown in Fig. 4.4 for the system ^{16}O + ^{232}Th (similar to ^{16}O + Au, Pb), in which the cross sections were obtained by integrating spectra similar to Fig. 4.2. The exponential dependence on Qgg over *five orders of magnitude* would not be expected from a simple direct reaction model,[352] relating the cross section to the Q-value at the *peak* of the distribution, which might be 50 to 100 MeV more negative. The systematics do however have a natural explanation in terms of a

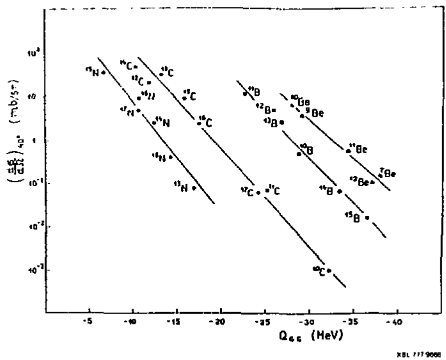

Figure 4.4

rotating dinuclear system undergoing partial statistical equlibrium at temperature T.[351,352] In a statistical reaction, the cross section is given by:[352]

$$\sigma \propto f_f(E^*) \propto \exp \frac{E^*}{T} \tag{4.5}$$

proportional to the level density of states at excitation E*, which can be written E* = Qgg-Q, and the Q-value is made up of the changes of Coulomb energy, rotational energy and other excitation processes. Therefore,

$$\sigma \propto \exp \frac{Qgg-\Delta Vc}{T} \tag{4.6}$$

where we have included only the Coulomb term in Q, since some of the others are not strongly coupled to the degrees of freedom participating in the equilibration.[352]

The temperatures derived from this approach for a variety of data (including those of Fig. 4.2, and of the extensive analysis of ^{16}O, ^{15}N + ^{232}Th reactions[351]) are shown in Fig. 4.5 by the filled circles, plotted as a function of the incident energy above the barrier (top scale). The variation initially follows the trend of the Fermi gas equation of state, $E^* \approx (E_c-V) = aT^2$, where E_c is the center of mass energy, V the Coulomb barrier in the incident channel, and "a" is the level density parameter, equal[354] to A/8, with A the mass number of the intermediate complex. Hence T is proportional to $\sqrt{E_c-V}$, the variable used on the bottom scale.

At relativistic energies the concept of temperature has also been useful in explaining isotope production cross sections, where

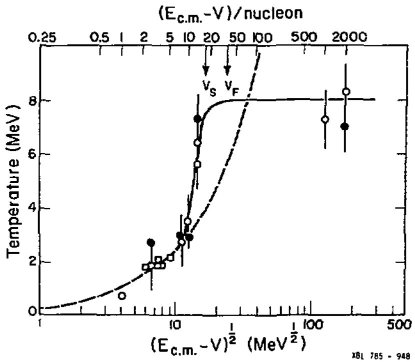

Figure 4.5

the "emitter" is the projectile rather than the dinuclear complex.[342,355-357] Then $\sigma \propto \exp(Q_F/T)$, with Q_F equal to the fragmentation Q-value, and T is the projectile temperature. This approach has been applied to the data in Fig. 4.5 at 315 MeV (≈20 MeV/A)[343] and at 2.1 GeV/A;[348] the values of T are also displayed in Fig. 4.5. Following the initial trend of the Fermi gas equation, a rapid rise sets in between 10 and 20 MeV/A, after which the temperature appears to saturate at approximately 8 MeV. Above 15 MeV/A, where the curve departs from the prediction of the Fermi gas for heating the entire complex, only a part of the total system can be heated (compare our discussion of hot-spots at the end of the last Lecture). The saturation at 8 MeV could be interpreted by assuming that A' (<<A) nucleons participate and carry less than BA' of excitation energy, where B is the binding energy of a nucleon (≈8 MeV), for the system to survive to emit a complex fragment. If this subsystem is excited like a Fermi gas, the result T ≈ 8 MeV follows immediately from the equation $BA' = A'/8T^2$. Since higher temperatures would result in a disintegration of the fragment,[339] it is natural to refer to this temperature as the "boiling point of nuclear matter" (It is interesting to make an analogy with Fig. 1.4, where a limiting temperature is also observed for hadronic matter; this has also been referred to as a boiling point of hadronic matter.[358]

Although temperature is a useful concept for organizing the data, and for understating the limiting behavior in the high energy region, an alternative interpretation comes from the abrasion model[359,360] in which the primary fragments emerge by the sudden shearing of the projectile without prior excitation. The dependence $\sigma \propto (Q_F/T)$ can also be derived analytically with this model.[344] The basic idea of this model is illustrated in Fig. 4.6 (top part).[361]

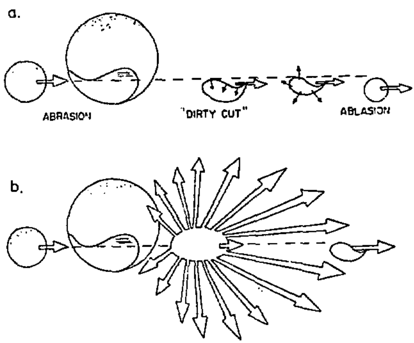

Figure 4.6

XBL 777-9683

The incident projectile in the region of overlap with the target has a part sliced out.[362] The cross section for this process can be calculated using Glauber theory[363] or from geometrical considerations. The cut is not clean but creates a hot region which causes the remaining fragments to be highly excited, so that they proceed to evaporate additional particles (ablation). In the Glauber model at high energies the nucleus-nucleus cross section for an event in which n projectile nucleons are scattered out of the projectile A is:

$$\sigma_n = \binom{A}{n} \int d^2\underline{b}\ (1-P(b))^n\ P(b)^{A-n} \qquad 4.7$$

where

$$P(b) = \int dz\ d^2\underline{s}\ \rho_A(s-bz)\ \exp[-A_T\sigma_{NN}\int dz'\ \rho_T(s,z')] \qquad 4.8$$

Here (1-P(b)) is the probability of finding a projectile nucleon in the overlap zone when b is the impact parameter. Equation 4.7 is then the cross section for n projectile nucleons to be in the overlap and (A-n) outside. It turns out that σ_n changes very little between 20 MeV/A and 2 GeV/A in spite of a large change in σ_{NN}. However, at high energies the momentum transfer is sufficient to knock nucleons out, but at low energies they appear to stay in the prefragment and deposit their energy. The subsequent fate of the projectile fragment (the ablation stage) is rather different in the two cases. This model[364] appears to account both for the isotope differences and the element similarities observed in O^{16} induced reactions at 20 MeV/A and 2.1 GeV/A.

For the primary distribution of fragments, eq. 4.7, 4.8 lead to a distribution in mass and mass and isospin, we use the formulation of the abrasion model in Ref. 365 :

$$\sigma \propto \exp -\left[\frac{(a-a_o)^2}{2\sigma_a^2} - \frac{(t_3-t_{30})^2}{2\sigma_{t_3}^2}\right] \qquad 4.9$$

where a = N+Z, the number of nucleons abraded, $t_3 = (N-Z)/2$ and σ_a, σ_{t_3} are the dispersions around the mean values a_0, t_{30}. Transforming to the variables N,Z yields the distribution of isotopes about the mean:

$$\sigma \propto \exp\left[-(N-N_o)^2\left(\frac{1}{2\sigma_a^2} + \frac{1}{8\sigma_{t_3}^2}\right)\right] = \exp\left[-\frac{(N-N_o)^2}{\alpha}\right]. \qquad 4.10$$

Values of σ_a, σ_{t_3} are derived from a model with correlations built into the nuclear ground state, viz. $\sigma_{t_3} \approx 0.24\ A^{1/3}$, $\sigma_a \approx 4.9\ \sigma_{t_3}$ (see later).

In the production of a series of isotopes the changes in Q_F are determined primarily by the N-dependent terms in the liquid drop mass formula. For a fragment of mass A_F this term can be written;

$$\frac{a_s(A_F-2N)^2}{A_F} - \frac{a_{ss}(A_F-2N)^2}{A_F^{4/3}} \qquad 4.11$$

where a_s and a_{ss} are the symmetry and surface symmetry coefficients respectively. It is then simple to derive a quadratic dependence of Q_F on $(N-N_o)^2$, viz.

$$Q_F = 4\left(\frac{a_s}{A} - \frac{a_{ss}}{A^{4/3}}\right)(N-N_o)^2 = \beta(N-N_o)^2 \qquad 4.12$$

From Eqs. 4.10 and 4.12 we get,

$$\sigma \propto \exp\left(\frac{Q_F}{\alpha\beta}\right) \qquad 4.13$$

which is equivalent to the result of the thermal model, with T replaced by $\alpha\beta$. By inserting the values[365] of σ_a, σ_{t_3} and of the mass formula coefficients,[366] we deduce that $T = 9$MeV[a] (or 5 MeV with values of σ neglecting[365] correlations). This derivation of isotope distributions ignores the subsequent redistribution by nucleon capture and evaporation,[364] but the value of 9 MeV is close to the required saturation value of 8 MeV in Fig. 4.5. This parameter in the exponential dependence of σ on Q_F is, however, identified with *the onset of the fast abrasion mechanism,* rather than with the saturation of nuclear temperature in the slower, equilibrating process.

In the saturation region above 20 MeV/nucleon, the abrasion model also accounts consistently for the momentum distribution of fragments in the projectile rest frame,[356]

$$\frac{d^3\sigma}{dp^3} \approx \exp\left[-\frac{(p-p_o)^2}{2\sigma^2}\right] \qquad 4.14$$

where p_o is the momentum corresponding to the peak of the distribution, of width:

$$\sigma^2 = \sigma_o^2 \frac{F(A - F)}{(A - 1)} \qquad 4.15$$

F, A are the masses of the observed fragment and the projectile respectively. This value of σ^2 is just related to the mean square momentum of F nucleons in the projectile suddenly going off as a single fragment. Not surprisingly, therefore, it is also closely related to the Fermi momentum by $p_F = \sigma_o\sqrt{5}$ which has been measured[367] as 235 MeV/c for ^{16}O). The analysis of the heavy-ion spectra yields $\sigma_o \approx 86$ MeV/c or $p_F = 192$ MeV/c. The Gaussian distribution shown in Fig. 4.3 is calculated with the above equations. For the energy distributions in the laboratory frame at angle θ, transformation of Eq. 4.14 yields:[343]

$$\frac{d^2\sigma}{dEd\Omega} \propto \sqrt{2A_F E} \ \exp\left[-\frac{A_F}{\sigma^2}\ (E-2aE^{1/2}\cos\theta + a^2)\right] \qquad 4.16$$

where $a^2 = 1/2\ M_F v_p^2$, v_p is the velocity corresponding to the peak of the energy distribution. This formula is used to generate the theoretical curve in Fig. 4.2 for the top set of data at 20 MeV/A, again using $\sigma_o \approx 86$ MeV/c in the expression for σ^2.

The energy distribution in Eq. 4.16 is also expected from a statistical model of fragment emission.[356] Therefore, the formula can equally well be applied to the lower energy spectra in Fig. 4.2, where we have already shown that equilibration processes at temperature T are relevant. By conservation of energy and momentum, T and σ_o are related[356] by

$$\sigma_o^2 = T\ m\ \frac{A_P - 1}{A_P} \quad ,$$

where m is the nucleon mass in MeV. (For $\sigma_o = 86$ MeV/c, $T \approx 8$ MeV, consistent with the two interpretations of the isotope distributions in the high energy region). The values of T required to fit the data at all energies are shown in Fig. 4.2 by the open circles. Also included are data for oxygen on nickel at 315 MeV and on tantalum[368] at 96 MeV. Although only results for ^{12}C fragments are presented, similar trends were observed in the energy spectra of other particles.[343] At low energies (<10 MeV/nucleon) the temperatures extracted from the momentum and isotope distributions are in agreement, supporting the temperature model. At high energies (>20 MeV/nucleon) the saturation of the widths of the momentum and isotope distributions at 8 MeV is consistent with a fast abrasion mechanism, although the alternative interpretation of a localized thermal excitation is not excluded.

If we adopt the abrasion model for the description of the high energy data, then the sudden transition from equilibration to fragmentation must contain information on characteristic properties of nuclear matter, such as the relaxation time for spreading the localized deposition of energy, or "hot-spot",[316,317] over the nucleus. The initial excitation may be in the form of uncorrelated particle-hole excitations, in which case this relaxation time is related to the Fermi velocity. On the other hand, if the initial excitation is carried by coherent, collective compressional modes, then this time is related to the frequency of these modes, which in turn depends on the speed of sound in nuclear matter.[369] Recent experiments,[370] determining the frequency of the monopole mode, lead[371] to a value of the compressibility coefficient $K \approx 300$ MeV, and an implied velocity of sound $v_s = \sqrt{K/9m}$ of 0.19c (m is the nucleon rest mass). This velocity and the Fermi velocity in nuclear matter (equivalent to 36 MeV/nucleon) are marked in Fig. 4.2. Although it would be premature to specify which (if either) defines the change of mechanism without a detailed model, the velocity of sound is certainly close to the transition region.

A formal approach to the break-up of nuclear matter was given recently,[372] by writing for the stress, S:

$$S = P = \frac{\partial E}{\partial V} = \rho^2 \frac{\partial (E/A)}{\partial \rho} \qquad (4.17)$$

with

$$\frac{E}{A} = \frac{\hbar^2}{2m} k^2 + A\rho + B\rho^2 \qquad (4.18)$$

In this equation the three terms represent the kinetic energy and the effects of the ordinary and velocity dependent nucleon nucleon potentials. Then the stress becomes:

$$\frac{P}{\rho} = \frac{2}{5} \hbar^2 \frac{k_F^2}{2m} \left(\frac{\rho}{\rho_o} \right)^2 + A\rho + 3B\rho^3 \qquad (4.19)$$

from which information on the tensile strength of nuclear matter is obtained in the condition of maximum stress $dP/d\rho = 0$, which is equivalent to the classical condition of the sound velocity going to zero. In central collisions the energy per particle comes out at a few MeV/A. This approach, if extended to the type of peripheral collisions we have discussed in above, could be a fruitful way of studying continuum properties of nuclear matter.

The equivalence of two extreme models for the ^{16}O-induced reactions is an intriguing problem. One model assumes thermal equilibration whereas the other is a fast abrasion process from the nuclear ground state. The degeneracy might be removed by using heavier projectiles such as ^{40}Ar, with which the deeply-inelastic scattering processes at low energies are better developed (as we discussed in Lecture 3). A new series of experiments to study the isotope production cross sections as a function of energy has been initiated. An example of the first experiment[373] with 213 MeV/A Argon on Thorium and Carbon is shown in Fig. 4.7. The identification of isotopes was achieved by multiple ΔE-E identification in a 9 element detector telescope, and imposing a χ^2-criterion that the identification be similar in all detectors.[374] All isotopes up to Argon were resolved although this is difficult to see in the illustration.)

The momentum spectra for ^{16}C and ^{34}S are shown in Fig. 4.8. These are representative of all the isotopes are chosen as examples close to and far removed from the projectile. The theoretical curves come from Equ. 4.14 and 4.16, with values of $\sigma_0 \approx 90$ MeV/c (see Equ. 4.15). (The associated temperature is 8.9 MeV.) In the framework of Fig. 4.5 this result fits into the pattern of ^{16}O, and we take it as confirmatory evidence for the fast abrasion mechanism.

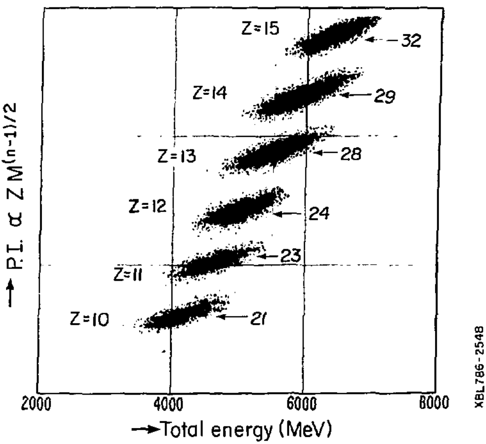

Figure 4.7

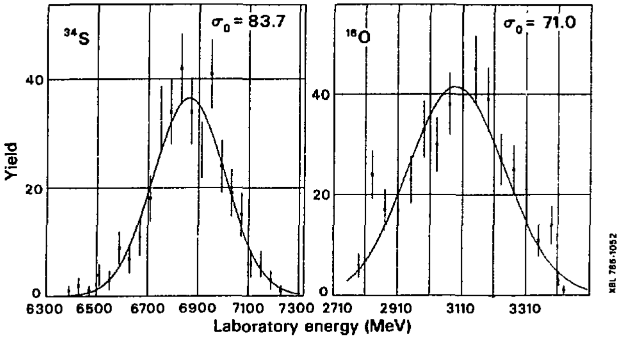

Figure 4.8

In the thermal equilibrium model we might conjecture that the temperature would have come out lower than for ^{16}O, as the initial localized deposition is cooled more rapidly by the larger thermal capacity of the heavy projectile.[337] The crucial test will come from the equivalent study of the *isotope* distributions, since the parameter $\alpha\beta$ in Equ. 4.13 *is* A-dependent, whereas the Fermi momentum parameter σ_o which characterizes the momentum distribution in the abrasion model is not.

Although the analytical comparison for the Argon reactions has not been completed, the preliminary results do indeed indicate that the "T" or "$\alpha\beta$" parameter is quite different from ^{16}O, although it appears[375] to *increase* to approximately 12 MeV, rather than decrease as predicted by the (oversimplified) analyses of Equ. 4.19-4.13. A value of 14 MeV in the expression $\sigma \propto \exp(QF/T)$ has been deduced in a similar experiment[376] with 250 MeV/A ^{12}C on Ca in which the *target* fragmentation yields were measured by γ-ray counting (this is *effectively the inverse experiment*). The predicted curve, using only the leading Q_F value of Q_{min} is shown in Fig. 4.9(a). The likely success of the abrasion-ablation approach is also encouraging from the predictions[377] for the magnesium isotope distribution[373] (hatched curve) in Fig. 4.9(b) compared to the data (solid points); the calculation reproduces the width of the distribution fairly well, although the peak is shifted from the experimental maximum.

The widths of the isotope distributions in the abrasion model is of considerable interest in view of recent attempts to account for them by building correlations into the nuclear ground state.[365,378] In the absence of correlations the abrasion model just calculates the dispersions (e.g., σ_a and σ_{t_3} in Equ. 4.9) in the number of protons and neutrons removed as equivalent to the relative number of ways of distributing neutrons and protons in an assembly of "a" nucleons

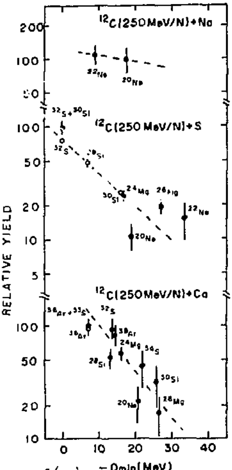

Figure 4.9(a)

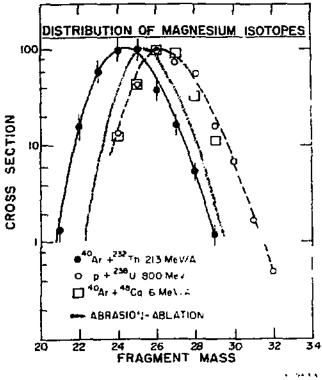

Figure 4.9(b)

(see also Equ. 4.7). Fig. 4.10 shows some representative primary product change distributions for ^{12}C + ^{238}U at 2.1 GeV/A.[378] (The data were acquired by the radiochemical method, as in Fig. 4.2.) An alternative model for the dispersions assumes that fluctuations in the number of swept-out protons (see Fig. 4.6) arise from zero-point vibrations of the giant dipole resonance, which is an out-of-phase vibration of protons and neutrons.[379] The predictions with (GDR) give a narrower width in better agreement with the experimental

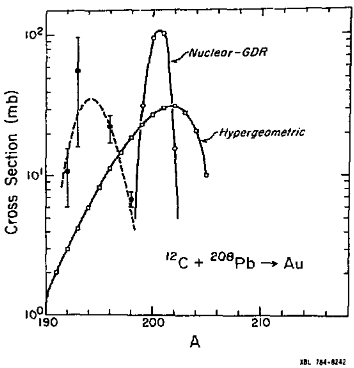

Figure 4.10

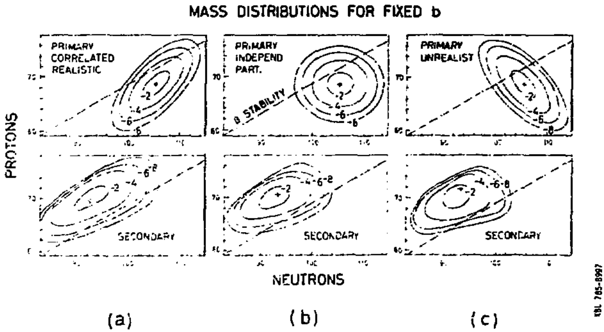

Figure 4.11

data. The uncorrelated calculation (hypergeometric) gives too large a width, essentially because it allows for unphysical possibilities such as removing *all* "a" nucleons as neutrons and protons alone. (The shift of the theory from the data is due to the neglect of the ablation stage.) Very similar considerations entered into the evaluation of the correlated widths σ_a, σ_{t_3} in Equ. 4.9. 4.10.

The subsequent ablation stage, in drifting the primary distribution back to the valley of stability, tends to erase the memory of the primary. The effect is illustrated in Fig. 4.11; the top sections display the primary abrasion distributions for (a) correlated, (b) uncorrelated and (c) unrealistic ground state motion. After the ablation stage (bottom) the distributions begin to look similar, but some influence of the primary persists.[365] Returning to experimental data in Fig. 4.9(b), it is clear that very careful measurements will be called for, since the completely different deeply-inelastic reaction ^{40}Ar + ^{48}Ca at 6 MeV/A[177] and the P + ^{238}U reaction at 800 MeV[380] give very similar distributions. (The points for both reactions were deduced from adding up counts from the published spectra and are thereby not very accurate.) Remember that the deeply-inelastic cross sections *also* arise from an equation like 4.9 (see 3.7), but the physics in the *primary* dispersions is quite different. What is clear however is the radical difference in the position of the peaks of the distributions. A more graphic demonstration appears in Fig. 4.12 which shows that the $\overline{N}/Z$ value for the deeply-inelastic reactions reflects more the value of the composite dinuclear system (due to the rapid equilibration of this degree of freedom, see Lecture 3) whereas at high energy the faster abrasion mechanism reflects the N/Z of the projectile, and the target acts as a "spectator." It is also clear that abrasion reactions such as ^{40}Ar + ^{232}Th, or better ^{48}Ca + ^{232}Th, at energies in the region of 200 MeV/A could be a powerful means of producing nuclei far from

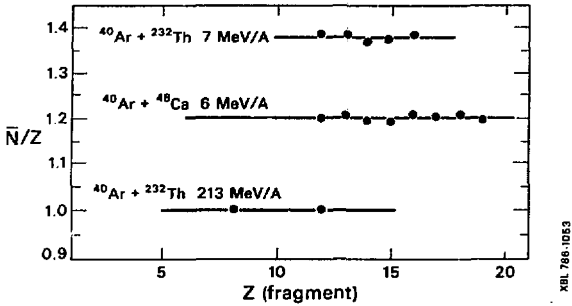

Figure 4.12

stability,[365,373] where the detection problems are simplified by the high emerging velocity of the fragments.

More detailed measurements as a function of energy for many systems must be made before a clear picture will emerge. Already departures from the skeletal framework of Fig. 4.5 may be cropping up in recent studies of $^{16}O + ^{197}Au$ reactions at 90 MeV/A.[381] One piece of evidence appears in Fig. 4.13, where the momentum widths of the fragments are compared with the parabolic dependence inherent in Equ. 4.15, evaluated with $\sigma_0 \approx 86$ MeV/c typical of the other data in Fig. 4.5. The systematics are obviously grossly violated. The data at 20 MeV/A may not therefore reside in Asymptotia as suggested by our earlier discussion, and implied by some other features. One characteristic of asymptotic behavior is factorization of the cross

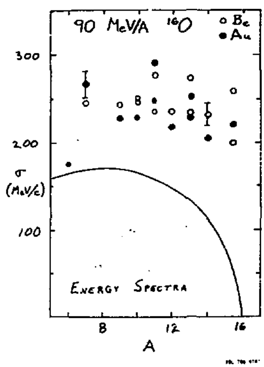

Figure 4.13

sections into a projectile and target term.[382-384] For the reaction $A + T \rightarrow F$ + Anything:

$$\sigma^F_{AT} = \sigma^F_A \ \ \gamma_T \tag{4.20}$$

This behavior is a logical consequence of the dependence $\sigma \propto \exp(Q_F/T)$ but not of the deeply-inelastic dependence

$$\exp \frac{Q_{gg}-\Delta V_c}{T}$$

of Equ. 4.6, since the substantial differences of Q-value for different targets would lead typically to an order of magnitude change between Pb and Au targets. The factorization appeared to hold at both 20 MeV/A and 2.1 GeV/A but not at 8 MeV/A.[382] A direct reaction model of peripheral fragmentation also leads to the observed factorization.[385] The phenomenon is also reminiscent of the Bohr independence hypothesis.[357,386] A dramatic illustration of the factorization and limiting fragmentation hypothesis (i.e., yields independent of energy[388]) is given in Fig. 4.14, which compares the yields of target fragments produced by protons at 3.9 GeV/A ^{14}N ions (upper curve) and 3.9 GeV protons (lower curve). (The data are displaced by a factor of 10 for display.) Other experiments also indicate that the distributions become similar for protons, of equivalent total energy as the heavy-ion, rather than of similar velocity.[389]

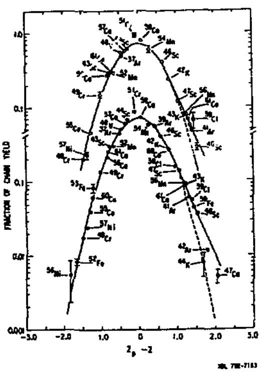

Figure 4.14

4.2 Central Collisions

Relativistic energies mark a change in the ability of a nucleon to pass through the nucleus. Above 1 GeV the longitudinal momentum decay length appears to grow to over 4 fm and begins to approximate nuclear dimensions; the colliding nuclei could then pass right through each other.[390] The consequences of the collision will vary depending on whether the collision is peripheral or central. Fig. 4.15(a) and (b) illustrates examples of the two types. In (a) the peripheral collision[391] of 870 MeV/A ^{12}C results in a small number of particles, continuing in the projectile direction. For the central collision in (b), there is a star explosion[392] of Ar + Pb at [illegible] GeV/A; the total multiplicity of charged particles ranges up to [illegible] suggesting that the initial system is completely disintegrated

Figure 4.15

(far from passing through each other!). At lower energies, we have seen that central collisions lead to fusion or fission. Although the nature of the central collision is very different in the two regimes, it appears that the onset of these more catastrophic processes takes place at roughly the same overlap of nuclear matter densities.[49] To see this[342,350] we write the reaction cross section as the sum of peripheral and central cross sections:

$$\sigma_R = \sigma_P + \sigma_c \tag{4.21}$$

and compare values of σ_c deduced from this equation by subtracting the summed peripheral cross sections of all reaction products in $^{16}O + ^{208}Pb$ at 20 MeV/A and 2.1 GeV/A (last section) from the reaction cross section, which has been measured directly at 2.1 GeV/A and was deduced from the optical model analysis of elastic scattering at 20 MeV/A.

Energy	Reaction	Peripheral σ (mb)	Total reaction σ (mb)	Central σ (mb)
20 MeV/A	$^{16}O+^{208}Pb$	1295	3460	2160
2.1 GeV/A	$^{16}O+^{208}Pb$	930	3100	2260

The reaction cross section has also been determined from ^{16}O reactions in emulsions in the energy range 75-150 MeV/A and appears to give similar values.[393] Such an energy independence would not be expected from the known (large) variation of the nucleon-nucleon cross section over the same energy region.[394]

In the central collisions of the type in Fig. 4.15(b), the most exotic features of high-energy heavy-ion collisions will be hidden--one says hidden because they must be separated from the large background of (possibly) trivial effects which are the outcome of the superposition of all the free nucleon-nucleon cross sections, properly folded with the particle distributions of position and momentum. The basic layout of a system designed to make quantitative studies of central collisions is shown in Fig. 4.16, which combines a particle identification telescope to identify a particular particle, with an array of plastic scintillators to determine the multiplicity of charged particles associated with each event.[395] A large multiplicity is used as a signature of a central collision.

Proton energy spectra from Ne and He bombardments of U are shown in Fig. 4.16 for angles of 30°, 60°, 90°, 120° and 150°

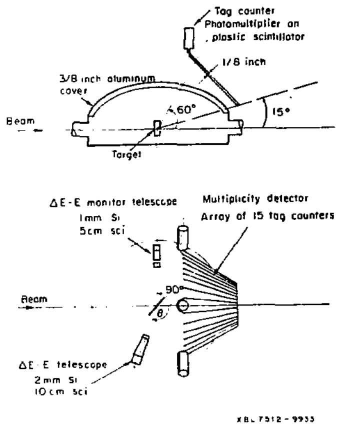

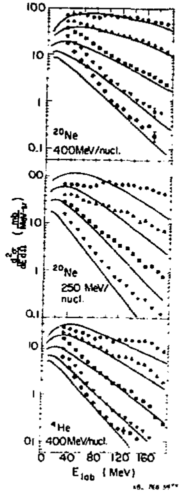

Figure 4.16

(except for Ne). The spectra have Maxwellian shapes corresponding to high temperature. These spectra have been elegantly explained with a fireball model,[395,396] illustrated schematically in Fig. 4.6(b). The model is an extension of the abrasion-ablation picture used previously for peripheral reactions. In the more central collision, nucleons swept out from the target and projectile form a quasi-equilibrated fireball at high temperature, equal to the available energy per nucleon. The velocity of the fireball is assumed to be that of the center of mass system of the nucleons swept out. The fireball expands isotropically in its center of mass system with a Maxwellian distribution in energy.

Assuming spherical nuclei and straight-line trajectories, the participating volume of each nucleus is easily calculated as a function of impact parameter. The number of participating protons as well as the division between projectile and target are shown in Fig. 4.17 for Ne on U. At the bottom is the effective weight, $2\pi b N_{proton}$, given to each impact parameter. The velocity of the center of mass of the fireball is then given by,

$$\beta_{cm} = \frac{P_{lab}}{E_{lab}} = \frac{N_p[t_i(t_i+2m)]^{1/2}}{(N_p+N_t)m+N_p t_i} \qquad (4.22)$$

where P_{lab} is the lab momentum, E_{lab} the total energy, t_i the

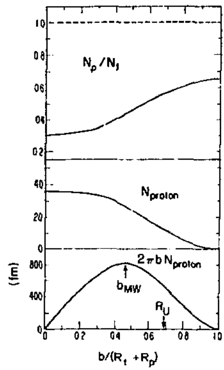

Figure 4.17

projectile incident energy/nucleon, and m the nuclear mass. The total energy in the center of mass of the fireball is

$$E_{cm} = \left[E^2_{lab} - P^2_{lab}\right]^{1/2} \tag{4.23}$$

If one assumes there are sufficient degrees of freedom in the fireball, and that there is a mechanism to randomize the available energy, one can define a temperature T, which can be expressed (non-relativistically) by:

$$\varepsilon = 3/2T \tag{4.24}$$

where ε is the available kinetic energy per nucleon in the center of mass, i.e., $E_{cm}/N_t + N_p$). The quantities β and ε (calculated relativistically) are given in Fig. 4.18 as a function of impact parameter. The momentum distribution of the fireball nucleons in the center of mass is then:

$$\frac{d^2N}{p^2 dp d\Omega} \propto (2\pi mT)^{-3/2} \; e^{-p^2/2mT} \tag{4.25}$$

where p is the momentum of a nucleon in the center of mass. Using the earlier expressions this distribution can be transformed to an energy distribution in the laboratory, which must then be integrated over impact parameter weighted appropriately (Fig. 4.17). The resultant distributions are shown in Fig. 4.16 (typical values of β and T can be derived from Fig. 4.18 at the point of maximum weight ($\beta \approx 0.25$ and $T \approx 50$ MeV)). Fairly satisfactory agreement with the data is obtained. (Note: the data shown in Fig. 4.16 have an error of absolute normalization, and the authors of Ref. 395 should be consulted for corrections.) Recently more advanced versions of the model such as the diffuse firestreak[397] have been developed, but its success is less obvious in view of the data errors. For a review of the various approaches, see Ref. 398.

It is possible to advance further and explain the distributions of other fragments heavier than the proton with a *coalescence model*.[397] If any number of protons and nucleons corresponding to a bound nucleus are emitted in the reaction with momenta differing by less than a "coalescence radius" p_0 (a parameter to be adjusted which comes out at 130 MeV/c typical of Fermi momenta), they are assumed to coalesce. The cross sections for these heavier nuclei are then trivially related to those for the proton. However, there are also thermodynamic models which extend the fireball concept to the emission of complex fragments.[400]

Fragments from central collisions may originate from several qualitatively different subsystems, such as the fireball, the target spectators, or even an explosion of the fused target

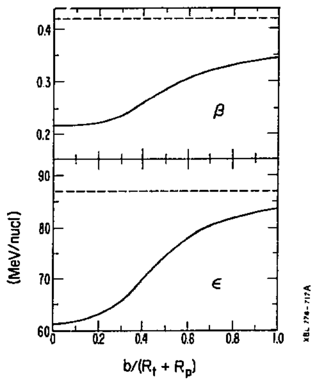

Figure 4.18

projectile system. The detailed distribution of the longitudinal and transverse momenta *of all the fragments give information on* these subsystems. For this purpose it is convenient to characterize the distribution of longitudinal momentum by the *rapidity variable*:

$$y = \tfrac{1}{2} \ln \frac{(E + p_{\parallel})}{(E - p_{\parallel})} \qquad (4.26)$$

where E and $p_{\parallel}$ are the total energy and longitudinal momentum of the particle. (This variable is convenient in relativistic systems because it transforms in Galilean fashion in changing frames.) Contour plots of invariant cross sections, which are measured as a function of angle, are transformed to these variables in Fig. 4.19 for inclusive proton spectra for the reactions[40] 800 MeV/A ^{20}Ne + Pb → p + x. These data were taken with a target centered rotating magnetic spectrometer to obtain data at high $p_{\perp}$ for production angles $15° \leq \theta_c \leq 145°$ and proton momenta in the interval $0.4 \leq p \leq 2.4$ GeV/c. The half rapidity line that corresponds to the velocity of the nucleon-nucleon center of mass frame is marked. The mountain top of the cross section is found for $p_{\perp} \lesssim 300$ MeV/c, $y \simeq \beta \lesssim 0.1$. Most of the protons have small transverse momentum and come from a source that moves slowly in the laboratory (target spectator decays). Towards high $p_{\perp}$ *the contour lines move up in y* but always bend round at a y smaller than $(y_T + y_p)/2$. The apparent proton source moves slower than the nucleon-nucleon center of mass. Over a wide *range* of $p_{\perp}$ the apparent source rapidity coincides with the fireball, which by equ. 4.22, is around 0.4 for this system. Similar studies for Ne + NaF (i.e., an almost equal mass target and projectile) which should have $y = (y_T + y_p)/2$, do not entirely support the elemental concept of the fireball but, at the least, call for refinements that allow a continuum of source-velocities.

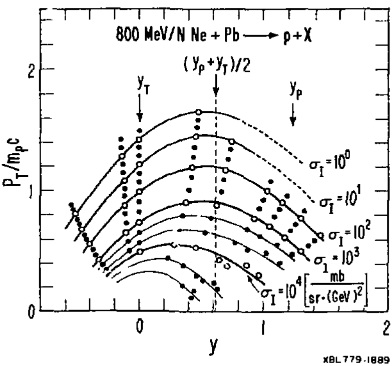

Figure 4.19

Data obtained with the very different techniques of stacked Lexan foil detectors give evidence for emission of complex fragments from a source moving with low velocity *and* high temperature,[402] which cannot be accommodated in the framework of a fireball. These fragments appear to originate from non-equilibrium emission from a system like the entire target, where the internal energy does not have to reach the value of $\frac{3}{2}$ T per nucleon. The radial emission velocity in the source frame is strongly correlated with the source velocity, independent of the mass of the fragment observed. This behavior is uncharacteristic of a thermalized source.[403] Various cooperative, non-thermal processes can be imagined, amongst which are compressional wave phenomena or the release of preexisting clusters. These ideas will be the topic of the last section, 4.5.

The fireball model was introduced in relativistic hadron and heavy-ion collisions and led to great early insight into the complex processes that take place when heavy ions collide. The model no longer enjoys unqualified success in its own territory, but it is now applied to shed light on reactions at much lower energy. Beggars (the nuclear physics community) do not mind picking up the crumbs that fall from the rich man's table (high energy physics). We can consider the logical limit of the fireball approach as the incident energy is decreased. It works at 250 MeV/A and it might work at 100 MeV/A. At still lower energies there cannot be a fireball, clearly separated from the intersecting nuclei, but can we imagine that the process degenerates into a local heated region? The possibility of the process depends on the reaction time compared to the time for transporting the local excitation outwards into the surrounding nuclear media. As we have seen (Fig. 3.25) this time increases at high energies. Presumably this concept of the "fireball" merges with the "hot-spot" discussed in Section 3.5 of Lecture 3. Some justification for the validity of this approach at least down to 20 MeV/A comes from the successful application of the Glauber model to describe complex fragment yields at 315 MeV (See Eq. 4.7, 4.8). To establish another link between the asymptotic and low energy regimes, let us look again at the fireball data of Fig. 4.16 compared with a cascade calculation [404] in Fig. 4.20. The simultaneous evolution of all projectile and target cascade particles is followed. Pion production and absorption are included via $NN \rightleftarrows N\Delta$, and experimental cross sections are used to determine the outcome of two-body collisions. Diffuse nuclear surfaces, Fermi motion, the exclusion principle and binding energy effects are also included. The inner workings of these very expensive and complicated computer calculations are beyond the comprehension of non-technicians, but they clearly do a good job in describing the data. This success does not signal a defeat for the fireball model; because the cascade model shows that complete thermalization is achieved for central collisions (but not for larger impacts parameters).

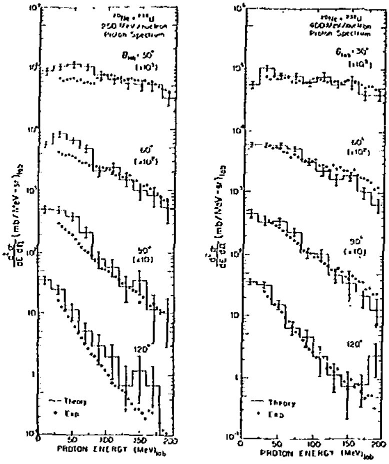

Figure 4.20

Compare now the proton energy spectra[405] from the collision of ^{12}C with ^{56}Fe at a *total* energy of 192 MeV (i.e. only 16 MeV/A!) in *Fig. 4.21(a). The trend of the data is indicated by the solid* lines, again the spectra are statistical in appearance, but by extending with substantial cross sections up to 70 MeV, requires a temperature far in excess of the compound nucleus. (The center of mass energy of 130 MeV above the barrier gives rise to T = 3.9 from the expression $E^* = \frac{A}{8} T^2$, and a resultant decrease of 10^5 in

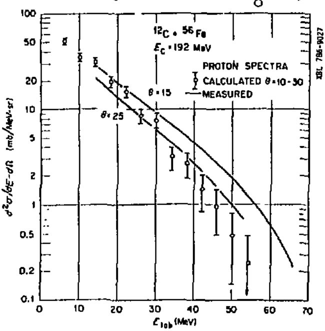

Figure 4.21(a)

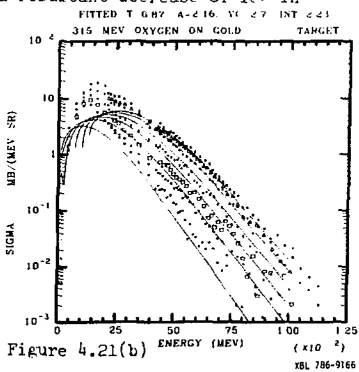

Figure 4.21(b)

in cross section between 10 to 60 MeV compared to the observed factor of 10^2). These data are also fitted by a cascade calculation[406] open circles). An analysis of the output suggests that the protons are evaporated by the *projectile*, which is excited in the collision and sequentially decays.[407] The high energy protons are produced by the vector addition of the low velocity decay in the projectile frame and the high projectile velocity.

Closer investigation suggests that this explanation may have a flaw. The data[408] in Fig. 4.21(b) for ^{16}O + ^{288}Pb at 315 MeV cover a wider range of angles from 20° to 80°. Over this region the spectra do not fall off sufficiently rapidly to be attributed to projectile decay. On the other hand they fall off too quickly to originate from the compound nucleus. Rather the data call for an intermediate number of nucleons moving with an intermediate velocity, *just as in the fireball*. The solid lines are in fact fits to the high energy parts of the spectra using eqs. 4.22-4.25 but replacing the ideal gas (Eq. 4.24) by the equivalent expression for a degenerate Fermi gas. The fits result in a temperature of 6.9 MeV (compared to the strict fireball prediction of 5.9 MeV) from a source of approximately 30 nucleons moving with half the projectile velocity. *The temperature of 6.9* MeV is almost the same as the value deduced for the emission of complex fragments at the same incident energy (see the discussion of Fig. 4.5).

Similar descriptions of proton spectra have been reported in α-particle induced reactions at energies of 25 MeV/A[409] and 180 MeV/A.[410] The formation of a localized hot spot has also been discussed in the analysis of a preequilibrium component in neutron spectra of ^{20}Ne + ^{150}Nd, leading to a temperature of 6 MeV and 25 participating nucleons.[411] Yet another approach[412] is to describe

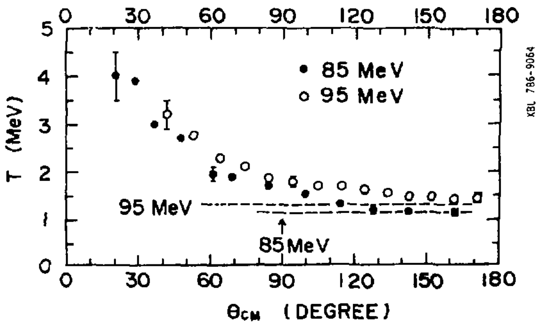

Figure 4.22

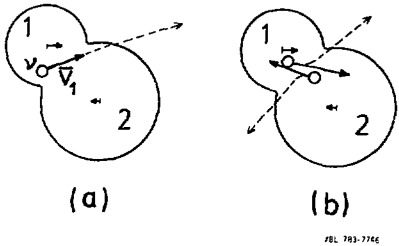

Figure 4.23

the energy spectra with an angle dependent temperature in reactions with ^{14}N on ^{209}Bi. Local heating takes place at the contact point, due to strong frictional forces, and alpha particles are emitted from the rotating surface (compare our discussion of hot-spots in Section 3.5). We have already seen that the rotation angle is intimately related to reaction time, in deeply-inelastic phenomena. As the system rotates the temperature drops according to the conductivity and specific heat of nuclear matter. Figure 4.22 shows the temperature and number of participating nucleons as a function of angle. The values for a completely equilibrated compound nucleus are given by the dashed lines, which are approached after 3/4 of a revolution.

There are other explanations in vogue for the explanation of energetic light particle emission in heavy-ion reactions. For example, Fig. 4.23 shows[339] a heavy-ion reaction at relative speed V of nucleus 1 at the ion-ion barrier. A nucleon ν moving from 1 to 2 has on arrival a velocity $\underline{v}_2 = \underline{v}_1 + \underline{V}$ where v is its velocity in nucleus 1, with a maximum of $v_F + V$. The maximum kinetic energy is:

$$E(\max) = E_F + E_{rel} + 2\sqrt{E_F E_{rel}} \qquad 4.27$$

For a 20 MeV/nucleon with E_F= 35 MeV, E reaches 108 MeV. An extension of the model to "Fermi-Jets" has recently been developed[413] and studied experimentally.[414] The emission of fast light particles is also encountered in time-dependent-Hartree-Fock calculations[415] and in hydrodynamic calculations.[416] A standing wave is set up and the nucleus fractures at the weakest point, which is a node of the standing wave located at a distance π/k_F from the surface. The two types of calculations are compared in Fig. 4.24 for a collision

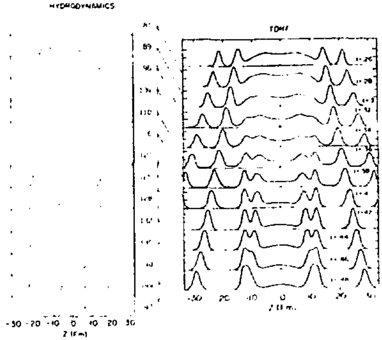

Figure 4.24

XBL 783-7747

energy of E/A = 100 MeV/nucleon. The numbers at the right give the time expressed in units of fm/c in the hydrodynamical calculations, and in units of 10^{-21} sec for the *TDHF*. *In both calculations a* small piece of nuclear matter is ejected with higher than beam velocity.

In low energy light-ion reactions there are well developed *preequilibrium theories for fast particle emission (see refs.* 315-322 & 417). A critical question in these theories is the correct initial exciton number to use. For α-particle induced reactions there is evidence that the correct number is four, for two protons and two neutrons.[417] In heavy-ion reactions one might assume that the heavy ion, eg. ^{12}C, breaks up into 6p + 6n, and the number of excitons would be 12. Calculations[417] based on this hypothesis for

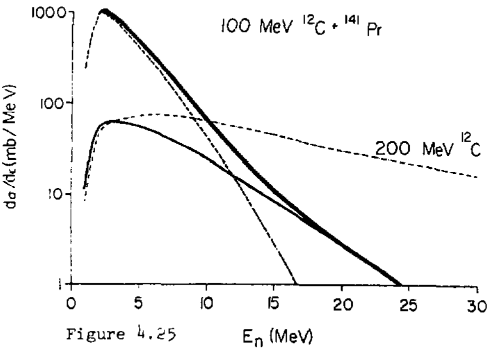

Figure 4.25

XBL 786-9071

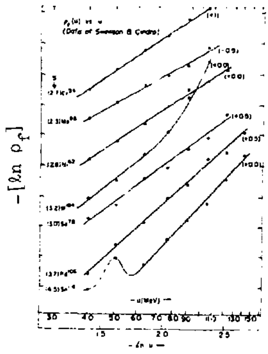

the ^{141}Ir(^{12}C,n) reaction are shown in Fig. 4.25(a). The dashed line for 100 MeV represents essentially compound nuclear evaporation (dashed line) with a small preequilibrium component. Now note the dramatic change at 200 MeV, where the huge increase of the preequilibrium emission leads to a cross section extending out to very high energies, just as in the ^{12}C and O^{16} induced reactions of Fig. 4.21. The preequilibrium emission becomes important when the excitation energy of the compound system becomes comparable with the particle binding energy/exciton. A method of finding out the number of excitons is to plot[418] the log of the differential cross section versus the log of the residual excitation and the slope gives the (number of excitons-2). An example for α-induced reaction is given in Fig. 4.25(b) on a variety of targets; the slopes, marked on the left hand side, are typically about 3 (a similar plot for the O^{16} induced reactions of Fig. 4.21(b) yields 25, very close to the number of particles in the fireball calculation!

All the above lengthy discussions, (which are a considerable digression from our description of central, relativistic heavy-ion collisions) are meant to emphasize that the questions of localization, hot spots, high temperatures and the like are not unique to the province of Asymptotia. These phenomena are firmly rooted throughout the whole physics of light and heavy-ion collisions and their interpretation will call for all the tools of nuclear dynamics, whether microscopic or macroscopic, at high or low energies. We have to understand how the central collisions at low energies evolve from fusion, fission and deeply-inelastic processes to the more catastrophic event of Fig. 4.15. There are already intimations on how to treat these problems.[419,420]

As a final illustration[317] look at the two spectra in Fig. 4.26, which compares p+p collisions at 100 GeV/c with ^{89}Y(p,n) at low

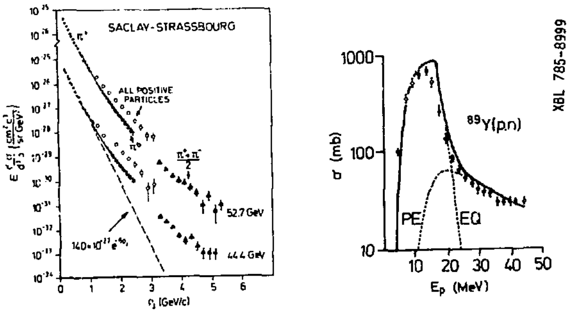

Figure 4.26

energies of 30 MeV. Both spectra have a "low temperature" component (in the p+p case $T \approx m_\pi$ the limiting temperature discussed in the introduction to Lecture 1) and a "preequilibrium tail". Both can be considered as local, instantaneous equilibrium in a hot spot.[32] All the experiments proposed to measure[421] the size and lifetime of the fireball from the small angle correlations[422] by adapting the Hanbury-Brown and Twiss technique to measure the size of stellar objects, must also be applied to the lower energy region. The method has already been used with pions to determine[423] the size of the [illegible] fireball. This unity between low and high energy regimes is aesthetically pleasing, but it is to be hoped that relativistic heavy-ion collisions will also reveal totally new phenomena in the nature of nuclear matter under extreme conditions, which will never be realized at lower energies or with lighter particles. To this topic we devote the last section of our lectures.

4.3 Six Impossible Things

My title is taken from "Alice in Wonderland", when Alice finds herself in the Garden of Live Flowers (remember the search for exotic phenomena is often compared to searching for flowers among weeds!) confronted by the White Queen. "You, my dear, must learn to think of impossible things," said the Queen. "But that is so difficult," said Alice. "And besides, what's the use? One can't [illegible] impossible things." "I daresay you haven't had much practice," said the Queen. "Why, when I was your age, I always did it for six hours per day. Sometimes I've even thought of as many as six impossible things before breakfast!" By and large I have not talked to you of impossible things. Rather, as quoted from James Joyce in the introduction to the Annotated Version of "Alice in Wonderland", I have "wiped my glosses with what I know"! For a detailed discussion of impossible things, I refer you to many excellent review articles.[[illegible],342,341,424–426]

An important basic question in complex nucleus-nucleus interactions is to what extent they can be traced back to quasi-free hadron-hadron collisions. Is the total energy available in the system, viz. $E_{inc}\, A_1A_2/A_1+A_2$ GeV, the important quantity or is it just $\approx (\sqrt{2}\, E_{inc} + [illegible])$–2 GeV that is available $\leq A_1$ nucleon-nucleon reactions? The difference between these pictures is important. If we find pion production at 0.1 GeV/A, the former expression must be relevant, and *collective* phenomena are important, and have already been claimed to be observed,[427] but more recent experiments yield contradictory evidence.[428–429] Many experiments are in progress, and it is clear that the great majority of events can be easily explained in an independent nucleon-nucleon model.[[illegible]] There are also some indications in pion multiplicities for production via strong nucleon correlation effects,, which hopefully may be a signature for shock waves.[361]

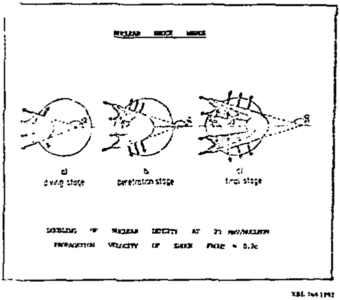

Figure 4.27

It has been suggested that a compressed zone of high energy density may be formed in a central collision, which propagates as a shock wave and could lead to the emission of energetic fragments upon impinging at the nuclear surface.[430-431] Such a propagation of high compression ($\rho > \rho_o$) and with velocities $v_s > 0.2c$ has been called a "shock wave." The progress of this wave is illustrated in Fig. 4.27. In the initial phase a "splashing tidal wave" is expected at a backward angle $\sin\phi_1 = v_t/v_i$, where v_t is the expansion velocity of the shock compression zone. In the second stage a strong compression shock is created accompanied by a Mach cone traveling outwards in the direction $\phi_2, \cos\phi_2 = v_s/v_i$, where v_s is the shock expansion velocity. In the final stage, matter is emitted in the directions ϕ_1(splashing) and ϕ_2 (Mach).

In reality the projectile would slow down considerably and the simple Mach cone picture is distorted. The emission is then spread out over a wider angular region, which actually appears to be a feature of hydrodynamical calculations of collisions of nuclear matter, treated as a classical compressible fluid.[434] The criterion for compressibility is whether flow velocities are comparable to the speed of sound. For nuclear matter with an incompressibility K(MeV) the speed of sound is[435]

$$v_s = (K/9mo)^{\frac{1}{2}} \qquad 4.28$$

and the projectile energy/nucleon above the Coulomb barrier required to reach such a velocity is:

$$E/A = K/18 \qquad 4.29$$

For typical values of K between 150 and 300 MeV, v_s is derived to be 0.13 and 0.19c, for E/A of 8 and 17 MeV. Apparently compressibility will be important at the relativistic energies we have been discussing. For a hydrodynamic description to be valid, the mean free path of the microscopic particles should be small compared to the macroscopic dimensions. From the known nucleon-nucleon cross section of 40 mb at 2 GeV, we can estimate the mean free path $\lambda \approx 1/\rho\sigma \approx 2$ fm. So the criterion is only marginally fulfilled. The hydrodynamical equations have been solved[4,434] for collisions of ^{20}Ne on U (the reaction used for the fireball discussion) at 250 MeV/A. Figure 1.3 showed the time development of the density as represented by the distributions of particles, for different impact parameters. For the nearly central collision (labeled 0.1) the neon penetrates into the uranium nucleus and sets off a strong shock wave (clearly visible at 5.1×10^{-23} sec). Subsequently most of the energy of the projectile is thermalized and the nucleus expands. The other two sections illustrate an intermediate impact parameter (which should come close to the fireball description), and a peripheral collision in which we see a part of the projectile sheared off (just as in the abrasion picture). When the angular distributions for central collisions are computed from the distribution of nucleons in the final state they lead to rather featureless exponential forms, with no sharp shock wave peak.

Another way of treating the density problem is by introducing statistical microscopic calculations.[436] These make Monte Carlo simulations of colliding samples of almost free point nucleons. The nucleon-nucleon scattering follows the known cross sections, conservation of energy, momentum, and angular momentum. The position and velocity of each nucleon is known (in principle) at each time. These calculations indicate that the transparency effects are too large to give high enough compression to produce shock waves.

Nevertheless, they have been searched for,[437] and the first experiments made extensive studies of high multiplicity events in track detectors using AgCl crystals and emulsions. The distributions of $d\sigma/d\theta$ were measured for events with more than 15 prongs, and a typical example[437] appears in Fig. 4.28(a). The sharp peak seemed to shift its position in a way characteristic of Mach shocks with a propagation velocity,

$$v_s = v_i \cos\theta(\text{peak}) \qquad 4.20$$

and the peak moves *backwards* with increasing energy. These peaks have not been found in other emulsion experiments, nor are they present in the differential cross sections obtained with the live counter techniques.[438] It seems that the peaks are due to

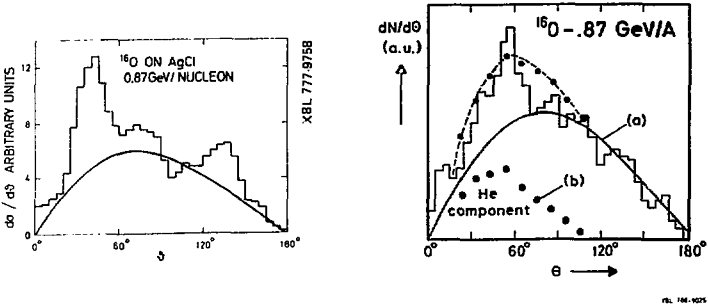

Figure 4.28

combinations of different particle types, such as protons and alphas which were selected by the experimental technique at different energies.[439] (Fig. 4.28(b) shows both components and the sum.) Other experimental searches for shock waves have not yielded positive results (see Ref. 337, p. 38 for a summary) and it must be concluded that there is no proof of their existence. Equally, though it is not clear these experiments were capable of establishing the existence of such effects, in that they were predominantly single particle inclusive measurements, lacking essential information on multiplicities. This criterion cannot be levelled at a recent study of the $^{40}Ar + {}^{9}Be$ reaction at 1.8 GeV/A.[440] A test was made of the possible correlations between a particular multiplicity M and the inclusive cross section W, by the ratio $r = W_M(\theta_L, Y_L)/W(\theta_L, Y_L)$ as a function of the laboratory

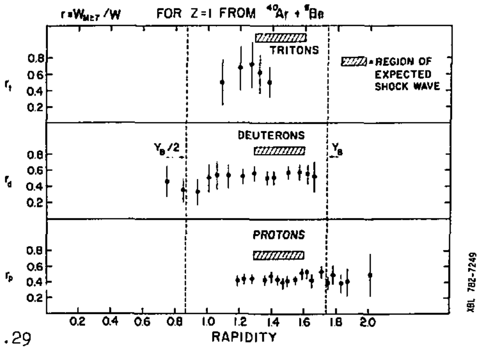

Figure 4.29

angle θ_L and the rapidity YL. This ratio is shown for p, t, d in Fig. 4.29. The multiplicity requirement was that at least seven fragments are detected by an Array of Cerenkov detectors. According to a shock wave model,[441] the fragments from a shock wave in the projectile would peak at rapidities indicated by the shaded region. The evidence is negative.

Only the first generation of experiments have been completed, which have primarily looked at single particle inclusive spectra. There are many refinements in progress to search for collective effects of nuclear matter at extreme density and pressure — conditions which are also probably realized in the interior of neutron stars. As an indication of some of the exciting possibilities ahead, Fig. 4.30 shows the anticipated equation of state. This equation, at densities above twice normal, can be affected by collective phase transitions to Lee-Wick abnormal matter,[442] density isomers or higher order transitions to a pion condensate,[337,341,443] the experimental signatures of which have recently been discussed.[444] In the absence of these effects the energy would simply increase monotonically with density. Since pressure in a hydrodynamic models is proportional to dE/dρ, a change to negative slope above twice normal density would imply negative pressure, e.g. condensation to abnormal matter. The most favore possibility now is a transition to quark matter, in which these hypothetical constituents of strongly interacting particles (hadrons) would not be confined to individual nucleons but instead could move separately through the nucleus.[445] A possible signal for these new states of matter would be some unusual thermodynamic property of matter at high baryon density. One proposal (discussed by Glendenning in this Study) extends the speculations about hadron structure[158] to the heavy-ion domain, raising the possibility that

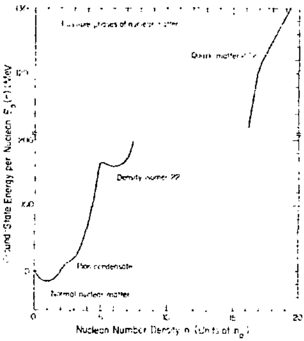

Figure 4.30

dense matter might exhibit a limiting temperature $T \sim m_\pi \approx 140$ MeV, as we discussed[7] at the beginning of Lecture 1, and which many have been observed in hadron collisions. It has been said[446] that "U+U collisions in the region of 4 GeV/A might produce important new phenomena, perhaps even practical applications. It should be noted that unlike hadron collisions these effects are not duplicated in accessible astronomical processes. They would be unlikely to occur except in gravitationally collapsing objects, or in the inverse process to the Big Bang. The lack of astronomical information means that we must depend on theoretical estimates to deduce the consequences of the stability of matter with supernormal density. Evidently this could be a potential energy source, since it could swallow up nucleons and disgorge energy, but equally evident is the possibility that the swallowing forces would be hard to control."

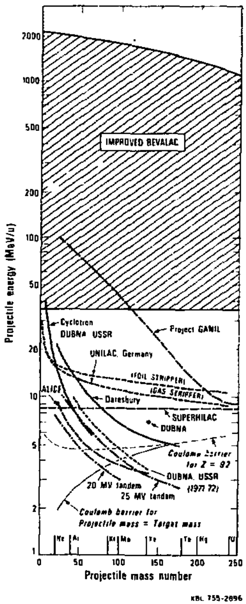

Figure 4.31

Whatever the theoretical speculations, the ultimate test will come from the experiments conducted on the present heavy-ion accelerators (see Fig. 4.31) although some of these studies call for yet another generation of accelerators, reaching energies of 20 to 100 GeV/nucleon, beyond even the range of the upgraded Bevalac. With the last statement, I must surely have covered at least six Impossible Things and I shall stop!

4.4 Envoi

In these lectures I have attempted to given an overview of current activities in the different areas of nuclear reactions with heavy ions. My selection of material was guided to some extent by an attempt to show that the subjects of Microscopia, Macroscopia and Asymtotia are not separate and distinct. The rate of exploration and development on all three continents is truly remarkable, and dispenses with the criticisms of many "doubting Thomases" in the early days of heavy-ion research, who insisted that the processes would be so complicated as to defy even a qualitative understanding. Nor should we be deterred by the critics who insist that all the same phenomena can be studied more easily in hadron reactions. The fact is that they *were not so studied* until stimulated by heavy-ion research, and this is true of locating high spin states in nuclei or of forming nuclear fireballs. We have only to look at the quality of heavy-ion *data* and the sophistication of our present microscopic theories of multistep processes in deformed rare-earth nuclei, to wonder whether our tools would be of poorer quality without the advent of heavy ions.

My lectures must seem a little like a helicopter tour over the Continental Jungles. We have not flown very high (this is the task of other lecturers) but neither was your pilot skillful or knowledgable enough of the terrain to set down in the dense undergrowth. The metaphor of the Jungle is apt, because that is what experimental physics is like. Since this School is mainly a Theoretical Study we do well to recall Max Born's words[417] on the relationship of Experimental Theory in Physics. "I believe there is no philosophical high road in Science, with epistemological signposts. No, we are in a jungle and find our way by trial and by error, building our road behind us as we go. We do not find signposts at the crossroads, but our own scouts erect them to guide the rest. Theoretical ideas may be such signposts. The difficulty is that they often point in opposite directions: two theories each claiming to be built on "a priori" principles, but widely different and contradictory."

At the moment it is not clear where the many paths will lead in heavy-ion physics, but wherever, we can be assured that we have embarked on one of the voyages of the Century. The analogy is often made that research in heavy-ions is like looking for flowers among the weeds, and if any sign of flowers are evident in the weeds of these lectures, then it is only because I have merely "made up a bunch of other men's flowers and provided little of my own but the string to bind them".[148] Therefore as a tribute to the many people whose research I have used, without proper interpretation or acknowledgement, let me end with a description[149] of how the Jungle will look one day, as neat manicured lawns and flower beds.

"...Such gardens are not made,
By singing: 'Oh, how beautiful!' and
sitting in the shade,
While better men than we go out and
start their working lives,
At grubbing weeds from gravel paths
with broken kitchen knives.
Oh, Adam was a gardener and God
who made him sees
That half a proper gardner's work is spent
upon his knees,
So when your work is finished you can
wash your hands and pray
For the Glory of the Garden, that it may
not pass away!
And the Glory of the Garden it shall never
pass away!

ACKNOWLEDGMENTS

I wish to thank the many workers in the field of heavy-ion physics who have written excellent reviews which helped me to prepare these lectures, and the many individuals mentioned in the text who sent me preprints on recent developments. Also, I owe an enormous debt to my immediate colleagues in Berkeley, M. Buenerd, M. Bini, P. Doll, C.K. Gelbke, D.L. Hendrie, J.L. Laville, J. Mahoney, G. Mantzouranis, A. Menchaca-Rocha, M.C. Mermax, C. Olmer, T.J.M. Symons, Y.P. Viyogi, K. Van Bibber, H. Wieman, P.J. Siemens, H. Faraggi, B.G. Harvey, F. Beiser, H. Crawford, D.E. Greiner, H.H. Heckman, P. Lindstrom, G.D. Westfall, C. McParland, S.A. Chessin, J.V. Geaga, J.Y. Grossiard and L.S. Schroder. In addition I have absorbed many ideas from the wider milieu of research and research workers at Berkeley. Finally it is a pleasure to thank: Shirley Ashley, Antoinette Czerwinski, Elaine Thayer, and Mike Baublitz of the Word Processing Dept; John Flambard and the staff of the Illustration Dept.; Marty Casazza, George Kagawa, Armand Ludtke, Alma Pedersen, Steve Yarborough, Robert Patterson, Church Lees and Steve Adams of the Photographic Dept. They all performed superhuman efforts cheerfully to get these lectures prepared.

This work was supported by the Department of Energy.

References

The list of references is not scholarly either in its completeness, or in its attention to historical development. The references are illustrative, and were readily accessible or well known to the author at the time of writing the Lectures. A careful reading of them will nevertheless provide an excellent introduction to heavy-ion experiments!

1. Halton Arp, Atlas of Peculiar Galaxies, published by California Institute of Technology, 1966.

2. A. Toomre and J. Toomre, Astrophys. Journal 178, 623 (1972).

3. J.P. Vary, Second High Energy Heavy-Ion Summer Study (Berkeley, 1974), Lawrence Berkeley Laboratory Report LBL-3675, p. 371.

4. A.A. Amsden, F.H. Harlow and J.R. Nix, Phys. Rev. C15, 2059 (1977).

5. F. Seidl and A. Cameron, Astrophys. and Space Sci. 15, 44 (1972).

6. W. Scheid, J. Hofman and W. Greiner, Ref. 3, p. 1.

7. N.K. Glendenning and Y. Karant, Phys. Rev. Lett. 40, 374 (1978).

8. A.T. Laasanen, C. Ezell, L.J. Gutery, N.W. Schreiner, F. Schubelin, L. von Linden and F. Turkot, Phys. Rev. Lett. 38, 1 (1977).

9. S. Weinberg, The First Three Minutes, A Modern View of the Origin of the Universe (Basic Books, N.Y. 1977).

10. Proceedings of the International Conference on Nuclear Reactions Induced by Heavy Ions, editors R. Bock and W.R. Hering (North-Holland, Amsterdam, 1970).

11. Proceedings of the International Conference on Heavy-Ion Physics (Dubna, 1971), JINR Report D7-5769.

12. Symposium on Heavy-Ion Reactions and Many-Particle Excitations (Saclay, 1971), Colloque du Journal de Physique 32, C6 (1971).

13. Proceedings of the Symposium on Heavy-Ion Scattering (Argonne, 1971), Argonne Report ANL-7837.

14. European Conference on Nuclear Physics (Aix-en-Provence, 1972), Colloque du Journal de Physique 33, C5 (1972).

15. Proceedings of Heavy-Ion Summer Study (Oak Ridge, 1972), editor S.T. Thornton, USAEC Report CONF-720669.

16. Proceedings of the Heavy-Ion Transfer Reaction Symposium (Argonne, 1973), Argonne Report PHY-1973B.

17. Proceedings of the International Conference on Nuclear Physics, editors J. de Boer and J.H. Mang (North-Holland, Amsterdam, 1973).

18. Proceedings of the International Conference on Reactions between Complex Nuclei, editors R.L. Robinson, F.K. McGowan, J.B. Ball and J.H. Hamilton (North-Holland, Amsterdam, 1974).

19. Second High Energy Heavy-Ion Summer Study (Berkeley, 1974), Lawrence Berkeley Laboratory Report LBL-3675.

20. Proceedings of the Symposium on Classical and Quantum Mechanical Aspects of Heavy-Ion Collisions, editors H.L. Harney, P. Braun-Munzinger and C.K. Gelbke, Lecture Notes in Physics 33 (Springer, Berlin/Heidelberg/New York, 1975).

21. Proceedings of the INS-IPCR Symposium on Cluster Structure of Nuclei and Transfer Reactions Induced by Heavy Ions (eds. H. Kamitsubo, I. Kohno and T. Marumori) Tokyo, 1975, IPCR Progress Report Supplement 4.

22. Proceedings of the Symposium on Macroscopic Features of Heavy-Ion Collisions (Argonne, 1976), Argonne Report ANL/PHY-76-2.

23. Third Summer Study of High Energy Heavy Ions (Berkeley, 1976), Lawrence Berkeley Laboratory Report.

24. European Conference on Nuclear Physics with Heavy Ions (Caen, 1976), Colloque du Journal de Physique 37, C5 (1976).

25. Theoretical Aspects of Heavy-Ion Collisions (Falls Creek, Tennessee, 1977), ORNL Report 770602.

26. Proceedings of the International Symposium on Nuclear Collisions and Their Microscopic Description (Bled 1977), Fizika 9, Supplement 3 and 4 (1977).

27. Proceedings of the IPCR Symposium on Macroscopic Features of Heavy-Ion Collisions and Pre-Equilibrium Processes (Hakone, 1977), eds. H. Kamitsubo and M. Ishihara, IPCR Progress Report, Supplement 6.

28. Proceedings of the International Conference on Nuclear Structure, ed. T. Marumori (Tokyo, 1977). Supplement-[illegible], J. Phys. Soc. Japan 44 (1978).

29. Heavy-Ion Collisions, ed. R. Bock (North Holland), to be published 1978.

30. D.K. Scott, Heavy Ion Experiments, Lectures presented in part at the Scottish Universities Summer School in Physics (St. Andrews, 1977) and the Latin American Summer School in Physics (Mexico City, 1977), Lawrence Berkeley Laboratory Preprint [illegible] (1977) and to be published.

31. D.A. Bromley, Ref. 17, p. 22.

32. A.S. Goldhaber, Ref. 19, p. 382.

33. D.A. Goldberg, Symposium on Heavy-Ion Elastic Scattering (Rochester, N.Y., 1977).

34. L.C. Vaz, J.M. Alexander and E.H. Auerbach; L.C. Vaz and J.M. Alexander, to be published in Phys. Rev. C, 1978.

35. T. Koeling and R.A. Malfliet, Phys. Reports 22C, 181 (1975).

36. J. Knoll and R. Schaeffer, Ann. of Phys. 97, 307 (1976).

37. D.M. Brink, Lectures on Heavy-Ion Reactions (Orsay, March, 1972).

38. W.E. Frahn, Ref. 20, p. 102 and refs. therein; see also the series of papers I, II and III on the Generalized Fresnel Model for Heavy-Ion Scattering by W.E. Frahn, to be published.

39. J.S. Blair, Phys. Rev. 95, 1218 (1954).

40. J.B. Ball, C.B. Fulmer, E.E. Gross, M.L. Halbert, D.C. Hensley, C.A. Ludemann, M.J. Saltmarsh and G.R. Satchler, Nucl. Phys. A252, 208 (1975).

41. G.R. Satchler, Ref. 18, p. 171.

42. P.R. Christensen and A. Winther, Phys. Lett. 65B, 19 (19[illegible]).

43. C. Olmer, M. Mermaz, M. Buenerd, C.K. Gelbke, D.L. Hendrie, J. Mahoney, D.K. Scott, M.H. Macfarlane and S.C. Pieper, Lawrence Berkeley Laboratory Preprint LBL-6553, to be published in Phys. Rev. C.

44. D.A. Goldberg and S.M. Smith, Phys. Rev. Lett. 29, 500 (1972).

45. J.G. Cramer, R.M. DeVries, D.A. Goldberg, M.S. Zisman and C.F. Maguire, Phys. Rev. C14, 2158 (1976).

46. D.F. Jackson and R.C. Johnson, Phys. Lett. 49B, 249 (1974).

47. R.M. DeVries, D.A. Goldberg, J.W. Watson, M.S. Zisman and J.G. Cramer, Phys. Rev. Lett. 39, 450 (1977).

48. J. Wilczynski and K. Siwek-Wilczynska, Phys. Lett. 55B, 270 (1975); J. Wilczynski, Nucl. Phys. A216, 386 (1973).

49. W.D. Myers, Nucl. Phys. A204, 465 (1973).

50. J. Blocki, J. Randrup, W.J. Swiatecki and C.F. Tsang, Ann. Phys. 105, 427 (1977).

51. D.M. Brink, Ref. 24, p. C-47.

52. J.R. Birkelund and J.R. Huizenga, Phys. Rev. C17, 126 (1978).

53. R. Bass, Phys. Rev. Lett. 39, 265 (1977).

54. J.P. Vary and C.B. Dover, Phys. Rev. Lett. 31, 1510 (1973).

55. G.R. Satchler, Ref. 18, p. 171.

56. W.G. Love, Phys. Lett. 72B, 4 (1977).

57. F. Beck, K-H. Müller and H.S. Köhler, Phys. Rev. Lett. 40, 837 (1978) and refs. therein.

58. D.M. Brink and Fl. Stancu, Oxford University Preprint, 84/77.

59. M.C. Lemaire, Phys. Reports 7C, 280 (1973).

60. W.R. Phillips, Rep. Prog. in Phys. 40, 345 (1977).

61. A.J. Baltz and S. Kahana, Adv. Phys. 9, 1 (1977).

62. M.C. Lemaire, Proc. of Int. Conf. on Clustering Aspects of Nuclear Structure and Nuclear Reactions (Winnipeg, Manitoba, 1978).

63. H.T. Fortune, Ref. 28, p. 99.

64. D.H. Wilkinson, *The Investigation of Nuclear Structure Problems* at High Energy. Proceedings of the International School of Nuclear Physics (Erice, 1974), ed. H. Schopper (North Holland, 1975), p. 1.

65. A. Mechaca-Rocha, D. Phil. Thesis, Oxford University (1974).

66. D.M. Brink, Phys. Lett. 40B, 37 (1972).

67. N. Anyas-Weiss, J.C. Cornell, P.S. Fisher, P.N. Hudson, A. Mechaca-Rocha, D.J. Millener, A.D. Panagiotou, D.K. Scott, D. Strottman, D.M. Brink, B. Buck, P.J. Ellis and T. Engeland, Phys. Reports 12C, 201 (1974).

68. K.P. Artemov, V.Z. Goldberg, I.P. Petrov, V.P. Rudakov, I.N. Serikov and V.A. Timofeev, Sov. J. Nucl. Phys. 24, 1 (1976).

69. A. Menchaca-Rocha, M. Buenerd, A. Dacal, D.L. Hendrie, J. Mahoney, C. Olmer, M.E. Ortiz and D.K. Scott, to be published.

70. B. Hamm and K. Nagatani, Phys. Rev. C17, 586 (1978) and refs. therein.

71. B. Buck and A.A. Pilt, Nucl. Phys. A295, 1 (1978) and refs. therein.

72. R.M. DeVries, D. Shapiro, W.G. Davies, G.C. Ball, J.S. Forster and W. McLatchie, Phys. Rev. Lett. 35, 835 (1975).

73. W.G. Davies, R.M. DeVries, G.C. Ball, J.S. Forster, W. McLatchie, D. Shapira, J. Toke and R.E. Warner, Nucl. Phys. A279, 477 (1976).

74. R.M. DeVries, J.S. Lilley and M.A. Franey, Phys. Rev. Lett. 37, 481 (1976).

75. D.F. Jackson and M. Rhoades-Brown, Nucl. Phys. A286, 354 (1977).

76. R.M. DeVries, D. Shapira, M.R. Clover, E. Gove, J.D. Garrett and G. Sorensen, Phys. Lett. 67B, 19 (1977).

77. R.A. Broglia and P.F. Bortignon, Phys. Lett. 65B, 221 (1976).

78. D.K. Scott, B.G. Harvey, D.L. Hendrie, L. Kraus, C.F. Maguire, J. Mahoney, Y. Terrien and K. Yagi, Phys. Rev. Lett 33, 1343 (1974).

79. G.T. Hickey, D.C. Weisser, J. Cerny, G.M. Crawley, A.F. Zeller, T.R. Ophel and D.F. Hebbard, Phys. Rev. Lett. 37, 130 (1976).

80. G.C. Ball, W.G. Davies, J.S. Forster and H.R. Andrews, Phys. Lett. 60B, 265 (1976).

81. I. Paschopoulos, E. Müller, H.J. Körner, I.C. Gebrich, K.E. Rehm and J. Scheerer, Munich Preprint (1978), to be published in Phys. Rev. C.

82. X. Campi, H. Flocard, A.K. Kerman and S. Koonin, Nucl. Phys. A251, 193 (1975).

83. K.F. Greider, Ref. 10, p. 217.

84. One of the most recent techniques for evaluating this integral is given by D.H. Glockner, M.H. MacFarlane and S.C. Pieper, Argonne National Laboratory Report ANL-76-11 (1976).

85. P.D. Bond, C. Chasman, J.D. Garrett, C.K. Gelbke, O. Hansen, M.J. Levine, A.Z. Schwartzchild and C.E. Thorn, Phys. Rev. Lett. 36, 300 (1976).

86. R.C. Fuller, Phys. Lett. 69B, 267 (1977).

87. E.A. Seglie and R.J. Asciutto, Phys. Rev. Lett. 39, 688 (1977).

88. G. Delic, K. Pruess, L.A. Charleton and N.K. Glendenning, Phys. Rev. Lett. 69B, 20 (1977).

89. For a recent summary, see. K.S. Low, Ref. 24, pC5-15.

90. K.S. Low, T. Tamura and T. Udagawa, Phys. Lett. 67B, 59 (1977).

91. P.D. Bond, M.J. Levine and C.E. Thorn, Phys Lett. 68B, 327 (1977).

92. K.E. Rehm, W. Henning, J.R. Erskine and D.G. Kovar, to be published in Phys. Rev. Lett. 40, 1479 (1978).

93. N.K. Glendenning, Rev. Mod. Phys. 47, 659 (1975).

94. D.K. Scott, B.G. Harvey, D.L. Hendrie, U. Jahnke, L. Kraus, C.F. Maguire, J. Mahoney, Y. Terrien, K. Yagi and N.K. Glendenning, Phys. Rev. Lett. 34, 895 (1975).

95. P.D. Bond, H.J. Körner, M.C. Lemaire, D.J. Pisano and C.E. Thorn, Phys. Rev. C16, 177 (1977).

96. J.C. Peng, M.C. Mermaz, A. Greiner, N. Lisbona and K.S. Low, Phys. Rev. C15 1331 (1977).

97. M.C. Lemaire and K.S. Low, Phys. Rev. C16, 183 (1977).

98. K.A. Erb, D.L. Hanson, R.J. Ascuitto, B. Sorensen, J.S. Vaagen and J.J. Kolata, Phys. Rev. Lett. 33, 1102 (1974).

99. C.F. Maguire, D.L. Hendrie, U. Jahnke, J. Mahoney, D.K. Scott, J.S. Vaagen, R.J. Ascuitto and K. Kumar, Phys. Rev. Lett. 40, 358 (1978).

100. B. Sorensen, Phys. Lett. 66B, 119 (1977).

101. K.W. McVoy, Proceedings of the Oaxtepec Symposium on Nuclear Physics (Mexico 1978); B.V. Carlson and K.W. McVoy, Nucl. Phys. A292, 310 (1977).

102. A.J. Baltz and S. Kahana, Phys. Rev. C17, 555 (1978).

103. T. Tamura, Phys. Reports 14C, 61 (1974).

104. For a review of experimental techniques, see P. Armbruster, Ref. 24, p. 161; the forthcoming issue of Nuc. Inst. and Meth. on Spectrometer Detection Systems, ed. by D.A. Bromley; and B. Engeland, Lectures at Scottish Universities Summer School in Physics (St. Andrews, 1978).

105. C. Olmer, M.C. Mermaz, M. Buenerd, C.K. Gelbke, D.L. Hendrie, J. Mahoney, A. Menchaca-Rocha, D.K. Scott, M.H. Macfarlane and S.C. Pieper, Phys. Rev. Lett. 38, 476 (1977) and refs. therein.

106. T.A. Belote, N. Anyas-Weiss, J.A. Becker, J.C. Cornell, P.S. Fisher, P.N. Hudson, A. Menchaca-Rocha, A.D. Panagiotou and D.K. Scott, Phys. Rev. Lett. 30, 450 (1973).

107. H.V. Klapdor, H. Reiss and G. Rosner, Eighth Summer School on Nuclear Physics (Mikolajki, Poland, 1975), Nukleonika 21, 763 (1976).

108. H.V. Klapdor, G. Rosner and H. Willmes, International Workshop V on Gross Properties of Nuclei and Nuclear Excitations (Hirschegg, Austria, 19[illegible]).

109. N. Marquardt, J. L'Ecuyer, C. Cardinal, R. Volders, and M.W. Greene, Ref. 17, Vol. 1, p. 476.

110. H.V. Klapdor, H. Reiss, G. Rosner and M. Schrader, Phys. Lett. 49B, 431 (1974).

111. M. Böhning, Ref. 10, p. 633; R.G. Stokstad, Ref. 18, p. 327.

112. H.V. Klapdor, H. Reiss and G. Rosner, Phys. Lett. 58B, 279 (1975).

113. D.A. Bromley, Second International Conference on Clustering Phenomena in Nuclei (Maryland, 1975); International Conference on the Resonances in Heavy Ion Reactions (Hvar, Yugoslavia, 1977).

114. H. Feshbach, Ref. 24 p. C5-177; Europhysics Conference on Medium Mass Nuclei (September, 1977).

115. R.H. Siemssen, Ref. [illegible], p. 233.

116. M.L. Halbert, C.B. Fulmer, S. Raman, M.J. Saltmarsh, A.H. Snell and P.H. Stelson, Phys. Lett 51B, 341 (1974).

117. A. Gobbi, R. Wieland, L. Chua, D. Shapira and D.A. Bromley, Phys. Rev. C7, 30 (1973).

118. R. Vandenbosch, M.P. Webb and M.S. Zisman, Phys. Rev. Lett. 33, 842 (1974).

119. K.S. Low and T. Tamura, Phys. Lett. 40B, 32 (1972).

120. E.R. Cosman, T.M. Cormier, K. van Bibber, A. Sperduto, G. Young, J. Erskine, L.R. Greenwood and O. Hansen, Phys. Rev. Lett. 35, 265 (1975).

121. A.J. Lazzarini, E.R. Cosman, A. Sperduto, S.G. Steadman, W. Thoms and G.R. Young, to be published in Phys. Rev. Lett. (1978); A.H. Lumpkin, G.R. Morgan, J.D. Fox and K.W. Kemper, Phys. Rev. Lett. 40, 104 (1978).

122. A. Arima, G. Scharff-Goldhaber and K.W. McVoy, Phys. Lett. 40B, 8 (1972).

123. K. Ikeda, Ref. 21, p. 23.

124. N. Cindro, F. Coçu, J. Uzureau, Z. Basrak, M. Cates, J.M. Fieni, E. Holub, Y. Patin and S. Plattard, Phys. Rev. Lett. 39, 1135 (1977).

125. B. Imanishi, Nucl. Phys. A125, 33 (1969).

126. H.J. Fink, W. Scheid and W. Greiner, Nucl. Phys. A188, 259 (1972).

127. J. Eisenberg and W. Greiner, Nuclear Theory (North-Holland, 1975) Vol. 1, p. 149.

128. T.M. Cormier, J. Applegate, G.M. Berkowitz, P. Braun-Munzinger, P. Cormier, J.W. Harris, C.M. Jachcinski, L.L. Lee, J. Barrette and H.E. Wegner, Phys. Rev. Lett. 38, 940 (1977).

129. T.M. Cormier, C.M. Jachcinski, G.M. Berkowitz, P. Braun-Munzinger, P.M. Cormier, M. Gai, J.W. Harris, J. Barrette and H.E. Wegner, Phys. Rev. Lett. 40, 924 (1978).

130. C.M. Jachcinski, T.M. Cormier, P. Braun-Munzinger, G.M. Berkowitz, P.M. Cormier, M. Gai and J.W. Harris, Phys. Rev. C17, 1263 (1978).

131. D. Shapira, R.M. DeVries, M.R. Clover, R.N. Boyd and P.H. Cherry, Phys. Rev. Lett. 40, 371 (1978).

132. M. Golin, Phys. Lett. 74B, 23 (1978).

133. P. Braun-Munzinger, G.M. Berkowitz, T.M. Cormier, C.M. Jachcinski, J.W. Harris, J. Barrette and M.J. Levine, Phys. Rev. Lett. 38, 944 (1977).

134. K.W. McVoy, Ref. 20, p. 127; Phys. Rev. C3, 1104 (1971).

135. J. Barrette, M.J. Levine, P. Braun-Munzinger, G.M. Berkowitz, M. Gai, J.W. Harris and C.M. Jachcinski, Phys. Rev. Lett. 40, 445 (1978).

136. M.R. Clover, R.M. DeVries, R. Ost, N.J.A. Rust, R.N. Cherry and H.E. Gove, Phys. Rev. Lett. 40, 1008 (1978).

137. K. McVoy, Proceedings of the Symposium on Heavy Ion Elastic Scattering (Rochester, 1977).

137(a). D.M. Brink and N. Takigawa, Nucl. Phys. A279, 159 (1977); S.Y. Lee, N. Takigawa and C. Marty, IPNO/TH 77-19 Preprint (1977).

137(b). D. Dennard, V. Schkolnik and M-A Franey, Phys. Rev. Lett. 40, 1549 (1978).

138. M. Paul, S.J. Sanders, J. Cseh, D.F. Geesaman, W. Henning, D.G. Kovar, C. Olmer and J.P. Schiffer, Phys. Rev. Lett. 40, 1310 (1978).

139. For some recent discussions of this field, see J.L.C. Ford, First Oaxtepec Symposium on Nuclear Physics (Mexico, 1978).

140. D.L. Hillis, E.E. Gross, D.C. Hensley, C.R. Bingham, F.T. Baker and A. Scott, Phys. Rev. C16, 1467 (1977).

141. M.W. Guidry, P.A. Butler, R. Donangelo, E. Grosse, Y. El Masri, I.Y. Lee, F.S. Stephens, R.M. Diamond, L.L. Riedinger, C.R. Bingham, A.C. Kahler, J.A. Vrba, E.L. Robinson and N.R. Johnson, Phys. Rev. Lett. 40, 1016 (1978).

142. R. Donangelo, L.F. Oliveira, J.O. Rasmussen and M.W. Guidry, Lawrence Berkeley Laboratory Preprint, LBL-7720 (1978); M.W. Guidry et. al, Nucl. Phys. A295, 482 (1978).

143. J.R. Birkelund, J.R. Huizenga, H. Freiesleben, K.L. Wolf, J.P. Unik and V.E. Viola, Phys. Rev. C13, 133 (1976).

144. I.Y. Lee, D. Cline, P.A. Butler, R.M. Diamond, J.O. Newton, R.S. Simon, and F.S. Stephens, Phys. Rev. Lett. 39, 684 (1977).

145. K. Kumar and M. Baranger, Nucl. Phys. A122, 273 (1968).

146. W.G. Love, T. Teresawa and G.R. Satchler, Nucl. Phys. A291, 183 (1977); A.J. Baltz, S.K. Kaufmann, N.K. Glendenning and K. Pruess, Phys. Rev. Lett. 40, 20 (1978).

147. P. Doll, M. Bini, D.L. Hendrie, S.K. Kauffmann, J. Mahoney, A. Menchaca-Rocha, D.K. Scott, T.J.M. Symons, K. Van Bibber, Y.P. Viyogi, H. Wieman and A.J. Baltz, Lawrence Berkeley Laboratory Preprint LBL-7195 (1978).

148. A. Johnson, H. Ryde and J. Sztarkier, Phys. Lett. 34B, 605 (1971).

149. For a recent review, see A. Faessler, Ref. 18, p. 437; D. Ward, Ref. 18, p. 417.

150. F.S. Stephens, Comments on Nuclei and Particles VI, 173 (1976); International School of Physics (Varenna, Italy, 1976).

151. M.A.J. Mariscotti, G. Scharff-Goldhaber and B. Buck, Phys. Rev. 178, 1864 (1969).

152. B.R. Mottelson and J.G. Valatin, Phys. Rev. Lett. 5, 511 (1960).

153. P. Thieberger, Phys. Lett. 45B, 417 (1973).

154. F.S. Stephens, Rev. Mod. Phys. 47, 43 (1975).

155. I.Y. Lee, M.M. Aleonard, M.A. Deleplanque, Y. El Masri, J.O. Newton, R.S. Simon, R.M. Diamond and F.S. Stephens, Phys. Rev. Lett. 38, 1454 (1977).

156. S.M. Harris and P.J. Evans, Phys. Rev. Lett. 39, 1186 (1977).

157. L.K. Peker and J.H. Hamilton, Phys. Rev. Lett. 40, 744 (1978).

158. I.Y. Lee, D. Cline, R.S. Simon, P.A. Butler, P. Colombani, M.W. Guidry, F.S. Stepehns, R.M. Diamond, N.R. Johnson and E. Eichler, Phys. Rev. Lett. 37, 420 (1976).

159. N.R. Johnson, D. Cline, S.W. Yates, F.S. Stephens, L.L. Riedinger and R.M. Ronningen, Phys. Rev. Lett. 40, 151 (1978).

160. A. Bohr and B.R. Mottelson, Phys. Scripta 10A, 13 (1974).

161. R.M. Diamond, Australian J. of Phys., to be published.

162. A. Bohr and B.R. Mottelson, Nuc. Structure (Benjamin N.Y.). Vol. II.

163. B.R. Mottelson, Proceedings of the Nuclear Structure Symposium of the Thousand Lakes (Joutsa, Finland, 1970), Vol. II, p. 148.

164. F.S. Stephens, Conference on Highly Excited States of Nuclei (Jülich, Germany 1975).

165. R.S. Simon, M.V. Banaschik, R.M. Diamond, J.O. Newton and F.S. Stephens, Nucl. Phys. A290, 253 (1977).

166. P.J. Tjøm, F.S. Stephens, R.M. Diamond, J. de Boer and W.E. Meyerhof, Phys. Rev. Lett. 33, 593 (1974).

167. R.S. Simon, M.V. Banaschik, P. Colombani, D.P. Soroka, F.S. Stephens and R.M. Diamond, Phys. Rev. Lett. 33, 596 (1974).

168. J.O. Newton, S.H. Sie and G.D. Dracoulis, Phys. Rev. Lett. 40, 625 (1978).

169. M.A. Deleplanque, I.Y. Lee, F.S. Stephens, R.M. Diamond and M.M. Aleonard, Phys. Rev. Lett. 40, 629 (1978).

170. P.O. Tjøm, I. Espe, G.B. Hagemann, B. Herskind and D.L. Hillis, Phys. Lett. 72B, 439 (1978).

171. G. Anderson, S.E. Larsson, G. Leander, P. Möller, S.G. Nilsson, I. Ragnarsson, S. Aberg, R. Bengtson, J. Dudek, B. Nerlo-Pomarska, K. Pomorski and Z. Szymanski, Nucl. Phys. A268, 205 (1976).

172. J. Pedersen, B.B. Back, F.M. Bernthal, S. Bjørnholm. J. Borggreen, O. Christensen, F. Folkmann, B. Herskind, T.L. Khoo, M. Neiman, F. Pühlhoffer and G. Sletten, Phys. Rev. Lett. 39, 990 (1977).

173. T. Døssing, K. Neergaard, K. Matsuyanagi and Hsi-Chen Chang, Phys. Rev. Lett. 39, 1395 (1977).

174. A. Faessler and M. Ploszjcak, Phys. Rev. C16, 2032 (1977).

175. M. Hillman and Y. Eyal, Ref. 24, p. 109.

176. F. Pühlhofer, Nucl. Phys. A280, 267 (1977).

177. J. Barrette, P. Braun-Munzinger, C.K. Gelbke, H.L. Harney, H.E. Wegner, B. Zeidman, K.D. Hildenbrand, and U. Lynen, to be published in Nucl. Phys. A (1978).

178. V.S. Ramamurthy, S.S. Kapoor and S.K. Kataria, Phys. Rev. Lett. 25, 386 (1970).

179. F. Pühlhofer, W.F.W. Schneider, F. Busch, J. Barrette, P. Braun-Munzinger, C.K. Gelbke and H.E. Wegner, Phys. Rev. C16, 1010 (1977).

180. T.M. Cormier, E.R. Cosnan, A.J. Lazzarini, H.E. Wegner, J.D. Garrett and F. Pühlhofer, Phys. Rev. C15, 654 (1977).

181. G. Sauer, H. Chandra and U. Mosel, Nucl. Phys. A264, 221 (1976).

182. S. Cohen, F. Plasil and W.J. S atecki, Ann. of Phys. 82, 557 (1974).

183. J. Gomez del Campo, M.E. Ortiz, A. Dacal, J.L.C. Ford, R.L. Robinson, P.H. Stelson and S.T. Thornton, Nucl. Phys. A262, 125 (1976).

184. J. Gomez del Campo, J.L.C. Ford, R.L. Robinson, M.E. Ortiz, A. Dacal and E. Andrade, Nucl. Phys. A297, 125 (1978).

185. U. Mosel and D. Glas, to be published.

186. W.J. Swiatecki, Ref. 14, p. C4-45.

187. W.J. Swiatecki and S. Björnholm, Phys. Reports 4C, 325 (19[illegible]).

188. F. Plasil, Phys. Rev. C17, 823 (1978).

189. F. Plasil, R.L. Ferguson, H.C. Britt, R.H. Erkkila, P.D. Goldstone, R.H. Stokes and H.H. Gutbrod, Oak Ridge Preprint (1978).

190. M. Lefort, Ref. 20, p. 274; Reports on Prog. in Phys. 39, 129 (1976).

191. M. Lefort, Ref. 24, p. C5-57.

192. M. Lefort, J. Phys. A7, 107 (1974).

193. J. Galin, D. Guerreau, M. Lefort and X. Tarrago, Phys. Rev. C9, 1018 (1974).

194. D. Glas and U. Mosel, Nucl. Phys. A237, 429 (1975).

195. W.D. Myers, Nucl. Phys. A 204, 465 (1973); Ref. 18, p. 1.

196. S. Vigdor, Ref. 22, p. 95.

197. R.G. [illegible]kstad, Ref. 25.

198. R.G. Stokstad, R.A. Dayras, J. Gomez del Campo, P.H. Stelson, C. Olmer and M.S. Zisman, Phys. Lett. 70B, 289 (1977).

199. R. Kohlmeyer, W. Pfeffer and F. Pühlhoffer, Nucl. Phys. A292, 266 (1977).

200. J. Natowitz, Ref. 25.

201. E. Seglie, D. Sperber and A. Sherman, Phys. Rev. C11, 1227 (1975).

202. R. Bass, Phys. Lett. 47B, 139 (1973); Nucl. Phys. A231, 45 (1974).

203. R. Beck and D.H.E. Gross, Phys. Lett. 47B, 143 (1973).

204. D.H.E. Gross and H. Kalinowski, Phys. Lett. 48B, 302 (1974).

205. J.P. Bondorf, M.I. Sobel and D. Sperber, Phys. Reports C15, 83 (1974).

206. K. Siwek-Wilczynska and J. Wilczynski, Nucl. Phys. A264, 115 (1976); Nukleonika 21, 517 (1976).

207. J.R. Birkelund, J.R. Hu[illegible] J.N. De and D. Sperber, Phys. Rev. Lett. 40, 1123 (1978).

208. B.B. Back, R.R. Betts, C. Gaarde, J.S. Larsen, E. Michelsen and Tai Kuang-Hsi, Nucl. Phys. A285, 317 (1977).

209. H. Doubre, A. Gamp, J.C. Jacmart, N. Poffé, J.C. Roynette and J. Wilczynski, Phys. Lett. 73B, 135 (1978).

210. D. Glas and U. Mosel, Phys. Lett. 49B, 301 (1974); Nucl. Phys. A264, 268 (1976).

211. D.J. Morrissey, W. Loveland, R.J. Otto and G.T. Seaborg, Phys. Lett. <u>74B</u>, 35 (1978).

212. D. Kovar, Ref. 27, p. 18.

213. S. Harar, Colloque Franco-Japonais de Spectroscopie Nucléaire, Dogashima, Japan (Univ. of Tokyo, 1977). p. 191.

214. P. Sperr, T.H. Braid, Y. Eisen, D.G. Kovar, F.W. Prosser, J.P. Schiffer, S.L. Tabor and S. Vigdor, Phys. Rev. Lett. 37, 321 (1976).

215. R.M. Freeman and F. Haas, Phys. Rev. Lett. 40, 927 (1978).

216. R.A. Broglia, C.H. Dasso, G. Pollarolo and A. Winther, Phys. Rev. Lett. 40, 707 (1978).

217. P.A.M. Dirac, Proc. Camb. Phil. Soc. 26, 376 (1930).

218. S.E. Koonin, K.T.R. Davies, V. Maruhn-Rezwani, H. Feldmeier, S.J. Krieger and J.W. Negele, Phys. Rev. C15, 1359 (1977).

219. See also detailed reviews by A.K. Kerman, Proceedings of the Enrico Fermi Summer School (Varenna, Italy, 1977) and Ref. 28, p. 711; P. Bonche, Ref. 24, p. C5-213; J.W. Negele, Ref. 25, and this school.

220. G.F. Bertsch and S.F. Tsai, Phys. Reports 18C (1975).

221. P. Bonche, B. Grammaticos and S. Koonin, Saclay Preprint DPh-T/DOC/77/128, to be published in Phys. Rev. C (1978).

222. H. Gauvin, R.L. Hahn, Y. Le Beyec and M. Lefort, Phys. Rev. C10, 722 (1974).

223. C. Cabot, H. Gauvin, Y. Le Beyec and M. Lefort. J. de. Phys. L36, 289 (1976).

224. S. Della-Negra, H. Gauvin, H. Jungclas, Y. Le Beyec and M. Lefort, Z. Phys. A282, 65 (1977).

225. R.C. Britt, B.H. Erkkila, P.D. Goldstone, R.H. Stokes, B.B. Back, F. Folkmann, O. Christensen, B. Fernandez, J.D. Garrett, G.B. Hagemann, B. Herskind, D.L. Hillis, F. Plasil, R.L. Ferguson, M. Blann and H.H. Gutbrod, Phys. Rev. Lett. 39, 1458 (1977).

226. L. Kowalski, J.M. Alexander, D. Logan, M. Rajagopalan, M. Kaplan, M.S. Zisman and T.W. Debiak, Stony Brook Preprint, 1978.

227. T. Inamura, M. Ishihara, T. Fukuda, T. Chimoda and H. Huruta, Phys. Lett. 68B, 51 (1977).

228. D. Horn, H.A. Enge, A. Sperduto and A. Grane, Phys. Rev. C17, 118 (1978).

229. J.P. Schiffer, Ref. 17, p. 813.

230. J.M. Nitschke, Symposium on Superheavy Elements (Lubbock, Texas, 1978), Lawrence Berkeley Laboratory Preprint LBL-7705 (1978).

231. W. Reisdorf and P. Armbruster, International Meeting on Reactions of Heavy Ions with Nuclei (Dubna, 1977). GSI Preprint-Bericht-M-2-78.

232. R.V. Gentry, T.A. Cahill, N.R. Fletcher, H.C. Kaufmann, L.R. Medsker, J.W. Nelson and R. Flocchini, Phys. Rev. Lett. 38, 479 (1977).

233. C.J. Sparks, S. Raman, E. Ricci, R.V. Gentry and M.O. Krause, Phys. Rev. Lett. 40, 507 (1978).

234. W.J. Swiatecki and C.F. Tsang, Lawrence Berkeley Lab Preprint LBL-666 (1971); R. Kalpakchieva, Yu. Ts. Oganessian, Yu. E. Penionzhkevich, H. Sodan and B.A. Gvozdev, Phys. Lett. 69B, 287 (1977).

235. E.K. Hulet, R.W. Lougheed, J.F. Wild, J.H. Landrum, P.G. Stevenson, A. Ghiorso, J.M. Nitschke, R.J. Otto, D.J. Morrissey, P.A. Baisden, B.F. Gavin, D. Lee, R.J. Silva, M.M. Fowler, and G.T. Seaborg, Phys. Rev. Lett. 39, 385 (1977).

236. Yu. Ts. Oganessian, H. Bruchertseifer, G.V. Buklanov, V.I. Chepigin, Choi Val Sak, B. Eichler, K.A. Gavrilov, H. Gaeggeler, Yu. S. Korotin, O.A. Orlova, T. Reetz, W. Seidl, G.M. Ter-Akopian, S.P. Tretyakova, and I. Zvara, Nucl. Phys. A294, 213 (1978).

237. H. Sann, A. Olni, Y. Cirelekoglu, D. Pelte, U. Lynen, H. Stelzer, A. Gobbi, Y. Eyal, W. Kohl, R. Renfordt, I. Rode, G. Rudlof, D. Schwalm and R. Bock, Ref. 25, p. 281; K.D. Hildenbrand, H. Freiesleben, F. Pühlhofer, W.F.W. Schneider, R. Bock, D.V. Harrach and H.J. Specht, Phys. Rev. Lett. 39, 1065 (1977).

238. G. Wolschin and W. Nörenberg, Z. Phys. A284, 209 (1978).

239. V.F. Weisskopf, Phys. Today 14, 18 (1960).

240. H. Feshbach, Rev. Mod. Phy. 46, 1 (1974) and refs. therein.

241. One of the earliest experiments related to this phenomenon is that of K. Kaufman and W. Wolfgang, Phys. Rev. 121, 192 (1961). Other early works include: G.F. Gridnev, V.V. Volkov and J. Wilczynski, Nucl. Phys. A142, 385 (1970); J. Galin, D. Guerreau, M. Lefort, J. Péter and X. Tarrago, Nucl. Phys. A159, 461 (1970).

242. For a recent review, see W.U. Schröder and J.R. Huizenga, Ann. Rev. Nucl. Sci. 27, 465 (1977).

243. A.G. Artukh, G.F. Gridnev, V.L. Mikheev, V.V. Volkov and J. Wilczynski, Nucl. Phys. A211, 299 (1973); A215, 91 (1973).

244. J. Wilczynski, Phys. Lett. B47, 484 (1973).

245. H.H. Deubler and K. Dietrich, Phys. Lett. 56B, 241 (1975).

246. K. Derlanger, F. Grangé, H. Hofmann, C. Ngo and J. Richert, Phys. Rev. C17, 1495 (1978).

247. J. Galin, Ref. 24, p. C5-83.

248. G.J. Mathews, G.J. Wozniak, R.P. Schmitt and L.G. Moretto, Z. Phys. A283, 247 (1977).

249. V.V. Volkov, Ref. 18, p. 363 and V.V. Volkov, Sov. J. Nucl. Phys. 6, 420 (1976).

250. V.V. Volkov, Ref. 20, p. 253.

251. L.G. Moretto and R. Schmitt, Ref. 24, p. C5-109.

252. J. Galin, Ref. 24, p. C5-83.

253. W. Norenberg; Ref. 24, p. C5-141.

254. H.A. Weidenmuller, Ref. 25.

255. R. Babinet, B. Cauvin, J. Girard, H. Nifenecker, B. Gatty, D. Guerreau, M. Lefort and X. Tarrago, Nucl. Phys. A296, 160 (1978).

256. P.D. Bond, Phys. Rev. Lett. 40, 501 (1978).

257. K. Sugimoto, N. Takahashi, A. Mizobuchi, Y. Nojiri, T. Minamisono, M. Ishihara, K. Tanaka and H. Kamitsubo, Phys. Rev. Lett. 39, 323 (1977).

258. M. Ishihara, K. Tanaka, T. Kammuri, K. Matsuoka and M. Sano, Phys. Lett. 73B, 281 (1978).

259. W. Trautmann, J. de Boer, W. Dünnweber, G. Graw, R. Kopp, C. Lauterbach, H. Puchta and U. Lynen, Phys. Rev. Lett. 39, 1062 (1977).

260. F. Plasil, R.L. Ferguson, H.C. Britt, R.H. Stokes, B.H. Erkkila, P.D. Goldstone, M. Blann and H.H. Gutbrod, Phys. Rev. Lett. 40, 1164 (1978).

261. H. Feshbach, First Oaxtepec Symposium on Nuclear Physics (Oaxtepec, Mexico, 1978).

262. H. Feshbach, "Statistical Multistep Reactions," Proc. of Conf. on Nuc. React. Mechanisms (Varenna, Italy, 1977).

263. H. [illegible], J.P. Coffin, P. Engelstein, A. Gallmann, K.S. Sim and P. Wagner, Phys. Lett. 71B, 63 (1977).

264. T. Tamura and T. Udagawa, Phys. Lett. 71B, 273 (1977).

265. S. Tsai and G.F. Bertsch, Phys. Lett. 73B, 247 (1978).

266. T. Udagawa, Ref. 28, p. 667.

267. G. Bertsch and S.F. Tsai, Phys. Reports 18C, 126 (1975).

268. R.A. Broglia, C.H. Dasso and A. Winther, Phys. Lett. 61B, 113 (1976); R.A. Broglia, O. Civitarese, C.H. Dasso and A. Winther, Phys. Lett. 73B, 405 (1978). N. Takigawa, University of Münster Preprint, 1978.

269. K.F. Liu and G.E. Brown, Nucl. Phys. A265, 385 (1976).

270. R.R. Betts, S.B. DiCenzo, M.H. Mortensen and R.L. White, Phys. Rev. Lett. 39, 1183 (1977).

271. D. Ashery, M.S. Zisman, R.B. Weisenmiller, A. Guterman, D.K. Scott and C. Maguire, Lawrence Berkeley Laboratory Annual Report (1975), p. 97; A. Guterman, D. Ashery, J. Alster, D.K. Scott, M.S. Zisman, C.K. Gelbke, H.H. Wieman and D.L. Hendrie, to be published.

272. P. Doll, D.L. Hendrie, J. Mahoney, A. Menchaca-Rocha, D.K. Scott, T.J.M. Symons, K. Van Bibber, Y.P. Viyogi and H.H. Wieman, to be published.

273. M. Buenerd, D. Lebrun, J. Chauvin, Y. Gaillard, J.M. Loiseaux, F. Martin, G. Perrin and P. de Saintignon, Phys. Rev. Lett. 40, 1482 (1978).

274. R.R. Betts, Private communication, 1978.

275. J.P. Bondorf, Lectures at International School of Physics (Enrico Fermi), 1974.

276. J.P. Bondorf, Ref. 18, p. 383.

277. W. Nörenberg, Phys. Lett. 52B, 289 (1974).

278. G. Wolschin and W. Nörenberg, Z. Phys. A284, 209 (1978) and refs. therein.

279. J.R. Huizenga, Ref. 25.

280. J.R. Huizenga, J.R. Birkelund, W.U. Schröder, K.L. Wolf and V.E. Viola, Phys. Rev. Lett. 37, 885 (1976).

281. For a fuller discussion, see M. Lefort, Symposium on New Avenues in Nuclear Physics (Rehovot, Israel, 1976).

282. G. Wolschin and W. Nörenberg, Z. Phys. A284, 209 (1978) and refs. therein.

283. F. Beck and D.H.E. Gross, Phys. Lett. B47, 143 (1973).

284. J.P. Bondorf, M.I. Sobel, and D. Sperber, Phys. Rev. C15, 83 (1974).

285. D.H.E. Gross, Nucl. Phys. A240, 472 (1975).

286. W.U. Schröder, J.R. Birkelund, J.R. Huizenga, K.L. Wolf and V.E. Viola, Phys. Rev. C16, 623 (1977).

287. J.P. Bondorf, J.R. Huizenga, M.I. Sobel and D. Sperber, Phys. Rev. C11, 1265 (1975).

288. J.R. Huizenga, Nukleonika 20, 291 (1975).

289. S.N. De and D. Sperber, Phys. Lett 72B, 293 (1978).

290. B. Sinha, Phys. Lett. 71B, 243 (1977).

291. W.U. Schröder, J.R. Huizenga, J.R. Birkelund, K.L. Wolf and V.E. Viola, Phys. Lett 71B, 283 (1977).

192. W.U. Schröder, [illegible] Birkelund, J.R. Huizenga, K.L. Wolf and V.E. Viola, University of Rochester Preprint UR-NSRL-[illegible] ([illegible]), to be published in Physics Reports.

193. [illegible] Swiatecki, [illegible] Phys. [illegible], 451 (1972).

194. [illegible] Preprint, [illegible] to be published.

195. [illegible] Arnold, [illegible] and [illegible] Reports [illegible]-1976- [illegible] and [illegible]; Ann. of Phys. [illegible] ([illegible]).

196. [illegible] Phys. Rev. Lett. [illegible] ([illegible]).

197. [illegible] Nucl. Phys. A[illegible], [illegible] ([illegible]).

198. [illegible] Physica Scripta [illegible] ([illegible]).

199. [illegible] Blocki, [illegible] Randrup, W.J. Swiatecki and C.F. Tsang, Ann. [illegible] ([illegible]).

200. [illegible] Lawrence Berkeley Laboratory Preprint LBL-[illegible] and [illegible] Preprint-[illegible].

201. R. [illegible], M.N. [illegible], [illegible], K. [illegible] and [illegible], Phys. Rev. Lett. [illegible] ([illegible]).

202. [illegible] Braun-Munzinger, [illegible] and T.A. Gelbke, Phys. Rev. Lett. [illegible] ([illegible]).

203. [illegible] and [illegible] University Preprint-[illegible] ([illegible]).

204. [illegible] Tanaka and [illegible] ([illegible]).

205. [illegible] Moretto, [illegible], R. Schmitt and [illegible] Stephens, Phys. Rev. Lett. [illegible] ([illegible]).

206. M. Berlanger, M.A. Deleplanque, C. Gerschel, F. Hanappe, M. Leblanc, J.F. Mayault, [illegible], [illegible] Perrin, [illegible] Peter, B. Tamain and L. Valentin, J. Phys. Lettres [illegible] ([illegible]).

207. M.M. Aleonard, [illegible] Wozniak, P. Glassel, M.A. Deleplanque, R.M. Diamond, L.G. Moretto, R.P. Schmitt and F.S. Stephens, Phys. Rev. Lett. 40, [illegible] (1978).

308. P.R. Christensen, F. Folkmann, O. Hansen, O. Nathan, N. Trautner, F. Videbaek, S.Y. van der Werf, H.C. Britt, R.P. Chestnut, H. Freiesleben and F. Pühlhofer, Phys. Rev. Lett. 1245 (1978).

309. K. Van Bibber, R. Ledoux, S.G. Steadman, F. Videbaek, G. Young and C. Flaum, Phys. Rev. Lett. 38, 334 (1977).

310. P. Dyer, R.J. Puigh, R. Vandenbosch, T.D. Thomas and M.S. Zisman, Phys. Rev. Lett. 39, 392 (1977).

311. G.J. Wozniak, R.P. Schmitt, P. Glässel, R.C. Jared, G. Bizard and L.G. Moretto, Phys. Rev. Lett. 40, 1436 (1978).

312. J.B. Natowitz, M.N. Namboodiri, P. Kasiraj, R. Eggers, L. Adler, P. Gonthier, C. Cerruti and T. Alleman, Phys. Rev. Lett. 40, 751 (1978).

313. K. Siwek-Wilczynska and J. Wilczynski, Nucl. Phys. A264, 115 (1976); Nukleonika 21, 517 (1976).

314. D.H.E. Gross and H. Kalinowski, Ref. 20, p. 194.

315. M. Blann, Ann. Rev. Nucl. Sci. 25 (1975).

316. R. Weiner and M. Weström, Nucl. Phys. A286, 282 (1977); Phys. Rev. Lett. 34, 1523 (1975).

317. R. Weiner, Phys. Rev. Lett. 32, 630 (1974); Phys. Rev. D13, 1363 (1976).

318. H. Bethe, Phys. Rev. 53, 675 (1938).

319. S. Tomonaga, Z. Phys. 110, 573 (1938).

320. R.K. Pathria, Statistical Mechanics (Academic Press, NY, 1972) Chapter 8; A. Isihara, Statistical Physics (Academic Press, NY, 1971) Chapter 13.

321. A. Kind and G. Paternagnani, Nuovo Cimento 10, 1375 (1953).

322. M. Blann, A. Mignerey and W. Scobel, Nukleonika 21, 335 (1976).

323. D.K. Scott, From Nuclei to Nucleons, 1st Oaxtepec Symposium on Nuclear Physics (Mexico, 1978), Lawrence Berkeley Laboratory Preprint LBL-7703 (1978).

324. For a review, see J. Galin, Ref. 28, p. 683.

325. C.K. Gelbke, M. Bini, C. Olmer, D.L. Hendrie, J.L. Laville, J. Mahoney, M.C. Mermaz, D.K. Scott and H.H. Wieman, Phys. Lett. 71B, [illegible] (1977).

326. T. [illegible], M. Ishihara, N. Kamitsubo, T. [illegible] and T. [illegible], INS - Cyclotron Preprint 46 (1978).

327. [illegible], [illegible], [illegible], H. [illegible], [illegible] and J. Wilczynski, Phys. Lett. 74B, 219 (1978).

328. H. [illegible], R. Albrecht, W. Dünnweber, G. Graw, S.G. Steadman, J.P. Wurm, D. [illegible], V. [illegible] and F. [illegible], [illegible] A [illegible], [illegible] (1977).

329. [illegible] and M. Weström, Phys. Rev. Lett. [illegible], [illegible] ([illegible]).

330. J.M. Miller, G.L. Catchen, D. Logan, M. Rajagopalan, J.M. Alexander, M. Kaplan and M.S. Zisman, Phys. Rev. Lett. [illegible], [illegible] ([illegible]).

331. J.M. Miller, D. Logan, G.L. Catchen, M. Rajagopalan, J.M. Alexander, M. Kaplan, J.W. Ball, M.S. Zisman and L. Kowalski, Phys. Rev. Lett. 40, [illegible] ([illegible]).

332. L. Kowalski, J. Alexander, D. Logan, M. Rajagopalan, M. Kaplan, M.S. Zisman and T.W. Debiak, Preprint ([illegible]).

333. D.H.E. Gross and J. Wilczynski, Phys. Lett. 67B, [illegible] ([illegible]).

334. J.P. Wurm, Ref. [illegible].

335. W.J. Swiatecki, Ref. 19, p. 3-9.

336. For some of the earliest studies, see, I. Frisler, R.J. Lofgren, E.P. Ney, F.Oppenheimer, H.L. Bradt and B. Peters, Phys. Rev. 74, 213 (1948) and Phys. Rev. 74, [illegible] ([illegible]); H. Alfvén, Nature 143, 435 (1939).

337. A.S. Goldhaber and H.H. Heckman, Lawrence Berkeley Laboratory Preprint LBL-6570 (1978), to be published in Ann. Rev. Nucl. Sci.

338. J. Blocki, Y. Boneh, J.R. Nix, J. Randrup, M. Robel, A.J. Sierk and, W.J. Swiatecki, Lawrence Berkeley Laboratory Preprint LBL-6536, to be published in Ann. of Phys. (1978).

339. J.P. Bondorf, Ref. 24, p. 65-195.

340. G. Bertsch, Lecture Notes for the Les Houches Summer School (1977).

341. For a recent review, see J.R. Nix, Los Alamos Preprint LA-UR-77-2952.

342. M. Buenerd, C.K. Gelbke, B.G. Harvey, D.L. Hendrie, J. Mahoney, A. Menchaca-Rocha, C. Olmer and D.K. Scott, Phys. Rev. Lett. 37, 1191 (1976).

343. C.K. Gelbke, D.K. Scott, M. Bini, D.L. Hendrie, J.L. Laville, J. Mahoney, M.C. Mermaz and C. Olmer, Phys. Lett. 70B, 415 (1977).

344. D.K. Scott, M. Bini, P. Doll, C.K. Gelbke, D.L. Hendrie, J.L. Laville, J. Mahoney, A. Menchaca-Rocha, M.C. Mermaz, C. Olmer, T.J.M. Symons, Y.P. Viyogi, K. VanBibber, H. Wieman and P.J. Siemens, Lawrence Berkeley Laboratory Preprint LBL-7729 (1978).

345. H. Kamitsubo, Ref. 21, p. 177; Ref. 21, p. 163.

346. H. Kamitsubo, M. Yoshie, I. Kohno, S. Nakajima, I. Yamane and T. Mikumo, Ref. 16, p. 540.

347. T. Mikumo, I. Kohno, K. Katori, T. Motobayashi, S. Nakajima, M. Yoshie and H. Kamitsubo, Phys. Rev. C14, 1458 (1976).

348. D.E. Greiner, P.J. Lindstrom, H.H. Heckman, B. Cork and F. Bieser, Phys. Rev. Lett. 35, 152 (1975).

349. K. Masuda and F. Uchiyama, Phys. Rev. C15, 1598 (1977).

350. C.K. Gelbke, C. Olmer, M. Buenerd, D.L. Hendrie, J. Mahoney, M.C. Mermaz and D.K. Scott, Lawrence Berkeley Laboratory Preprint LBL-5826 (1977), to be published in Phys. Reports (1978).

351. V.V. Volkov, Sov. J. of Nucl. Phys. 6, 420 (1976).

352. J.P. Bondorf, F. Dickman, D.H.E. Gross and P.J. Siemens, Ref. 12, p. C6-145; R. Billerey, C. Cerruti, A. Chevarier, N. Chevarier and A. Deneyer, Z. Phys. A284, 389 (1978).

353. A.Y. Abul-Magd and K.I. El-Abed, Prog. Th. Phys. (Japan) 53, 480 (1975).

354. A. Bohr and B. Mottelson in Nuclear Structure (Benjamin, 1969), Vol. 1, p. 187.

[illegible] Phys. Lett. [illegible]

[illegible]

[illegible]

[illegible]

[illegible] preprint [illegible]

[illegible]

[illegible] High Energy [illegible]

[illegible] Westfall [illegible] Meyer, H. [illegible] A. [illegible] Phys. [illegible]

[illegible] Lectures in Theoretical Physics [illegible] Interscience [illegible]

[illegible] Phys. [illegible]

[illegible] preprint [illegible]

[illegible] Structure of the Nucleus [illegible] Wesley [illegible]

[illegible] Whitney [illegible] Phys. Rev. Lett. 36 [illegible]

[illegible] Phys. Rev. [illegible]

[illegible] Johansen [illegible] Jensen and H. [illegible] Nucl. Phys. A288 [illegible]

[illegible] Youngblood, Bull. Am. Phys. Soc. [illegible]

[illegible] V.R. Pandharipande, Phys. Lett. 31B, 635 (197[illegible]).

[illegible] G. Bertsch and D. Mundinger, Phys. Rev. C17, 1646 (1978).

37[illegible]. F. Beiser, H. Crawford, P. Doll, D.E. Greiner, C.K. Gelbke, H.H. Heckman, D.L. Hendrie, P. Lindstrom, J. Mahoney, D.K. Scott, T.J.M. Symons, K. Van Bibber, Y.P. Viyogi, G.D. Westfall and H. Wieman, to be published (1978).

[illegible]. [illegible] Greiner, Nucl. Inst. and Meth. 103, 291 (1972).

[illegible]. [illegible] and H. Faraggi, private communication.

[illegible]. [illegible], F. [illegible]angeli and L. Oliveira, Ref. 27, p. [illegible] [illegible] published in Nucl. Phys. (1978).

[illegible], private communication (1978).

[illegible] Morrissey, W.R. Marsh, R.J. Otto, W. Loveland, and [illegible], LBL Preprint 6579 (1978).

[illegible], W.J. Swiatecki, T. Kodama, L.J. El-Jaick and [illegible], Phys. Rev. [illegible] (1977).

[illegible], [illegible] Perry, [illegible] Kemsberg, A.M. Poskanzer, [illegible] witz and F. Plasil, Phys. Rev. Lett. 36, 1580 (1976).

[illegible], J.A. Chersin, J.V. Geaga, J.Y. Grossiord, [illegible], [illegible] Schroeder, R.H. Scott and H.H. Wieman, [illegible] published.

[illegible], [illegible], J.L. Hendrie, J. Mahoney, M.C. Merman, [illegible] and [illegible] Scott, Phys. Lett. 65B, [illegible] (1976).

[illegible] and T. Fortel, Ann. Rev. of Nucl. Sc. [illegible], 451 (197[illegible]).

[illegible]. W.R. Frazer, [illegible] Ingber, C.H. Mehta, C.H. Poon, D. Silverman, [illegible], [illegible] and H.Y. Yesian, Rev. Mod. Phys. 44, 284 (1972).

[illegible]. [illegible] Jackson, Phys. Lett. 71B, 57 (1977).

[illegible]. [illegible], lectures at École d'Été de Physique Theorique, Les Houches (1977).

[illegible]. [illegible] Cumming, P.E. Haustein, R.W. Stoenner, L. Mausner and R.A. Naumann, Phys. Rev. C10, 739 (1974); Phys. Rev. C14, 1554 (1976) and Brookhaven National Laboratory Preprint BNL-25378 (1977).

[illegible]. [illegible] Lindstrom, D.E. Greiner, H.H. Heckman, B. Cork and [illegible] Bieser, LBL-Preprint 3650 (1975).

389. D.J. Morrissey, W. Loveland, W.R. Marsh and G.T. Seaborg, LBL Preprint 7718 (1978).

390. M.I. Sobel, P.J. Siemens, J.P. Bondorf and H.A. Bethe, Nucl. Phys. A 251, 502 (1975).

[illegible] for example, An Atlas of Heavy-Ion Topology, [illegible] [illegible] [illegible] and [illegible]

[illegible] Proc. of Topical Meeting on Multiparticle Production of Nuclei at Very High Energy, [illegible]

[illegible] Phys. [illegible]

[illegible] Phys. Rev. [illegible]

[illegible] Phys. Rev. [illegible]

[illegible] Meyer, [illegible] and [illegible]

[illegible]

[illegible] Preprint [illegible]

[illegible] Meyer, [illegible] Phys. Rev. [illegible]

[illegible] A. McKellar, Phys. Rev. Lett. [illegible]; A. McKellar, [illegible] and [illegible] Phys. Lett. [illegible]

[illegible] Nakamiya, [illegible] Tanihata, [illegible] Schnetzer, [illegible] Anderson, [illegible] Chamberlain, [illegible] and H. Steiner, J. Phys. Soc. Japan [illegible]

[illegible] P.B. Price, J. Stevenson and K. Fraenkel, Phys. Rev. Lett. [illegible] ([illegible]).

[illegible] P.B. Price and J. Stevenson, LBL Preprint 7702 (1978).

404. R.K. Smith and M. Danos, Ref. 25.

405. J.B. Ball, C.B. Fulmer, M.L. Mallory and R.L. Robinson, ORNL Preprint (1978).

406. H.W. Bertini, T.A. Gabriel, R.T. Santoro, O.W. Hermann, N.W. Larson and J.M. Hunt, ORNL Report TM-4134 (1974).

[illegible] Bondorf and W. Nörenberg, Phys. Lett. 44B, 4[illegible] [illegible].

[illegible] M. [illegible], [illegible], [illegible] Hendrie, [illegible] Mahoney, [illegible], [illegible], [illegible], K. Van Bibber, [illegible] and H. Wieman, [illegible] [illegible].

[illegible], Münster Preprint [illegible].

[illegible] Phys. Rev. Lett. [illegible].

[illegible] Parker, BNL Preprint [illegible].

[illegible] Phys. Rev. Lett. [illegible].

[illegible], Private communication, [illegible].

[illegible] Conference in Nuclear Chemistry [illegible].

[illegible] Phys. Rev. [illegible].

[illegible] Welton, Phys. Lett. 66B, [illegible].

417. M. Blann, Nucl. Phys. A235, 211 (1974); I. Arassi, H.A. Weidenmuller and G. Mantzouranis, Phys. Rep. 27, 145 (1976).

418. J.J. Griffin, Phys. Lett. 24B, 5 (1967).

419. V.E. Viola, R.G. Clark, W.G. Meyer, A.M. Zebelman and R.G. Sextro, Nucl. Phys. A261, 174 (1976); V.E. Viola, C.T. Roche, W.G. Meyer and R.G. Clark, Phys. Rev. C10, 2416 (1974).

420. G. Bertsch and A.A. Amsden, Los Alamos Preprint LA-78-838 (1978).

421. G.I. Kopylov, Phys. Lett. 50B, 472 (1974).

422. S.E. Koonin, Phys. Lett. 70B, 43 (1977).

423. A.T. Laasanen, C. Ezell, L.J. Gutay, W.N. Schreiner, P. Schübelin, L. von Lindern and F. Turkot, Phys. Rev. Lett 38, 1 (1977).

424. R. Stock, Heavy-Ion Collisions, Vol. 1, ed. R. Bock (North Holland), in press; Phys. Reports, in press.

[illegible] Greiner, [illegible]

[illegible] Greiner, [illegible] High Energy [illegible]

[illegible]

[illegible] Phys. Rev. Lett. [illegible]

[illegible] Greiner, [illegible]

[illegible] Phys. Rev. Lett. [illegible]

[illegible]

[illegible] and W. Greiner, Phys. Rev. Lett. [illegible]

[illegible]

[illegible]

[illegible] review, see [illegible] Nix, Symposium on Relativistic Heavy [illegible] Research GSI, [illegible] Los Alamos Preprint LA-[illegible]

[illegible]

[illegible] review see A. Goldhaber, Ref. [illegible]; A. [illegible] and [illegible] Phys. Rev. [illegible] (1977).

[illegible] Baumgardt, J.U. Schott, Y. Sakamoto, E. Schopper, H. Stöcker, J. Hofmann, W. Scheid and W. Greiner, Z. Phys. [illegible], [illegible] (1975).

[illegible] A.M. Poskanzer, [illegible] Sextro, A.M. Zebelman, H.H. Gutbrod, A. Sandoval and R. Stock, Phys. Rev. Lett. 35, [illegible] (1975).

[illegible] For a discussion, see H.H. Heckman, Ref. 26, and E. Schopper, Ref. 25.

[illegible] M.M. Gazzaly, J.B. Carroll, J.V. Geaga, G. Igo, J.B. McClelland, M.A. Nasser, H. Spinka, A.L. Sagle, V. Perez-Mendez, R. Talaga, E.T.B. Whipple and F. Zarbakash, LBL Preprint 7278 (1978) to be published in Phys. Rev. Lett. (1978).

[illegible] [illegible] [illegible]ker, [illegible] H[illegible]ffman, W. [illegible]cheid and W. Greiner, [illegible]
[illegible] [illegible] Properties [illegible]f Nuclei, Austria [illegible]

[illegible], Rev. M[illegible]. Phys. [illegible], [illegible] [illegible]

[illegible], M. [illegible] and W. Greiner, [illegible] Phys. [illegible], [illegible]

[illegible] and [illegible] Kauffman, Phys. Rev. Lett. [illegible], [illegible]

[illegible] and [illegible] Perry, Phys. Rev. Lett. [illegible], [illegible]; [illegible], Phys. Rev. [illegible], [illegible]; [illegible] Chaplin and [illegible], Phys. Rev. [illegible], [illegible]

[illegible] [illegible]maker, [illegible] Preprint, [illegible]

[illegible], Experiment and Theory in Physics, [illegible]

[illegible], Other Men's Flowers [illegible] Cape [illegible], [illegible]; [illegible] Phys. Reports [illegible], [illegible] (1978).

[illegible] Kipling, The Glory of the Garden.

[illegible] Friedrich, K. Langanke, A. Weiguny and R. Santo, University [illegible] Münster Preprint, 1978; A. Weiguny, Ref. [illegible], p. [illegible] and ref. therein.

[illegible] [illegible] Kolk, [illegible] Gehrhard, [illegible] Kubono, M.A. Franey, and [illegible] Gripp, Phys. Lett. 76B, 195 (1978).